Russian Original Vol. 32, No. 2, February, 1972

Translation published August, 1972

SOVIET ATOMIC ENERGY

АТОМНАЯ ЭНЕРГИЯ
(ATOMNAYA ÉNERGIYA)

TRANSLATED FROM RUSSIAN

CONSULTANTS BUREAU, NEW YORK

SOVIET ATOMIC ENERGY

Soviet Atomic Energy is a cover-to-cover translation of *Atomnaya Énergiya*, a publication of the Academy of Sciences of the USSR.

An arrangement with Mezhdunarodnaya Kniga, the Soviet book export agency, makes available both advance copies of the Russian journal and original glossy photographs and artwork. This serves to decrease the necessary time lag between publication of the original and publication of the translation and helps to improve the quality of the latter. The translation began with the first issue of the Russian journal.

Consultants Bureau journals appear about six months after the publication of the original Russian issue. For bibliographic accuracy, the English issue published by Consultants Bureau carries the same number and date as the original Russian from which it was translated. For example, a Russian issue published in December will appear in a Consultants Bureau English translation about the following June, but the translation issue will carry the December date. When ordering any volume or particular issue of a Consultants Bureau journal, please specify the date and, where applicable, the volume and issue numbers of the original Russian. The material you will receive will be a translation of that Russian volume or issue.

Subscription
$75.00 per volume (6 issues)
2 volumes per year
(Add $5 for orders outside the United States and Canada.)

Single Issue: $30
Single Article: $15

CONSULTANTS BUREAU, NEW YORK AND LONDON

227 West 17th Street
New York, New York 10011

Davis House
8 Scrubs Lane
Harlesden, NW10 6SE
England

Published monthly. Second-class postage paid at Jamaica, New York 11431.

SOVIET ATOMIC ENERGY

A translation of *Atomnaya Énergiya*
Translation published August, 1972

Volume 32, Number 2 February, 1972

CONTENTS

	Engl.	Russ.
Organization of Radiation Monitoring at Nuclear Power Stations – A. A. Il'khman, V. M. Dedkov, and A. N. Romanov	121	107
Radiation Safety Conditions in Uranium Mine Drifting Operations – N. I. Chesnokov, Yu. A. Lebedev, and I. V. Pavlov	124	111
Thermodynamic Properties of Uranium–Aluminum Alloys – V. A. Lebedev, V. I. Sal'nikov, I. F. Nichkov, and S. P. Raspopin	129	115
Production of Ac^{227} and Th^{228} Isotopes by Irradiation of Radium in the SM-2 Reactor – Z. K. Karalova, R. N. Ivanov, B. F. Myasoedov, L. M. Rodionova, Z. I. Pyzhova, S. M. Kalebin, and V. Ya. Gabeskiriya	133	119
Interaction of High-Energy Radiation with Matter – V. S. Barashenkov, N. M. Sobolevskii, and V. D. Toneev	137	123
Plasma Accumulation through Ionization of Residual Gas in an Electromagnetic Trap – Yu. I. Pankrat'ev, M. G. Nozrachev, O. A. Lavrent'ev, B. G. Safronov, V. A. Naboka, and E. F. Ponomarenko	144	131
Nonlinear Theory for the Excitation of Regular Oscillations by a Relativistic Electron Beam – V. I. Kurilko, A. P. Tolstoluzhskii, and Ya. B. Fainberg	150	137
Verification of the Neutron Diffusion for a Medium with Channels (Lattice of Channels with Large Transverse Dimensions) by Means of the Pulse Method – I. F. Zhezherun	155	143
ABSTRACTS		
Uranium Extraction from Low-Grade Silicate Ore with the Aid of Thiobacteria – E. G. Kuznetsova and I. P. Kuligina	165	153
Effect of Noise Currents on Measuring Circuits of Reactor Channel Control Systems – A. G. Ivanov and V. M. Matyukhin	166	153
Heat Exchange Crisis in the Boiling-up of Liquids – A. N. Vasil'ev and P. L. Kirillov	167	154
An Approximate Method for Calculating Fast Neutron Shields – B. S. Sychev	168	155
A Universal Expression for the Characteristics of the Scattered Electron Distribution as a Function of the Medium and the Initial Electron Parameters – V. V. Arutyunov, V. F. Baranov, and A. G. Zrazhun	169	156
Calculation of Bremsstrahlung Intensity by the Monte Carlo Method – V. V. Arutyunov and V. F. Baranov	170	156
Dosimetric Characteristics of Neutron Threshold Detectors – T. V. Koroleva, K. K. Koshaeva and S. N. Kraitor	170	157
LETTERS TO THE EDITOR		
Short-Term Reactor Cooling – S. O. Slesarevskii, M. N. Korotenko, M. M. Nazarchuk, D. T. Pilipets, and S. S. Stel'makh	172	159
Fast Neutron Fluxes in Experimental Channels of the MR Reactor – A. V. Borodin, V. I. Vikhrov, V. F. Krasnoshtanov, V. N. Perevezentsev, and G. E. Shatalov	175	161

CONTENTS

(continued)

	Engl.	Russ.
Heat-Transfer Properties of Cermet Compositions of the System Al_2O_3 – Mo – V. A. Osipova and Kh. A. Kyaar	177	162
Carbon Electrotransference in Beryllium – V. P. Gladkov, V. S. Zotov, and D. M. Skorov	179	163
Thermodynamics of the Extraction of Plutonium(IV) from Perchloric and Nitric Acid Solutions in the Presence of Oxalic Acid – A. S. Solovkin and A. I. Ivantsov	182	164
Simulation Experiment on the Water–Oil Contact in Exploration of Stratal Fresh Water by Recording Delayed Neutrons – Ya. E. Kostyu, A. P. Osipenko, and V. A. Shkoda-Ul'yanov	184	166
Separation of Liquid Mixtures by Thermodiffusion through an Electric Field – V. P. Kuchinov, B. I. Nikolaev, and A. A. Tubin	187	167
Separation of Isotopes of Nitrogen and Hydrogen in the Photodissociation of Ammonia – B. U. Utirov, G. M. Panchenkov, V. K. Korovkin, and Yu. G. Basov	189	169
Operating Characteristics of Dispersive Air-Equivalent Scintillators – G. P. Volosyuk, S. P. Vershinina, O. A. Gunder, L. S. Prokof'eva, and L. V. Sigalova	192	171
Electrical Discharge in Radioactive Dielectrics – V. V. Gromov and V. V. Surikov	194	172
Isotropic Neutron Source Using the LUÉ-25 Linear Electron Accelerator – V. P. Kovalev, V. P. Kharin, V. V. Gordeev, and V. I. Isaev	196	173
Calculation of the Yield of D–T Neutrons with Periodic Replenishment of the Target with Tritium – V. T. Tustanovskii	198	175
Relative Probability of Am^{242} Beta Decay – V. Ya. Gabeskiriya	201	177
Slow Neutron Capture Cross Section of Pa^{231} – B. M. Aleksandrov, M. A. Bak, A. S. Krivokhatskii, and E. A. Shlyamin	203	178
Cf^{249} Fission Cross Section for Fast and Thermal Neutrons – B. I. Fursov, Kh. D. Androsenko, V. I. Ivanov, V. G. Nesterov, G. N. Smirenkin, L. V. Chistyakov, and V. M. Shubko	205	178
An Unidentified Alpha Activity of Thorite – K. A. Petrzhak, M. I. Yakunin, and G. M. Ter-Akop'yan	207	179
INFORMATION		
Startup of the Third Power Unit of the Novaya Voronezh Nuclear Power Station	209	181
CHRONICLES		
XXI Session of the Comecon Permanent Commission (PKIAÉ SÉV) – A. Panasenkov	210	182
Collaboration Logbook	212	182

The Russian press date (podpisano k pechati) of this issue was 1/24/1972. Publication therefore did not occur prior to this date, but must be assumed to have taken place reasonably soon thereafter.

ORGANIZATION OF RADIATION MONITORING AT NUCLEAR POWER STATIONS

A. A. Il'khman, V. M. Dedkov, and A. N. Romanov

UDC 621.039.766

The basis for the organizational and functional structure of radiation monitoring at domestic nuclear power stations was developed under the influence of traditions which grew up during the period the first nuclear power stations were built. At the present time, the requirements for radiation monitoring are set fourth in "Health Rules for Nuclear Power Station Design" (Medgiz, Moscow (1968)). According to these rules, a radiation monitoring service, which is organizationally an independent subdivision, is provided at a nuclear power station. The functional structure is characterized by the existence of an independent, sufficiently many-sided system consisting of subsystems, each of which is provided for the solution of definite problems in the field of radiation monitoring.

One of the aspects of the accepted functional structure related to the nature of the usage of information circulating within the radiation monitoring sphere is discussed below. Obtaining the necessary information is accomplished in three basic ways: by remote measurements, by measurements with portable instruments, and by sample collection. Remote measurements provided continuous data on the radiation situation in a nuclear power station; portable instruments permit more detailed information about radiation levels for a specific monitored unit; sample collection enables one to obtain quantitative and qualitative characteristics for individual radiation parameters.

Of greatest interest is the information acquired by remote monitoring. In domestic nuclear power stations, remote monitoring is centralized and, as a rule, is done at a separate panel attended by a special operator from the radiation monitoring service. A diagram of the main information channels for this panel is shown in Fig. 1. The content of the information reaching the operator and the nature of its use is shown in Table 1.

Analysis of the data presented in Table 1 indicates that the main responsibility of the operator at the radiation monitoring panel is essentially the recording of events and the transfer of required information to duty personnel of the radiation monitoring service and to operating personnel of the technical subsections of the station. Although obtaining information about various radiation anomalies, the operator does not have the capability of doing anything about their cause. In such situations, all necessary measures are taken by the appropriate personnel of the technical departments. Thus one observes a definite break between the volume and amount of information acquired by the operator and his capabilities, which transforms a basic element of the system (panel and operator) into an intermediate link intended for the transfer of information to a location where it can be used actively, i.e., to the control system of the nuclear power station.

There is a fundamental possibility for simplifying the radiation monitoring system based on the transfer of the appropriate information directly to personnel able to take the necessary measures to bring about control of a situation. To accomplish this, it is advisable to include an independently functioning radiation monitoring system within the complex control system of a nuclear power station in the status of a subsystem. This step makes it possible to furnish the appropriate information circulating in the sphere of the system under discussion to the operators at the power station panels, i.e., to the personnel directly controlling the technical processes at the station.

In nuclear power stations at the present time, information and computing systems with organized display for the operator are used for automation of the basic technical processes. The appropriate information from the radiation monitoring subsystem should be introduced into such a system. The results will

Translated from Atomnaya Énergiya, Vol. 32, No. 2, pp. 107-109, February, 1972. Original article submitted March 26, 1971.

TABLE 1. Characteristics of Radiation Monitoring Panel at a Nuclear Power Station

Information flow number (as in Fig. 1)	Information content	Information purpose	Role of operator in obtaining (using) information	Remarks
1	Values of γ-ray dose rate and aerosol concentrations in attended and semi-attended locations; gas concentrations in attended, semi-attended, and unattended locations of the controlled area	Charactize radiation situation	Take instrument readings, control individual elements of monitoring system	—
2	Specific activity values for the process media in the main loops	Characterize radiation status of loops and equipment	The same	—
3	Concentration of radioactive materials in liquid and gaseous wastes discharged outside the limits of nuclear power station	Prevent discharge of radioactive materials from nuclear power station in amounts greater than permissible	Take instrument readings, calculate daily discharge	—
4	Audible and visible alarms for radiation levels above permissible in attended locations of controlled area	Warn personnel of presence of radiation hazard	Inform (by telephone) operating personnel of the technical departments about the appearance of a radiation anomaly; record the anomalous event	Area alarms are activated automatically
5	Radiation levels in unattended locations, specific activity of process media and of wastes discharged outside limits of nuclear power station	Inform operating personnel of technical departments about the appearance of a radiation anomaly	The same	Warning on the engineering panels about a change in basic radiation parameters is given automatically
6	Radiation levels in attended, semi-attended, and unattended locations of the controlled area	Inform duty personnel of the radiation monitoring service about radiation levels in the areas	—	Information is telephoned by the operator on request from the duty personnel of the radiation monitoring service
7	Amount of radioactive material discharged from the nuclear power station into the environment	Warn personnel in the external monitoring group about above-permissible discharges	Record data	Information transmitted by telephone

be: an increase in operational control of a nuclear power station, which is very important because the increase in specific power of reactor units imposes increasingly rigorous requirements on safety problems; a reduction in the number of service personnel at a nuclear power station because of the elimination of operators for the radiation monitoring panel; economies in the area of panel locations because the secondary equipment for radiation monitoring can, in this case, be placed in the general circuit for technical control panels and not in a separate arrangement, etc.

The proposed reorganization of functional structure involves changes in other important problems of radiation monitoring with the principal ones being: the volume of radiation monitoring, the degree of automation of information collection and analysis, the volume and quality of information displayed to control panel operators, and construction principles for groups of technical systems. The organizational structure of the radiation monitoring service may also undergo certain changes.

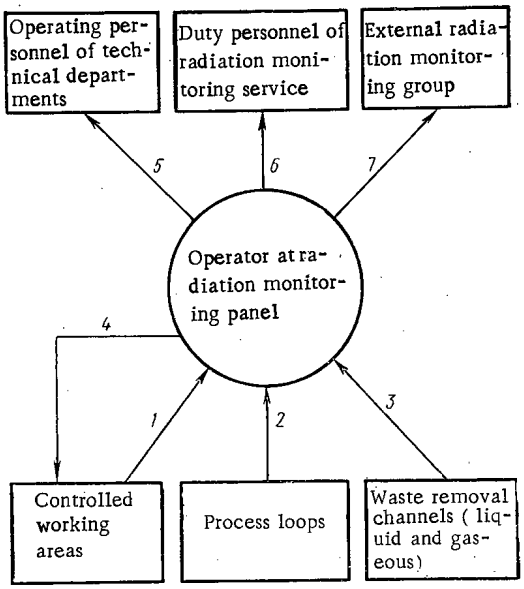

Fig. 1. Diagram of main information channels to the radiation monitoring panel at a nuclear power station. (Numerals indicate the information flow number.)

In conclusion, it should be said that questions of cost were not a deciding factor in the construction of the first operating nuclear power stations which served as the basis for the creation of radiation monitoring systems for subsequent nuclear power stations. Thus the presently accepted organizational and functional structure was not only acceptable but also useful – it made it possible to obtain rather complete data on all aspects of radiation monitoring. Subsequent development of nuclear power in this country, associated with the construction of a large number of commercial nuclear power stations, moves into the forefront the requirement of reduction in capital expenditures for station construction along with the requirement for increase in operational reliability. From this viewpoint, the proposed solution can have a decided effect.

RADIATION SAFETY CONDITIONS IN URANIUM MINE DRIFTING OPERATIONS

N. I. Chesnokov, Yu. A. Lebedev, and I. V. Pavlov

UDC 613.6:621.039

Radon is liberated constantly from the walls of the mine faces and sidewalls and from broken-up mine muck, rubble, ore, and gangue, and gets into the air circulating through underground uranium ore mines at a rate of $2 \cdot 10^{-8}$ to $5 \cdot 10^{-8}$ Ci/sec·m^2 [1].

Artificial ventilation is built into all mines with the purpose of minimizing the radiation effects of the radon given off, and even more so the radiation effects of the radon daughters: Po^{218} (RaA), Pb^{214} (RaB), and Bi^{214} (RaC), with their short half-lives. The intensive ventilation, while removing the randon present, also severely upsets the radioactive equilibrium between the radon and the radon daughters. When the disturbance of this equilibrium is taken into account, the degree of radiation effects of the mixture of radon daughters can be estimated from the amount of latent energy of decay.

The energy is determined from the formula [2]:

$$\varphi = K_\varphi (0.1C_{\mathrm{RaA}} + 0.5C_{\mathrm{RaB}} + 0.4C_{\mathrm{RaC}}), \quad (1)$$

where φ is the latent energy in MeV/m^3; C_{RaA}, C_{RaB}, C_{RaC} are the respective concentrations of each of the radon daughters in Ci/m^3; K_φ is a conversion factor equal to $1.3 \cdot 10^{15}$ MeV/m^3 [2].

The yearly average allowable amount of latent energy in the mine atmosphere φ_{YAC} is $1.3 \cdot 10^8$ MeV/m^3 if the miners have spent not more than 15 to 17 years on the job [2].

Nevertheless, there have been cases when uranium energy reached a level of $2 \cdot 10^{11}$ to $3 \cdot 10^{11}$ MeV/m^3 [3] in unventilated mine areas, i.e., a level at which miners working in such an atmosphere would be subjected to radiation exposure several times in excess of the critical allowable yearly dose.

The latent energy can be kept down to allowable levels, as a rule, through high-intensity ventilation. But when the galleries driven through the mine are very long and when a considerable amount of radon is liberated into the mine atmosphere, it is not always possible to maintain the required conditions throughout the mine working areas. In those cases, the time the miners are permitted to stay at various mine work sites must be limited, or air-cleaning filters and individual respirators must be put to use.

Experience in driving mine galleries has taught that miners spend most of their time in areas within 30 to 40 meters of the stopped mine face (Fig. 1). This means that radiation protection calculations can be reliably oriented on the basis of the average latent energy in the mine face area $\varphi_{\mathrm{av}}^{\mathrm{face}}$. This, in combination with individual dosimeter badges, will provide adequate radiation safety for the miners.

The pattern of variations in the latent energy in mine drift work is a highly intricate one, and depends on a host of factors, those of greatest importance being: a) the intensity and position of the sources giving off the radon; b) the radon concentration and the latent energy at the ventilation air intake point; c) the amount of air supplied to the mine working site and the aerodynamic characteristics of the ventilation system (volume swept in ventilation, air leakage distribution in the vents and ducting, distance from end of vent to mine face breast, etc.).

Most of the determining factors vary with time over fairly broad ranges. Moreover, some of the factors have received inadequate study (e.g., the degree of precipitation of radon decay products in the ventilation ductwork and on the walls of the mine working area). This necessitates introduction of certain

Translated from Atomnaya Énergiya, Vol. 32, No. 2, pp. 111-114, February, 1972. Original article submitted April 28, 1971; final revision submitted July 22, 1971.

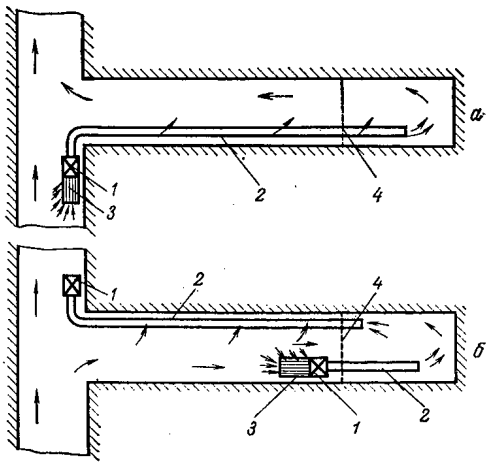

Fig. 1

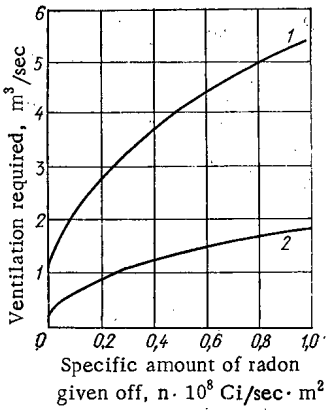

Fig. 2

Fig. 1. Arrangement for ventilation of mine drfit area in forced ventilation (a) and in combined ventilation (b): 1) fans; 2) ducting; 3) aerosol filters; 4) boundary of mine face area.

Fig. 2. Dependence of amount of air needed to ventilate mine face area on specific amount of radon given off: 1) without aerosol filter; 2) with aerosol filter; $C_{in} = 3 \cdot 10^{-7}$ Ci/m^3; $\varphi_{in} = 9 \cdot 10^7$ MeV/m^3.

assumptions into the calculations, and specifically leaving out of account precipitation of radon decay products, ignoring air coming from pneumatic tools, etc.

The difficulties encountered in calculating the average radon concentrations and the latent energy can be eliminated by using the following ratios:

$$Z_{Rn} = \frac{C_j - C_{in}}{C_{av} - C_{in}}, \tag{2}$$

$$Z_{\varphi} = \frac{\varphi_j - \varphi_{in}}{\varphi_{av} - \varphi_{in}}, \tag{3}$$

which we shall term the ventilation indices for radon Z_{Rn} and for the latent energy Z_{φ}.

The ratios Z_{Rn} and Z_{φ} provide the link with the volume-averaged concentration of radon and the latent energy in the mine working area C_{av}, φ_{av} and the corresponding values in the emanating jet stream C_j, φ_j. These indices characterize the rate of air exchange between the various mining areas and the arrangement of radon evolution sources in the mine. They are virtually independent of the air turnover time in the mine areas.

Consider the equations characterizing the time variation process of the amount of radon and of the latent energy in the mine areas:

$$W \frac{dC_{av}}{dt} = D - Q(C_j - C_{in}), \tag{4}$$

$$W \frac{d\varphi_{av}}{dt} = W\lambda_{\varphi}(K_{\varphi} C_{av} - \varphi_{av}) - Q(\varphi_j - \varphi_{in}). \tag{5}$$

Here W is the volume of the mine area swept out in ventilation in m^3; Q is the amount of air supplied to the mine working areas in ventilation in m^3/sec; D is the flow of radon per sec from the mine working areas in Ci/sec; λ_{φ} is an empirical constant characterizing the fall-off in latent energy, and is equal to $\approx 3 \cdot 10^{-4}$ sec^{-1} [4].

In Eq. (4), radon decay is ignored, since the radon decay constant is relatively small ($\lambda_{Rn} = 2.1 \cdot 10^{-6}$ sec^{-1}), while the air turnover time in the mine working areas is usually not longer than 10^4 sec.

The first term in the right-hand member of Eq. (5) characterizes the buildup of latent energy in response to the formation of radon daughters, and their subsequent decay, while the second term in the equation characterizes the process by which the latent energy changes through increment and loss of radon daughters added or carried off by the ventilation air stream.

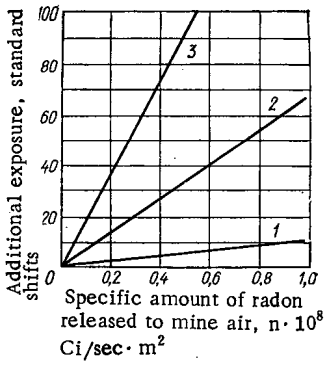

Fig. 3. Dependence of additional exposure experienced by miners on specific amount of radon given off in continuous ventilation of mine face area: 1) for 1 h; 2) for 2 h; 3) for 3 h.

Substitution of the values of C_j and φ_j from Eqs. (2) and (3) into Eqs. (4) and (5) yields, for steady-state conditions:

$$C_{av} = C_{in} + \frac{D}{QZ_{Rn}}, \tag{6}$$

$$\varphi_{av} = \frac{\varphi_{in}}{1 + \frac{W\lambda_\varphi}{QZ_\varphi}} + \frac{K_\varphi C_{av}}{1 + \frac{QZ_\varphi}{W\lambda_\varphi}}. \tag{7}$$

The numerical values of Z_{Rn} and Z_φ can be determined experimentally either by using laboratory simulation models or by observing natural conditions.

In mine drifting work, Z_{Rn} and Z_φ depend primarily on the position of the sources of emanation and air leaks in the ducting. At the mine face the distance from the end of the ductwork to the breast of the mine face is also of essential importance. The greater this distance, the smaller Z_{Rn} and Z_φ will be, and the worse the ventilation conditions will be at the mine face and in the mine generally.

The average level of irradiation of the mine worker during a shift is determined by the amount of latent energy of the radioactive aerosols:

$$\varphi_{sh} = \varphi_{av}^{face}\delta + \varphi_{av}(1-\delta), \tag{8}$$

where δ is the relative residence time of the miner at the mine face. Since $\delta > 0.8$ as a general rule, efforts must be made to increase the quantity of air supplied directly to the mine face Q_{face} in the event that it becomes impossible to attain the condition $\varphi_{av} \leq \varphi_{YAC}$.

Curve 1 in Fig. 2 illustrates the dependence of the amount of ventilation needed to keep the amount of latent energy from rising above 0.8 φ_{YAC} on the specific amount of radon given off at the mine face from a cross sectional area 8 m^2 over a length of 40 m, at $C_{in} = 3 \cdot 10^{-7}$ Ci/m^3, $\varphi_{in} = 0.9 \cdot 10^8$ MeV/m^3, $Z_{Rn} = 1.0$, $Z_\varphi = 1.5$.

Since the capacity of the local ventilation fans is not greater than 3 to 5 m^3/sec, air leakages in the ductwork make it difficult to supply more than 2 to 3 cubic meters of air per second to a mine face of considerable extent. It is for that reason that it does not always prove possible, in the case of mine workings subject to heavy radon emanation, to keep up adequate radiation safety conditions solely by means of ventilation. If the radon concentration and the latent energy are high in the air intake area, recourse to aerosol filters incorporating FP particle-trapping fabric will be mandatory [5]. The effect achieved through the use of these filters is illustrated by Fig. 2, curve 2. Calculations of the amount of ventilation required when the filters are used can be based on Eq. (7), with the substitution $\varphi_{in} = 0$.

To remove radon decay products filters for cleanup of mine air must combine a high degree of cleanup with a high dust capacity, and must be lightweight, compact, nonhygroscopic, and offer comparatively little aerodynamic resistance. Experimental prototypes of such filters have been through production tests at several uranium mines, where results showed over 90% efficiency in cleaning up the mine air, both in terms of coarse-disperse mine dust and in terms of radon decay products.

The filters consist of separate cylindrical sections extending 2 meters in length. The required dust capacity (to 0.3 kg/m^2) is achieved through the use of Lavsan [Dacron] fibers.

The most favorable conditions for the effective use of these filters is in the ventilation of mine areas by the combined method (see Fig. 1b), which offers some distinct advantages over the forced-flow method (particularly the fact that gaseous products of ignited explosives are removed from the air with much greater dispatch).

This means that ventilation incorporating the use of aerosol filters, when required, will in principle meet the needs of radiation safety in terms of the miners' working conditions.

But this inference is valid only for the case of steady-state ventilation conditions. A serious deterioration of the radiation energy situation at the mine face could result from outage of a local ventilation fan.

In order to evaluate the hazard involved in local-ventilation fans failing or being switched off, we consider the differential equations describing the process by which the amount of radon and the latent energy in the mine change, when there is no flow of air whatever except for the diffusion process:

$$W\frac{dC_{av}}{dt}=D(t)-WC_{av}\lambda_{Rn}, \tag{9}$$

$$W\frac{d\varphi_{av}}{dt}=W\lambda_{\varphi}(K_{\varphi}C_{av}-\varphi_{av}). \tag{10}$$

A rapid increase in the radon concentration after the shutdown of a fan leads to a fall-off in the radon flow, by the law [6]

$$D(t)=S\sqrt{\lambda_{Rn}K_d}(C_{\infty}-C_{av}), \tag{11}$$

where S is the surface area of the exposed mine area in m^2; K_d is the radon diffusion coefficient in the rock with porosity taken into account in m^2/sec; C_{∞} is the radon concentration in the pores of the rock at a depth at which radon diffusion into the mine atmosphere is virtually absent in Ci/m^3.

When the fan is operating, we have $C_{av} \ll C_{\infty}$ and $D = S\sqrt{\lambda_{Rn}K_d}C_{\infty}$. Denoting the ratio of the exposed mine area periphery to its cross section as $\varkappa$, we obtain

$$S=\varkappa W,$$

$$D(t)=D-\varkappa W\sqrt{\lambda_{Rn}K_d}C_{av}. \tag{12}$$

The solutions of Eqs. (9) and (10), with the value of D(t) from Eq. (12) taken into account, with some simplifications, become

$$C_{av}=C_{av}^0e^{-(\lambda_{Rn}+\varkappa\sqrt{\lambda_{Rn}K_d})(t-t_0)}+\frac{D}{W(\lambda_{Rn}+\varkappa\sqrt{\lambda_{Rn}K_d})}[1-e^{-(\lambda_{Rn}+\varkappa\sqrt{\lambda_{Rn}K_d})(t-t_0)}], \tag{13}$$

$$\varphi_{av}=\varphi_{av}^0e^{-\lambda_{\varphi}(t-t_0)}+K_{\varphi}C_{av}^0[e^{-(\lambda_{Rn}+\varkappa\sqrt{\lambda_{Rn}K_d})(t-t_0)}-e^{-\lambda_{\varphi}(t-t_0)}]+\frac{K_{\varphi}D}{W(\lambda_{Rn}+\varkappa\sqrt{\lambda_{Rn}K_d})}\left\{1-e^{-\lambda_{\varphi}(t-t_0)}+\frac{\lambda_{\varphi}}{\lambda_{\varphi}-(\lambda_{Rn}+\varkappa\sqrt{\lambda_{Rn}K_d})}[e^{-\lambda_{\varphi}(t-t_0)}-e^{-(\lambda_{Rn}+\varkappa\sqrt{\lambda_{Rn}K_d})(t-t_0)}]\right\}. \tag{14}$$

Here C_{av}^0 and φ_{av}^0 are the average radon concentration and average latent energy at the instant t_0 when the fan is shut off.

If the ventilation conditions in the mine area at the time the fan was shut off are ascertained, then the values of C_{av}^0 and φ_{av}^0 can be found from Eqs. (6) and (7).

However, it is not possible to give a sufficiently exact description of the process of change in C_{av} and φ_{av} after the fan is shut off, since the values of Z_{Rn} and Z_{φ} are not constant for the steady state in the general case.

Proper organization of radiation protection services nevertheless calls for knowledge of the transient period of the ventilation process. The transient period may be much longer than W_{face}/Q_{face} when the end of the ductwork at the mine face area is an appreciable distance away from the breast of the mine face. Assuming Z_{Rn} and Z_{φ} to be more or less equal to their steady-state values in that case, and solving Eqs. (4) and (5) on that basis, we get

$$C_{av}\approx C_{av}^{st}e^{-Z_{Rn}\frac{Q}{W}(t-t_{st})}+C_{av}^0[1-e^{-Z_{Rn}\frac{Q}{W}(t-t_{st})}] \tag{15}$$

$$\varphi_{av}\approx\varphi_{av}^0[1-e^{-\left(\lambda_{\varphi}+\frac{Q}{W}Z_{\varphi}\right)(t-t_{st})}]+\varphi_{av}^{st}e^{-\left(\lambda_{\varphi}+\frac{Q}{W}Z_{\varphi}\right)(t-t_{st})}+\frac{K_{\varphi}\lambda_{\varphi}(C_{av}^{st}-C_{av}^0)}{\lambda_{\varphi}+\frac{Q}{W}(Z_{\varphi}-Z_{Rn})}[e^{-Z_{Rn}\frac{Q}{W}(t-t_{st})}-e^{-\left(\lambda_{\varphi}+\frac{Q}{W}Z_{\varphi}\right)(t-t_{st})}]. \tag{16}$$

All of the parameters in Eqs. (15) and (16) refer to the mine face area, while C_{av}^{st} and φ_{av}^{st} refer to the average radon concentration and average latent energy at the time t_{st} when the fan is turned on as ascertainable through Eqs. (13) and (14).

The approximate amount of additional radiation exposure (as received in units of standard shifts)* suffered by miners continuing to work in blind drifts with the local-ventilation fan shut off, is shown in Fig. 3. Radiation exposure during the transient period of the field of latent energy, after the fan has been switched on, is not taken into account. The radon concentration and the latent inert energy at the time the fan shuts down are respectively $3 \cdot 10^{-7}$ Ci/m^3 and $1.3 \cdot 10^8$ MeV/m^3, and the remaining calculated parameters are: $\varkappa = 1.4$, $K_d = 5 \cdot 10^{-7}$ m^2/sec.

It is clear from Fig. 3 that complete cessation of air intake for even a few hours may result in additional exposure to the miners comparable to the annual limiting tolerance dose, in the case of mine areas where large amounts of radon emanate. This emphasizes the need for constant inspection and monitoring of the performance of ventilation equipment and prompt evacuation of personnel from the mine face in the event of fan stoppage. When these conditions are met, radiation safety conditions in mine drift work can be realized successfully with the aid of existing technical equipment.

LITERATURE CITED

1. A. V. Bykhovskii, Public Health Problems in Underground Mining of Uranium Ore [in Russian], Medgiz, Moscow (1963).
2. Radiation Safety Rules NRB–69 [in Russian], Atomizdat, Moscow (1970).
3. A. Rice, Mines Mag., 47, 44 (1957).
4. I. I. Gusarov and V. K. Lyapidevskii, At. Énerg., 10, 64 (1961).
5. A. V. Bykhovskii, V. D. Nikolaev, and N. I. Chesnokov, in: Public Health and Labor Safety Problems at Uranium Mines and Uranium Ore Beneficiating Plants [in Russian], edited by G. M. Parkhomenko, O. S. Andreeva, and V. I. Bad'in, Atomizdat, Moscow (1971), p. 12.
6. A. S. Serdyukova, Yu. T. Kapitanov, and M. P. Zavodskaya, Izv. Akad. Nauk SSSR, Fizika Zemli, 7, 123 (1965).

*The standard shift corresponds to the radiation exposure experienced by a miner working in the mine atmosphere where latent energy is at the level of $1.3 \cdot 10^8$ MeV/m^3, over a seven-hour work shift.

THERMODYNAMIC PROPERTIES OF URANIUM–ALUMINUM ALLOYS

V. A. Lebedev, V. I. Sal'nikov, I. F. Nichkov, and S. P. Raspopin

UDC 536.7+669.715'822

Uranium–aluminum alloys are widely used in modern reactors. Their thermodynamic properties must be known for a quantitative description of the various interactions in which these alloys participate From the difference in the dissolution heats of UAl_2, UAl_3, and UAl_4 and corresponding component mixtures M. I. Ivanov et al., [1] determined the heats of formation of uranium–aluminum compounds (ΔH°_{298}) which were found to be 22.3 ± 2.4, 25.2 ± 2.2, and 31.2 ± 3.1 kcal/mole respectively and in good agreement with the results of low-temperature calorimetric measurements [2]. However, the results of [2] obtained by measuring the emf between uranium and its aluminum solid solutions differ considerably from calorimetric data.

Below are reported the results of a study of the thermodynamic properties of UAl_4, UAl_3, and UAl_2 uranium–aluminum liquid solutions and compounds, and of the temperature dependence of solubility of uranium in molten aluminum.

EXPERIMENTAL METHOD

We measured the emf of galvanic cells:

$$U_{sol}(KCl–NaCl \text{ or } KCl–LiCl + 3\% \text{ by weight } UCl_3)\,U–Al.$$

TABLE 1. Activity Factor of Uranium in Aluminum Alloys (Standard state: γ uranium)

T°K	E, mV: experimental data	E, mV: with reference to γ uranium	x_U	$\gamma_U \cdot 10^4$
934	377,2	379,0	0,0145	0,66
934	370,7	372,5	0,0156	0,60
958	383,0	384,4	0,0076	1,1
959	354,6	356,0	0,0157	1,2
961	353,6	355,0	0,0205	1,3
980	370,3	371,3	0,0100	1,9
980	358,8	359,8	0,0155	1,9
1077	365,8	365,8	0,0083	8,8
1080	347,7	347,7	0,0140	9,7
1085	336,3	336,3	0,0199	10
1144	336,0	336,0	0,0200	18
1147	322,3	322,3	0,0275	20

TABLE 2. Thermodynamic Characteristics of the Formation of Uranium–Aluminum Liquid Solutions at 1000°K

x_U	a_U	a_{Al}	$-\Delta H$, cal/g-atom	$-\Delta S^{ex}$, eu/g-atom	$-\Delta G^{ex}$, cal/g-atom
0,005	$1{,}27 \cdot 10^{-6}$	0,995	166	84	82
0,01	$2{,}54 \cdot 10^{-6}$	0,99	332	168	164

Ions of the potential-determining element were added by means of anodic dissolution of uranium to a melt of dehydrated alkali metal chlorides. Alloys of the desired composition were prepared directly in the cell by adding accurately weighted amounts of aluminum (99.97%) and finely ground, free from oxide films uranium shavings (99.6%). The alloys were held in small beryllium oxide crucibles. Electrical connections to uranium and the alloy were made of titanium to prevent distortion of the results by thermoemf. The experimental cell was described in [3]. The emf measurements were made with a high-resistance potentiometer. In investigating uranium solutions in aluminum, the equilibrium was studied at one temperature only in each experiment since the alloy composition has been observed to change with time probably as a result of the $Al + U^{3+} \rightarrow U(Al) + Al^{3+}$ reaction. The contact of melt with metallic uranium shifts the equilibrium of this reaction in the direction of higher uranium content as observed in practice. After the emf reached a steady-state value, as indicated by the fact that in a span of thirty minutes it did not change by more than 0.2–0.3 mV, the crucible was extracted from the cell and cooled, the alloy regulus was cleaned and analyzed for uranium content. The temperature dependence of the emf was studied in the investigation of two-phase uranium

Translated from Atomnaya Énergiya, Vol. 32, No. 2, pp. 115-118, February, 1972. Original article submitted March 22, 1972.

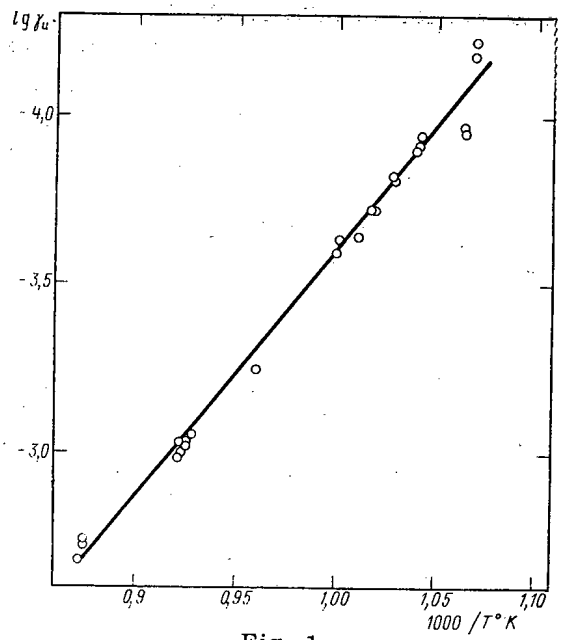

Fig. 1

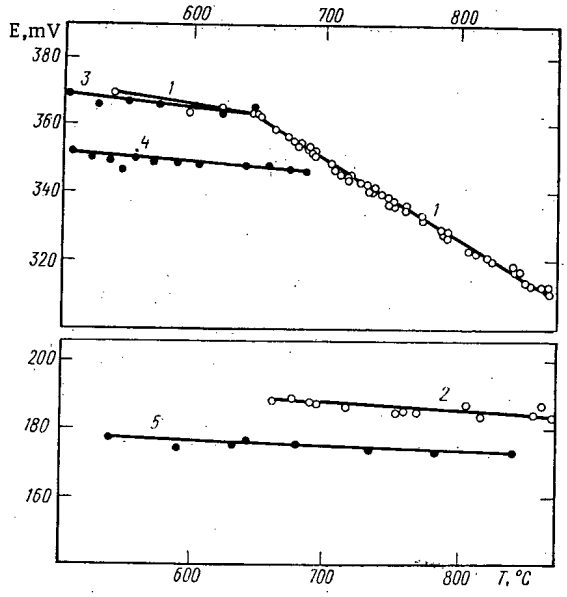

Fig. 2

Fig. 1. Temperature dependence of γ uranium activity factor in aluminum solutions.

Fig. 2. Temperature dependence of emf between γ uranium and its aluminum alloys. Uranium content in % by weight: 1) 25-40, 2) 77-80, 3) 10, 4) 71.4, 5) 77 (1 and 2 are our data, 3-5 were adopted from [2]).

TABLE 3. Partial Thermodynamic Characteristics of γ Uranium in Aluminum Alloys

Data	T, °C	Uranium content in alloys, % by weight	Phase composition	Coefficients of E= a+ bT		$-\Delta\bar{H}_U$, kcal/g-atom	$-\Delta\bar{S}_U$, eu/g-atom	$-\Delta\bar{G}_U$, 1000° K, kcal/g-atom
				a	$-b\cdot 10^3$			
Our	870—730	25—40	$1+UAl_3$	0,558	0,216	38,6±0,8	14,9±0,8	23,6±0,1
	730—640	25—40	$1+UAl_4$	0,600	0,258	41,5±0,8	17,8±0,8	23,6±0,1
	640—537	25—40	$Al+UAl_4$	0,420	0,059	29,1±2,3	4,1±2,8	(25,0±0,3)
	880—660	77—80	UAl_3+UAl_2	0,201	0,014	13,9±2,8	1,0±2,8	(12,9±0,4)
[2]	401—639	10	$Al+UAl_4$	0,406	0,046	28,1±0,6	3,2±0,8	(24,9±0,1)
	399—706	71,4	UAl_4+UAl_3	0,351	0,003	24,3±0,6	0,2±0,6	24,1±0,1
	442—840	77	UAl_3+UAl_2	0,197	0,021	13,6±0,6	1,5±0,6	12,1±0,1

– aluminum alloys. As trustworthy were taken emf values which in the course of an hour did not change by more than 0.2 mV and could be reproduced to the same degree of accuracy as the temperature was raised and lowered. The reproducibility was ±1 mV in separate experiments with liquid two-phase alloys and somewhat worse (~3-4 mV) in experiments with solid solutions. The experiments were conducted in an atmosphere of purified argon. The experiment temperature was measured by a Chromel–Alumel thermocouple, calibrated against melting points of pure metals, and maintained constant to within ±0.5° by an electronic temperature regulator.

RESULTS AND DISCUSSION

The emf's measured between uranium and its liquid solutions in aluminum at different temperatures are listed in Table 1. Several uranium modifications are stable in the investigated temperature interval. As a standard modification we have taken γ uranium. At temperatures at which α or β uranium are stable we used the correction

$$-\Delta E = (RT/zF)\ln a^{\circ},$$

where a° is the uranium activity with reference to γ uranium. The correction was calculated using the well-known method [4], knowing the heats and temperatures of polymorphous uranium transformations [5]. For

TABLE 4. Thermodynamic Characteristics of the Formation of Uranium–Aluminum Compounds of α Uranium and Solid Aluminum at 900°K

Compound	$-\Delta\bar{H}_U$, kcal/g-atom	$-\Delta\bar{S}_U$, eu/g-atom	$-\Delta\bar{G}_U$, kcal/g-atom	$-\Delta H$, kcal/g-atom	$-\Delta S$, eu/g-atom	$-\Delta G$, kcal/g-atom	a_{Al}	$a_U \cdot 10^6$
UAl_4	29,7	4,3	25,83	5,94	0,86	5,16	1,00	0,52
UAl_3	29,3	4,1	25,61	7,39	1,06	6,45	0,96	0,60
UAl_2	12,1	—1,8	13,72	7,92	0,74	7,26	0,10	460

750, 700, 650, and 600°C the correction ΔE was 0.4, 1.2, 2.2, and 3.5 mV respectively. These were added to the experimentally found emf values, i.e., the alloy emf's were reckoned with reference to γ uranium. Using the well-known relations [3], the uranium activity factor in aluminum alloys was calculated from the measured emf values, the temperature, and the results of analysis.

The studied solutions exhibit a characteristic deviation of the uranium activity from the Raoult law, which decreases with increasing temperature. To within $\pm 10\%$ γ_U remains constant over the entire investigated range of concentrations and temperatures. The temperature dependence of the uranium activity factor is shown in Fig. 1. The experimental results plotted in $\log \gamma_U - 1000\ T/°K$ coordinates fit a straight line whose equation, found by the method of least squares, is

$$\lg \gamma_U = 3.672 - \frac{7266}{T} \pm 0.051. \quad (1)$$

From this we can find the excess partial thermodynamic characteristics of uranium in aluminum alloys [6]. The following figures were found:

$$\Delta\bar{G}_U^{ex},\ 1000°K = -16.4 \pm 0.23 \text{ kcal/g-atom};$$
$$\Delta\bar{H}_U = -33.2 \pm 0.7 \text{ kcal/g-atom};$$
$$\Delta\bar{S}_U^{ex} = -16.8 \pm 0.7 \text{ eu/g-atom}.$$

While the activity of uranium in solutions obeys the Henry law, the activity of aluminum obeys the Raoult law. Changes in the integral excess characteristics (Table 2) can be found from the equation $\Delta G^{ex} = x_U \cdot \bar{G}_U^{ex}$.

The dissolution of uranium in liquid aluminum is accompanied by a significant exothermic effect. For example, formation of 1 g-atom of a solution containing 1 at.% of uranium is accompanied with a release of 332 cal of heat, sufficient to raise the temperature of the reaction mixture in the calorimeter from 1000 to 1047°K (according to [7] the atomic heat of liquid aluminum is 7.0 cal/g-atom·deg).

The emf between uranium and its aluminum alloys was also measured for different two-phase domains of the uranium–aluminum phase diagram [8]. The experimental data were recalculated for γ uranium and are shown in Fig. 2. Alloys containing 25–40% by weight of uranium (see Fig. 2) exhibit several straight sections with discontinuities at 730 and 640°C that can be related to changes in the phase composition of the samples. The data of [2] are in good agreement with the results for solid-phase composition domains. Table 3 lists the coefficients of the equations representing the temperature dependence of emf, obtained by applying the method of least squares to our data and to the data of [2], as well as the partial thermodynamic characteristics of uranium in alloy calculated with these coefficients [4].

According to our data, the endothermic effect of the $UAl_4 \rightarrow UAl_3 + UAl$ reaction amounts to 2.9 ± 1.6 kcal/mole which is in good agreement with the figure of 4.0 ± 0.4 kcal/mole found from calorimetric measurements [2]. Obviously, the partial thermodynamic characteristics of uranium in alloys depend not only on the phase composition of the alloys but also on the state of aggregation of the phases. For example, the formation of the UAl_4 compound from γ uranium and liquid aluminum is accompanied by a loss of partial enthalpy of 41.5 ± 0.8 kcal/g-atom and entropy of 17.8 ± 0.8 eu/g-atom. Taking into account the change of the corresponding functions in the hardening of 4 g of aluminum atoms ($\Delta H = -10.0$ kcal, $\Delta S = -10.72$ eu [7]), we get -31.5 ± 0.8 kcal/g-atom and -7.1 ± 0.8 eu/g-atom which corresponds to the change in thermodynamic functions of uranium in the course of formation of the UAl_4 compound from γ uranium and solid aluminum and agree well with the experimental values of $\Delta\bar{H}_U$ and $\Delta\bar{S}_U$ in this phase domain (-29.1 ± 2.3 kcal/g-atom and -4.1 ± 2.8 eu/g-atom). Thermodynamic characteristics obtained by measuring the emf between uranium and its liquid two-phase alloys show better reproducibility and are apparently more trustworthy. As a result, these characteristics were used to calculate the thermodynamic characteristics of the formation of uranium–aluminum compounds of γ uranium and solid aluminum. From these values we deducted the changes in thermodynamic function due to transformation of γ uranium into α uranium ($\Delta H = -1.8$ kcal/g-atom, $\Delta S = -2.8$ eu/g-atom [5]) and to aluminum hardening ($\Delta H = -2.5$ kcal/g-atom, $\Delta S = -2.68$ eu/g-atom

[7]) and thus obtained partial characteristics for α uranium in compounds. Integral characteristics and aluminum activities were calculated from the Gibbs–Duhem equations. The calculated results are listed in Table 4.

The formation of uranium–aluminum compounds is accompanied by release of heat, and a reduction of entropy and free energy. The maximum value of ΔH (–7.92 kcal/g-atom) corresponds to the most stable compound in the system, UAl_2, which has the highest melting point (1590°C [8]). Maximum loss of entropy (–1.06 eu/g-atom) occurs in UAl_3 which agrees with the inference about the high degree of order in this compound [9]. The heats of formation of UAl_4 and UAl_2 compounds of α uranium and solid aluminum at 900°K (–29.7 ± 0.8 and –23.8 ± 1.3 kcal/mole) are practically the same as the data cited in [1, 2] at 298°K. This indicates that these values are constant over a wide temperature interval and are quite reliable. The discrepancy in ΔH for UAl_3 lies outside experimental errors and is probably due to the temperature dependence of the heat effect in the formation of this compound.

The data of Table 3 were used to establish the temperature dependence of uranium activity (with reference to γ uranium) in uranium-saturated liquid solutions of aluminum:

$$\ln a_U = -\frac{zF}{RT}E;$$

$$\lg a_U = 3.266 - \frac{8438}{T} \pm 0.03 \quad (730 - 870^\circ C); \tag{2}$$

$$\lg a_U = 3.902 - \frac{9074}{T} \pm 0.03 \quad (640 - 730^\circ C). \tag{3}$$

The difference of (2), (3), and (1) gives an expression for the temperature dependence of uranium solubility in molten aluminum:

$$\lg x_U = \lg a_U - \lg \gamma_U;$$

$$\lg x_U = -0.406 - \frac{1172}{T} \pm 0.08 \quad (730 - 870^\circ C); \tag{4}$$

$$\lg x_U = -0.230 - \frac{1808}{T} \pm 0.08 \quad (640 - 730^\circ C). \tag{5}$$

Calculations indicate that 13.7 and 19.5% by weight of uranium is dissolved in aluminum at 640 and 730°C respectively confirming the figures of 13.0 and 19.3% by weight cited in [8].

LITERATURE CITED

1. M. I. Ivanov et al., At. Énerg., 5, 166 (1958).
2. P. Chiotti and J. Kateley, J. Nucl. Materials, 32, 135 (1969).
3. V. A. Lebedev et al., Élektrokhimiya, 2, 160 (1966).
4. A. A. Vecher et al., Zh. Fiz. Khim., 35, 1578 (1961).
5. M. A. Filyand and E. I. Semenova, The Properties of Rare Elements [in Russian], Metallurgizdat, Moscow (1964), p. 662.
6. V. A. Lebedev et al., Zh. Fiz. Khim., 42, 690 (1968).
7. Ya. I. Gerasimov et al., Chemical Thermodynamics in the Nonferrous Metallurgy [in Russian], Vol. 4, Metallurgiya, Moscow (1966), p. 11.
8. M. Hansen and C. Anderko, Binary Alloy Structures [Russian translation], Vol. 1, Metallurgizdat, Moscow (1962), p. 160.
9. J. Maskrey and B. Frost, J. Inst. Metals, 81, 171 (1953).

PRODUCTION OF Ac^{227} AND Th^{228} ISOTOPES BY IRRADIATION OF RADIUM IN THE SM-2 REACTOR

Z. K. Karalova, R. N. Ivanov,
B. F. Myasoedov, L. M. Rodionova,
Z. I. Pyzhova, S. M. Kalebin,
and V. Ya. Gabeskiriya

UDC 621.039.554

Actinium-227 belongs to a group of isotopes that are used as radioactive fuel in thermoelectric generators of extended action [1]. According to reports the first Ac^{227}-based units with a thermal capacity of 250 W are already in operation [2].

Natural sources are not very promising for the production of significant amounts of Ac^{227} since the concentration of actinium in pitchblende does not exceed 0.15 mg per ton of uranium. In addition, such actinium samples usually contain rare earths whose separation is quite difficult. Actinium can also be extracted from Pa^{231} but this technique takes a very long time for Ac^{227} to accumulate

Ac^{227} was first synthesized from radium in 1945, and the first milligram quantities of this isotope were obtained somewhat later. The efficiency of artificial production of Ac^{227} can be considerably improved by irradiating radium in a reactor with a high-density neutron flux. This technique gives as side products significant quantities of Th^{228} and Th^{229} isotopes, the study of whose nuclear properties is of great theoretical importance and has considerable practical value in reactor design.

Irradiation of Ra^{226} by neutrons gives rise to the following main reactions:

$$\begin{array}{l} Ra^{226} \xrightarrow{n\gamma} Ra^{227} \\ \quad\quad\downarrow \beta- \\ Ac^{227} \xrightarrow{n\gamma} Ac^{228} \\ \quad\quad\quad\downarrow \beta- \\ Th^{228} \xrightarrow{n\gamma} Th^{229}. \end{array}$$

According to the most recent data, the thermal-neutron capture cross section of Ra^{226} at the thermal point is equal to 8.3 ± 0.9 b [3] (the resonance integral is 222 ± 15 b). The neutron capture cross section of Ac^{227} is higher and equal to approximately 814 b [4]. In the third reaction any significant yield of Th^{229} can be expected only with flux densities of the order 10^{15} neutrons/cm^2·sec.

After irradiation the Ra^{226} sample contains isotopes of the following three families: Ra^{226} ($T_{1/2}$ = 1620 years), Ac^{227} ($T_{1/2}$ = 21.9 years), and Th^{228} ($T_{1/2}$ = 1.9 years). The process of actinium separation must thus take into account the buildup and decay of daughter products, such as Rn^{222}, $Pb^{210-212}$, Po^{210}, Th^{227}, $Ra^{223,224}$, etc.

The previously known schemes of reprocessing irradiated radium were based on extraction and on cation exchange. Extraction with thenoyltrifluoroacetone (TTA) was most frequently used [5]. The main disadvantage of this method is that extraction of significant quantities of actinium requires a pH higher than 5.5. Under such conditions actinium is in a partially hydrolyzed state and this affects the yield as hydrolyzed forms of actinium are not extractable [6]. Moreover, the extraction of actinium is sometimes complicated by the formation of a residue resulting from the interaction of radium with radiation damage products

Translated from Atomnaya Énergiya, Vol. 32, No. 2, pp. 119-122, February, 1972. Original article submitted March 18, 1971.

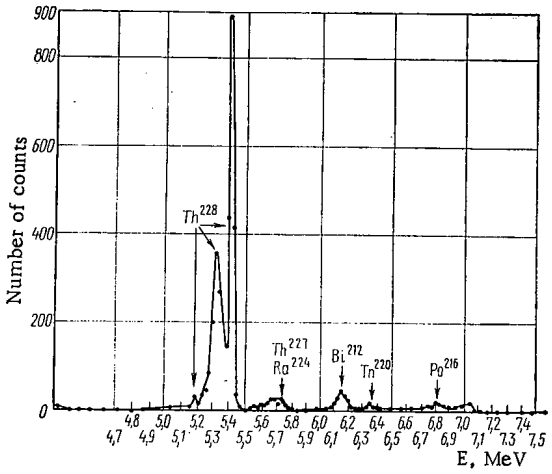

Fig. 1. Alpha spectrum of Th^{228}.

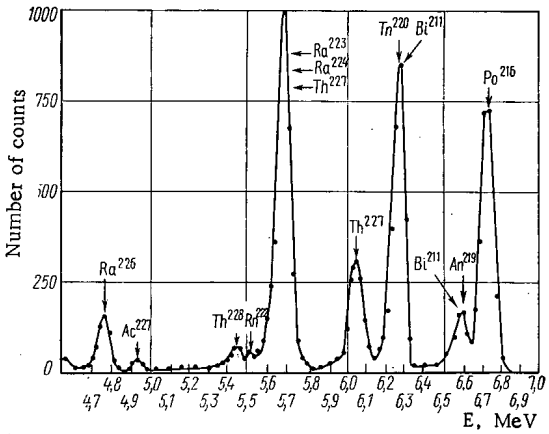

Fig. 2. Alpha spectrum of actinium fraction before purification.

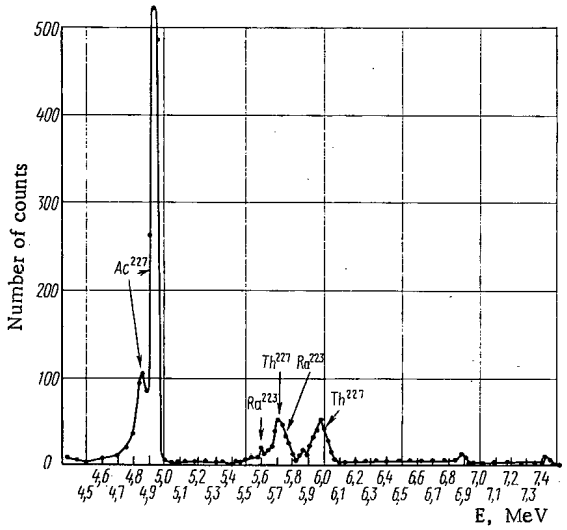

Fig. 3. Alpha spectrum of Ac^{227}.

of TTA [7]. Extraction with TTA does not secure complete separation of actinium from accompanying elements, so that final refinement is obtained by extraction chromatography [8] or by precipitation of impurities in the form of sulfides [6].

Along with extraction, irradiated radium was processed by the ion-exchange method [9]. Element separation takes place in a medium of mineral acids (HCl, HNO_3) and a cation-exchange resin [10]. However, ionizing radiation affects the stability of these resins causing disruption of their functional groups, and converting them into a soluble state with the formation of sulfuric acid. Thus, relatively insoluble $RaSO_4$ can form when the starting solution contains large quantities of radium resulting in a lower yield of Ac^{227} and Th^{228}.

In the present work we report on the processing of Ra^{226} after irradiation in the SM-2 reactor by a thermal-neutron flux of 10^{15} neutrons/$cm^2 \cdot sec$ with the purpose of determining the buildup of Ac^{227} and Th^{228} isotopes.

After removing the main body of radium by dissolving the sample in HNO_3, the Th^{228} and Ac^{227} isotopes were separated with the aid of the AB-23M radiation-resistant anion-exchange resin containing pyridine groups and by extraction with 1-phenyl-3-methyl-4-benzoylpyrazolone-5 (PMBP). The extraction of actinium and thorium with PMBP has been described before [11, 12]. PMBP has several advantages over TTA: it allows actinium to be extracted in quantity from a medium with higher acidity, equilibrium is established much faster, and full separation from accompanying elements is possible.

For irradiation we have used a 15.44 mg sample of radium in the form of $RaCO_3$ roasted at 700°, and prepared by melting radium sulfate with alkali-metals carbonates. Radium carbonate contained 4.75% barium and traces of other elements.

The radium sample was placed in a dismountable, hermetically sealed platinum ampoule and exposed to an integral neutron flux of $(9.8 \pm 0.2) \cdot 10^{21}$ neutrons/cm^2. Six and a half months after exposure the ampoule was opened and the sample dissolved. At the instant of solution the sample activity was 800 mg-eq Ra. Opening and solution of the sample, and separation of the main radium mass took place in a hot cell reequipped for operation with emanating substances. The cell had a plastic box connected by means of a system of valves with a freeze trap (activated carbon, liquid nitrogen) and with a vessel under low pressure for collecting the major portion of radon. The top of the ampoule was "cut" off by means of a special machine

tool. The ampoule content was poured into a platinum cup, and the inside of the ampoule was washed with an acid which was added to the main substances. After removing the sample the ampoule gamma activity was ~10% of the initial activity.

The sample was dissolved by heating in HNO_3. The radium nitrate residue precipitated by adding concentrated nitric acid was filtered and the 8N HNO_3 solution (v = 15-20 ml) was passed at a rate of 0.5 ml /min through a 10-cm high, 0.8-cm diameter chromatographic column packed with AB-23M anion-exchange resin in a NO_3^- form (0.25-0.5 mm grains, 3 g of air-dry resin). The filtrate and wash water were evaporated to dryness, the residue was dissolved in 8N HNO_3, and once again passed through the anion-exchange cycle. Thorium was desorbed from the resin with 50 ml of 0.1N HNO_3.

To separate actinium from the filtrate obtained after passing the starting solution through resin, we have used extraction with a solution of PMBP in a mixture of benzene and acetyl alcohol. For this purpose batches of the solution were evaporated to dryness, the residue was twice treated by heating with concentrated HNO_3, and dissolved in 5 ml of 1M NH_4NO_3 with a pH of 2.6. The solution was transferred into a separatory funnel and, after adding 5 ml of 0.25 M PMBP in a mixture of benzene and octyl alcohol, the extraction was continued for 5 min. The extract was washed in 5 ml of 3M NH_4Cl and reextracted Ac^{227} with 5 ml 1N HNO_3. The reextract was washed in benzene.

Quantitative determination of Ac^{227} and Th^{228} was made using an alpha counter with 2π geometry, the fraction of alpha activity of each isotope being measured with an alpha spectrometer. In some cases actinium was quantitatively determined with an alpha spectrometer using Th^{230} (Io) 0.59 μg of which in a radiochemically pure form was deposited on the target with the analyzed sample. The alpha spectrometer used in this work had a silicon surface-barrier detector with a resolving power of about 0.8%. The instrument was calibrated against Cm^{244}, Cm^{242}, Am^{243}, and Am^{244} isotopes. The average energy per channel was 21-23 keV. The amount of Th^{228} on the targets fluctuated between $4.2 \cdot 10^{-7}$ and $8 \cdot 10^{-6}$ μg and of Ac^{227} from $5 \cdot 10^{-3}$ and $1 \cdot 10^{-2}$ μg.

The suggested scheme of reprocessing irradiated radium allowed the major portion of the sample (more than 70%) to be separated out in the course of solution as a result of the salting-out action of HNO_3. Besides radium, the precipitate contained barium and some lead isotopes. Coprecipitation of actinium and thorium under such conditions did not exceed 1%. In passing of the initial solution through the AB-23M anion-exchange resin in 8M HNO_3, thorium in the form of a nitrate group was quantitatively sorbed on the resin and separated from actinium, lead, bismuth, and radium which passed into the filtrate. Separation from polonium was achieved by desorption of thorium in a 0.1N HNO_3 solution.

Figure 1 shows the alpha spectrum of the thorium fraction measured 3.5 h after separation. Peaks belonging to Th^{228} and its daughter products (Ra^{224}, Bi^{212}, Tn^{220}, Po^{216}) were detected. Analysis of the thorium fraction proved that the content of Th^{228} is 0.576 ± 0.116 mg with 2% of Ac^{227}.

After thorium separation the major portion of actinium together with isotopes of bismuth, lead, and radium, and traces of thorium (less than 0.1%) remained in the filtrate. In the course of extraction of actinium in the form of a chelate compound with PMBP, the mixture of benzene and octyl alcohol with pH = 2.6 participated separation of radium which remained in an aqueous phase. Lead was separated out from actinium by washing the extract with 3M NH_4Cl, while thorium and bismuth were isolated by reextraction with 1N HNO_3. The content of actinium in the final solution was noted to diminish as the number of extractions was increased with the purpose of improving the radiochemical purity of actinium. It was found that some of the loss occurs at the extraction stage since about 5% of the starting amount of actinium remains in the aqueous phase. The loss of actinium can be avoided by repeating the extraction.

Figure 2 shows the alpha spectrum of the actinium fraction before purification, i.e., directly after separating Th^{228} in the anion-exchange resin. Besides Ac^{227} and its daughter products (Th^{227}, Ra^{223}, Bi^{211}, An^{219}) the spectrum shows the presence of Ra^{226} and Th^{228} and of their decay products.

Fourfold extraction with PMBP allows the actinium to be obtained in an almost pure radiochemical form (Fig. 3). The presence of daughter products (Th^{227}, Ra^{223}) in the alpha spectrum of Ac^{227} is due to their fast accumulation while the sample was being prepared for measurement. However, the by weight amount of Th^{227} and Ra^{223} impurities in Ac^{227} is negligible. In the presence of daughter products, it is better to determine actinium with an alpha spectrometer calibrated with Th^{230}.

The investigations proved that the content of Ac^{227} in the starting solution was 0.303 ± 0.05 mg, and the chemical operations had an Ac^{227} yield of 91%. As indicated before, the starting solution contained 0.576 ± 0.116 mg Th^{228}. Taking into account Th^{228} decay, the content of the thorium-228 isotope in the sample at the instant it left the reactor was found to be 0.730 ± 0.147 mg.

Thus, the experimental data indicate that the accumulation of Ac^{227} and Th^{228} after exposure to an integral flux of $(9.8 \pm 0.2) \cdot 10^{21}$ neutrons/cm^2 amounts to 2.15 and 4.72% of the starting quantity of radium.

LITERATURE CITED

1. G. M. Fradkin and V. M. Kodyukov, At. Énerg., 26, 169 (1969).
2. G. Gammel, M. Koskinen, and A. Trover, Raumfahrtforschung, 13, 1 (1969).
3. S. M. Kalebin et al., Yadernaya Fiz., 14, 22 (1971).
4. H. Kirby, G. Grove, and D. Timma, Phys. Rev., 102, 1140 (1956).
5. F. Hagemann, J. Amer. Chem. Soc., 72, 768 (1950).
6. H. Kirby, Progress in Nuclear Energy. Analytical Chemistry, Vol. 8, Part 1, New York (1967), p. 89.
7. P. Engle, Report MLM-454 (1950).
8. C. Ruiz, B. Reider, and J. Gehart, USA Patent, No. 3 (1966), pp. 459, 634.
9. F. Hagemann and H. Andrews, Report ANL-4215 (1948).
10. M. Cabell, Canad. J. Chem., 37, 1094 (1959).
11. Z. K. Karalova, Z. I. Pyzhova, and L. M. Rodionova, Zh. Analiticheskoi Khim., 25, 909 (1970).
12. Z. K. Karalova and Z. I. Pyzhova, Zh. Analiticheskoi Khim., 23, 1564 (1968).

INTERACTION OF HIGH-ENERGY RADIATION WITH MATTER

V. S. Barashenkov, N. M. Sobolevskii, and V. D. Toneev

UDC 539.12.17

The reliable calculation of the interaction of beams of high-energy particles with blocks of materials of various compositions, shapes and sizes is becoming more and more important in connection with a wide variety of practical problems, such as the effective radiation screening of accelerators and space craft, the design of high-power neutron generators, the solution of a whole string of geophysical problems, and so on. A universal and very flexible technique for solving such problems is simulation of the interaction process by Monte-Carlo methods with the aid of a digital computer. A number of programs for effecting such calculations have been described in the literature [1-3]. The central and most complex point in all these programs is the calculation of the characteristics of particles produced in nonelastic pion–nucleus and nucleon–nucleus collisions. The quality of the program depends to a great extent on how accurately this part of the calculation is performed. Allowance is also made in the programs for ionization energy losses and for the possibility of the rapid decay process $\pi^\circ \to 2\gamma$ with the subsequent propagation of the products of the process within the material. The slower processes $\pi \to \mu + \nu$, $\mu \to e + \nu + \bar{\nu}$ are sometimes also taken into account. In some programs the effects of multiple Coulomb scattering are considered, and the behavior of low-energy neutrons simulated. Ranft's program [1] is directed towards the calculation of the interaction of very high energy particles ($T \approx 10\text{-}10^3$ GeV†) with large blocks of material.

A shortcoming of program [1] is the very coarse approximation of particle–nucleus collisions.

The method described in [2] is suitable only for comparatively small energies ($T < 600\text{-}700$ MeV), where meson formation can still be neglected. The characteristics of particle–nucleus collisions, previously calculated through an independent program, are stored in the memory of the computer in the form of a set of approximate distributions. A deficiency of program [2] is the loss of correlation between the exit angle and the energy of particles produced in nonelastic nucleon–nucleus collisions. As a result, the program yields only average, integral quantities: fluxes of particles, their combined spectra, and so on.

The NMTC program [3] has good possibilities. It permits simulation of the propagation in matter of nucleons with energies $T < 3.5$ GeV (including low-energy neutron components) and of fluxes of π and μ mesons with energies $T < 2.5$ GeV. Nonelastic particle–nucleus collisions are taken into account through the cascade-evaporation model of nuclear reactions described by Bertini [4], which yields the characteristics of the secondary particles sufficiently well. Bertini's program is incorporated in the NMTC program as a separate subprogram, the calculation of pion–nucleus and of nucleon–nucleus interactions being carried out afresh in each case.

A program of similar structure was recently developed by us at the Joint Institute for Nuclear Research in Dubna. However, as our program utilizes an improved cascade-evaporation model [5, 6], it holds right up to very high energies, up to several tens of GeV. The cascade-evaporation model used by us gives rather well both the high-energy and low-energy characteristics of secondary particles, including the double differential distributions $\partial^2\sigma/\partial\mathcal{T}\partial\Omega$. In contrast to Bertini's model [4], where it is assumed that all π mesons are formed through the decay of pion–nucleon resonances N^*_{33} (1236), the calculation of pion

†Here and below we denote by T the kinetic energy of a primary particle, and by $\mathcal{T}$ the kinetic energy of a secondary particle in a laboratory system of coordinates.

Translated from Atomnaya Énergiya, Vol. 32, No. 2, pp. 123-129, February, 1972. Original article submitted April 8, 1971.

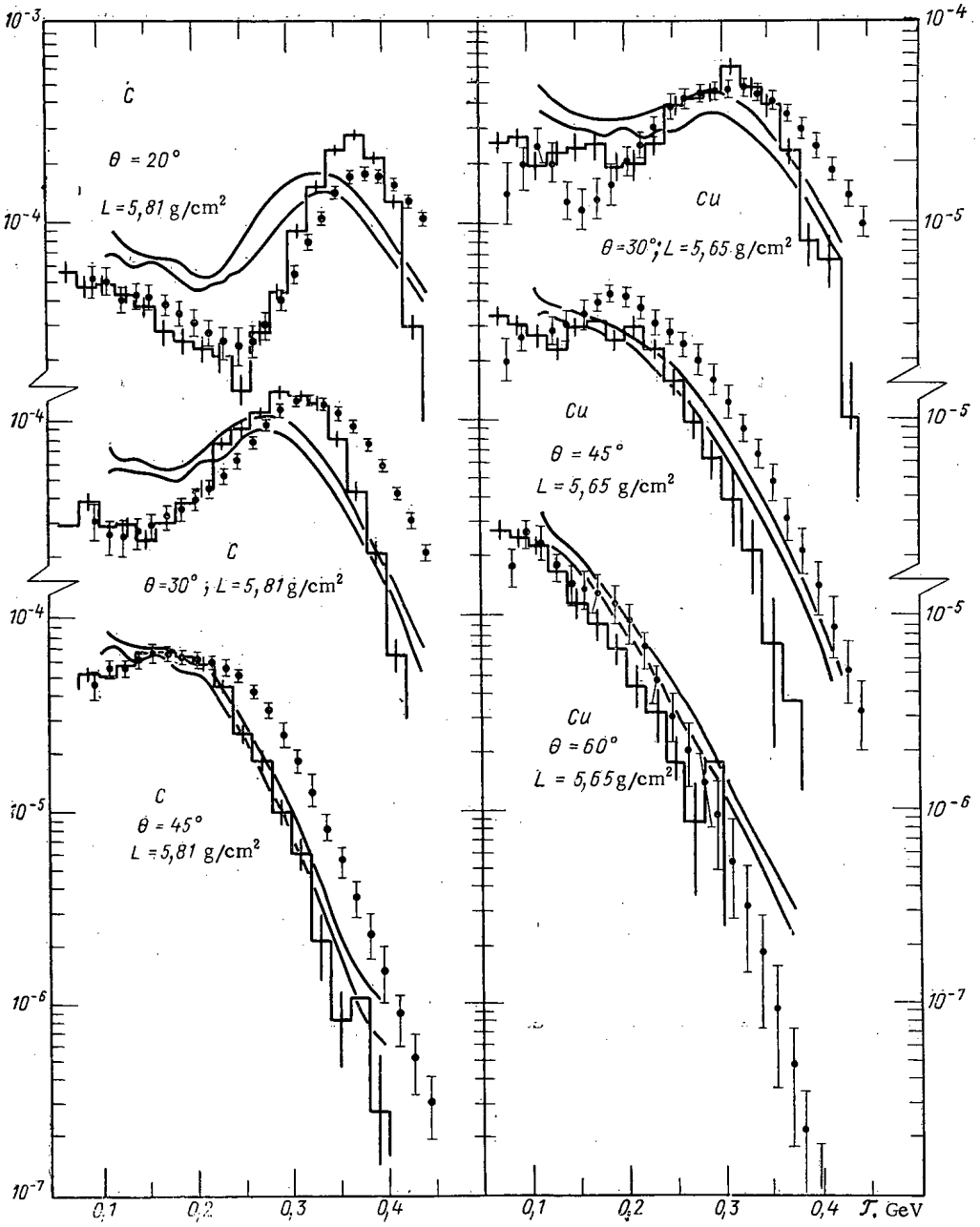

Fig. 1. Energy spectrum of protons emitted at an angle θ from slabs of carbon and copper of thickness L for 450 MeV incident proton beam. Units: protons $\cdot$ MeV^{-1} $\cdot$ ster^{-1} $\cdot$ primary protons^{-1}. Histograms – our calculation for angular intervals $\theta \pm 5°$; points – corresponding calculation of Alsmiller et al., [9] for the same angular intervals. The solid curves show the corridors delimiting the experimental data [10].

formation in our case is based on a statistical approximation of known experimental data. This improves the accuracy of the calculation and extends its range of applicability to very high energies, up to T $\approx$ 30 GeV.

It should be mentioned, however, that if the varying density of the intranuclear matter during the development of a cascade within the nucleus is neglected [6] when calculating the nonelastic pion–nucleus and nucleon–nucleus interaction, then the multiplicity of low-energy particles in the material is increased appreciably at primary particle energies T > 3-5 GeV. In this case, correct results are obtained only for particles with energies $\mathcal{T}$ > 100 MeV.

Ionization losses were taken into account through the well-known formula of Sternheimer [7]. The propagation of neutrons with energies ~1 eV < $\mathcal{T}$ < 10 MeV was simulated using the multigroup system of constants for reactor calculations [8].

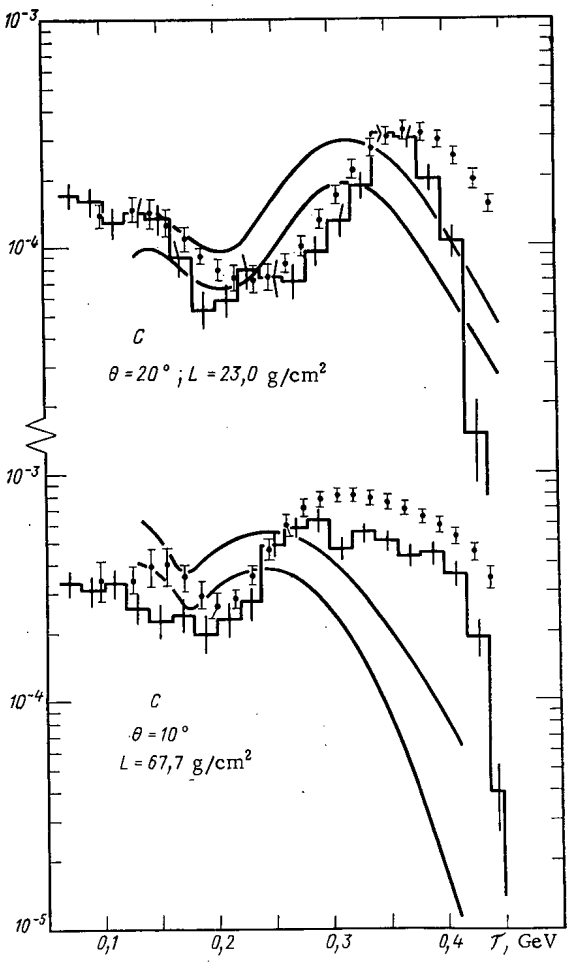

Fig. 2. Energy spectra of neutrons emitted from carbon slabs for 450 MeV incident proton beam. Units: neutrons · MeV^{-1} · $ster^{-1}$ · primary $protons^{-1}$. Notation as in Fig. 1.

To check the reliability of the program and to get an idea of possible systematic errors in the method, we compared our results with existing experimental data and with the calculations of other authors. Figures 1-3 show the spectra of protons and neutrons emitted at specific angles from slabs of different materials for a narrow monoenergetic incident beam of 450 MeV protons. The transverse dimensions of the slabs were sufficiently large. It can be seen from the figures that there is excellent agreement between calculation and experiment at angles $\theta > 30°$ for the most diverse targets in composition and thickness. Discrepancies in the hard part of the spectra appear at small angles, particularly in the case of thin targets. These discrepancies are due to errors in the cascade model, which gives the quasielastic scattering peak with insufficient accuracy. The discrepancies are smoothed out to some extent in targets of thickness more than one mean nuclear path (see Figs. 2, 3). This comes about because in such targets the particle experiences on the average more than one nonelastic scattering event, which "erodes" to some extent the too sharp calculated peak. Similar results are also obtained with the NMTC program. Although there is a discrepancy between the shapes of the calculated and experimental spectra at small angles, the total output of secondary nucleons from the shield is computed correctly.

Figures 4, 5 show the calculated and experimental cross sections for the production of the isotopes F^{18} and Na^{24} in aluminum foils. The foils, perpendicular to the direction of the primary proton beam, are located at various depths within an iron block of dimensions 30.5 × 30.5 × 95 cm. In Shen's experiment [11] this block was irradiated by a narrow beam of protons with energies 1 and 3 GeV; the beam was incident perpendicular to the end face of the block. The experimental situation was exactly modelled in our calculations. To permit comparison of our results with the results obtained with the NMTC program [12], we used the same definition of macroscopic cross section and the same excitation functions as in [12].

A comparison of our calculations with the theoretical data of [12] shows that the contribution to the cross section from interactions with charged particles is smaller, and the contribution from neutrons with energies $\mathcal{T} < 25$ MeV – greater. Nevertheless, the manner in which the cross section varies with radius is given quite well both by our calculation and by calculation through the NMTC program. The same can be said for the manner in which the cross section varies with the depth z in the block (see Fig. 4), although in this case there is difference in absolute magnitude between the calculated and experimental cross sections (by not more than a factor of 2-2.5 in the worst case).

In the experiments of Citron et al. [13] a beam of protons of momentum 19.2 GeV/c also fell normally on the end face of an iron block, of dimensions 100 × 160 × 300 cm. The beam, of diameter 2 cm, had a "halo" of protons, neutrons, and π mesons. The diameter of this "halo" was comparable with the transverse dimensions of the iron block. Plates of photoemulsion were situated in the block at various depths perpendicular to the axis of the beam. In the scanning of the plates only those stars were recorded which were formed by particles with energies $\mathcal{T} > 100$ MeV. These stars were divided into three types: P stars, which have a fine track in an angle ±5° to the beam axis; P_B stars, which have a fine track in the backward hemisphere but outside ±5° to the beam axis; and N stars, which have no fine track in the backward hemisphere.

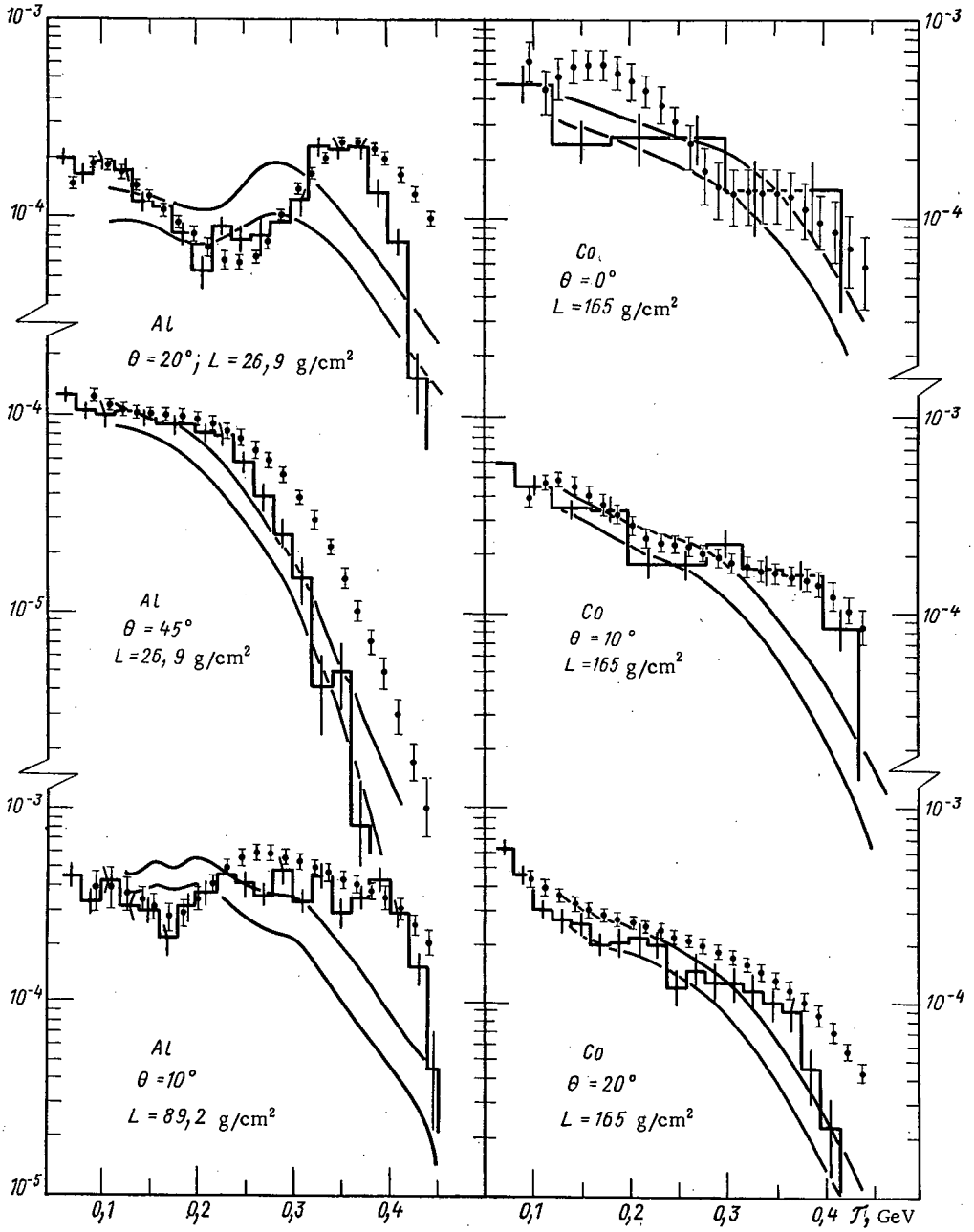

Fig. 3. Energy spectra of neutrons emitted from aluminum and cobalt slabs for 450 MeV incident proton beam. Units: neutrons · MeV^{-1} · $ster^{-1}$ · primary $protons^{-1}$. Notation as in Fig. 1.

Except for some insignificant assumptions (the beam was assumed narrow, the block was regarded as a cylinder of length 300 cm with a base area equal to the area of the real target), all the conditions of the experiment were modelled in the calculation. In particular, the identifications of the stars corresponded exactly to experiment.

Figures 6, 7 show that at energies much in excess of the region of applicability of the NMTC program the present method gives excellent quantitative agreement with experiment. It should be emphasized that it is very important to reproduce the experimental situation sufficiently accurately when fitting the theoretical and experimental data. In particular, the corridor of theoretical values shown hatched in Fig. 6 represents the indeterminacy associated with the fact that the area and shape of that region of the photoemulsion which was scanned in [13] was unknown to us.

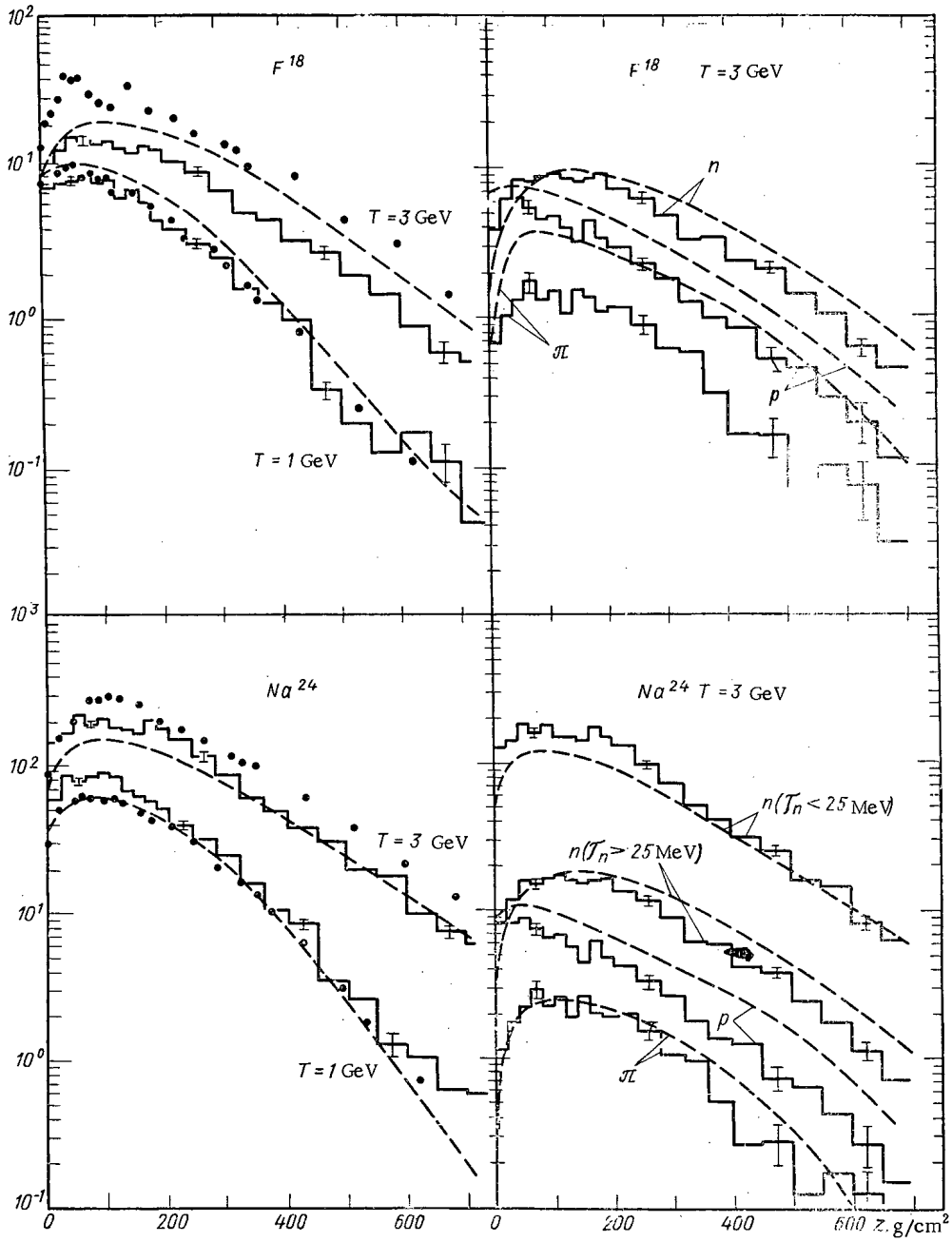

Fig. 4. Total cross sections for formation of isotopes F^{18} and Na^{24} in aluminum foil as a function of distance z of foil from end face of iron block. Incident proton energies 1 and 3 GeV. Units: mbarn/primary proton. The contributions to the cross sections coming from the interactions of neutrons, protons and π mesons are shown on the right (T = 3 GeV); the contributions from neutrons with energies below and above 25 MeV are shown separately for the Na^{24} isotope. Histograms – our calculation; dashed curves – calculation of [12]; the points – experimental data from [11].

In this manner, the cascade-evaporation model of nonelastic particle–nucleus collisions [5, 6] permits calculation of the interaction of beams of particles with matter over a very wide range of energies, right up to several tens of GeV. Refinement of the cascade-evaporation model by incorporation of

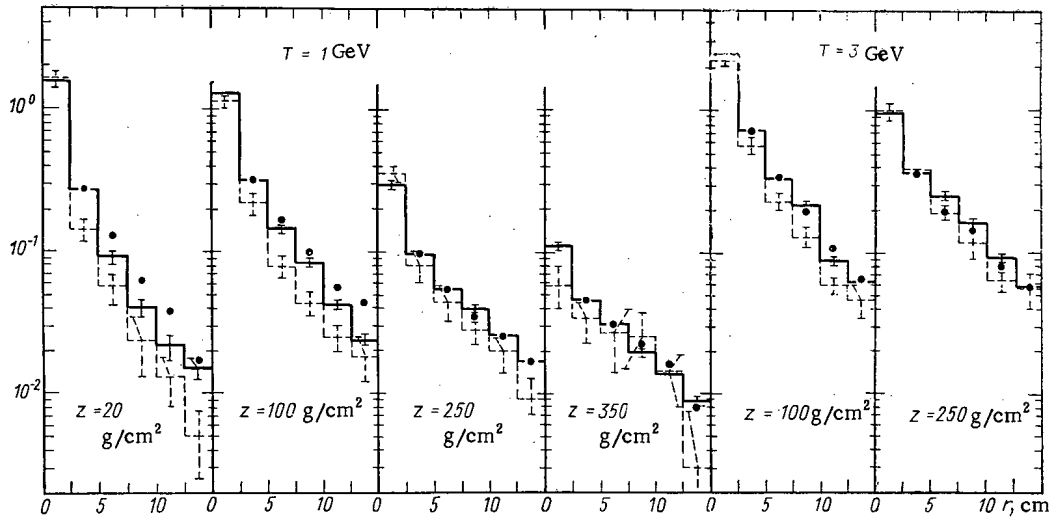

Fig. 5. Radial dependence of cross section for formation of Na^{24} isotope in aluminum foil for various values of depth z in iron block. Units: mbarn/cm^2 · primary proton. Incident proton energies 1 and 3 GeV. r – distance to beam axis. Solid histograms – our calculation; dashed histograms – calculation of [12]; the experimental points [11] are normalized to our theoretical values in the second annular zone (only the relative cross sections are quoted in [11]).

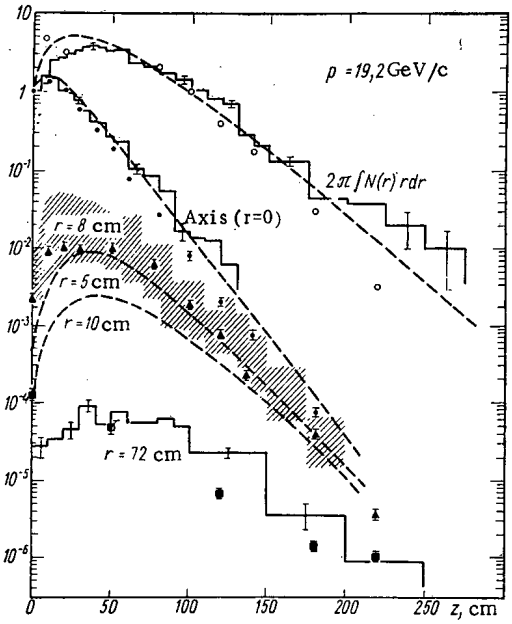

Fig. 6

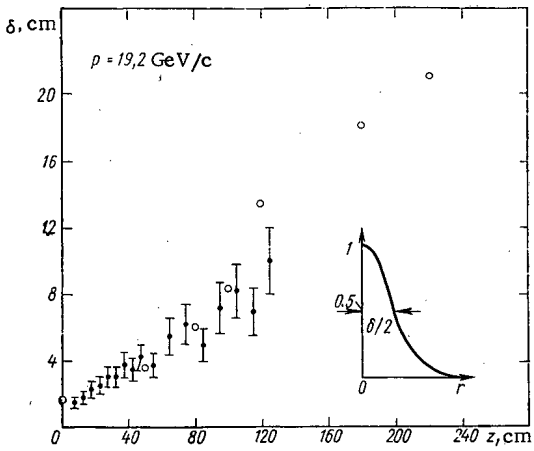

Fig. 7

Fig. 6. Star distribution with depth z in iron block. Momentum of incident protons 19.2 GeV/c. Histograms – our calculation; solid curves – Ranft's calculation [1]; experimental points are taken from [13]. The star densities at r = 0.8 and 72 cm are normalized to the star density at r = 0, z = 0. The hatched region corresponds to indeterminacy in scanning (see text).

Fig. 7. Total width δ of radial star density distribution as function of depth z in iron block. Points – our calculation, circles – experimental data taken from [13].

multiparticle intranuclear interactions [14] should permit calculation of the interaction of radiation with matter at still higher energies.

LITERATURE CITED

1. J. Ranft, CERN 64-67, Geneva, 1964; Nucl. Instrum. Methods, 48, 133, 261 (1967).
2. V. E. Dudkin et al., in: Radiation Dosimetry and the Physics of Shielding Charged-Particle Accelerators [in Russian], OIYaI (Joint Institute for Nuclear Research) 16-4888, Dubna (1970), p. 75.
3. W. Coleman, ORNL-TM-2206, Oak Ridge (1968); W. Coleman and R. Alsmiller, Nucl. Sci. Engng. 34, 104 (1968); W. Coleman and T. Armstrong, ORNL-4606, Oak Ridge (1970).
4. H. Bertini, ORNL-3383, Oak Ridge (1963); Phys. Rev., 188, 1711 (1969).
5. V. S. Barashenkov, K. K. Gudima, and V. D. Toneev, JINR Dubna Communications [in Russian], P2-4065 (1968), P2-4066 (1968); P2-4302 (1969), P2-4313 (1969), P2-4402 (1969); Acta Phys. Polon., 36, 457, 887 (1969); V. S. Barashenkov et al., JINR Dubna Communications [in Russian], P2-5507 (1970), P2-5549 (1970).
6. V. S. Barashenkov, A. S. Il'inov, and V. D. Toneev, JINR Dubna Communications [in Russian], E2-5280 (1970), P2-5282 (1970).
7. R. Sternheimer, Phys. Rev., 118, 1045 (1960); S. V. Starodubtsev and A. M. Romanov, Passage of Charged Particles through Matter [in Russian], Izd. AN UzSSR, Tashkent (1962).
8. L. P. Abagyan et al., Group Constants for Nuclear Reactor Design [in Russian], Izd. Atomizdat, Moscow (1964).
9. R. Alsmiller et al., Nucl. Sci. Engng., 36, 291 (1969).
10. J. Wachter et al., ORNL-TM-1781, Oak Ridge (1968).
11. S. Shen, BNL-8721 (1964).
12. Y. Armstrong and R. Alsmiller, Nucl. Sci. Engng., 33, 291 (1968).
13. A. Citron et al., Nucl. Instrum. Methods, 32, 48 (1965).
14. I. Z. Artykov, V. S. Barashenkov, and S. M. Eliseev, Nucl. Phys., B6, 11, 628 (1968).

PLASMA ACCUMULATION THROUGH IONIZATION OF RESIDUAL GAS IN AN ELECTROMAGNETIC TRAP

Yu. I. Pankrat'ev, M. G. Nozrachev,
O. A. Lavrent'ev, B. G. Safronov,
V. A. Naboka, and E. F. Ponomarenko

UDC 533.9

Experiments on plasma containment in traps with oppositely directed magnetic fields have shown that there is a rapid loss of plasma through magnetic gaps [1-5]. A new approach to the problem of plasma containment is discussed in [6-10], where it is proposed to contain a plasma having an uncompensated space charge (Fig. 1).

It is well known that an electron cloud constitutes a trap for positive ions. A magnetic field which increases towards the periphery, for example – the field produced by oppositely directed currents, can be used to contain the electron cloud and assure hydrodynamic stability of the plasma. The loss of electrons through magnetic gaps is prevented by electrodes at negative potentials; the loss of ions is prevented by the electric field of the space charge of the electrons. Provided there are no "potential gaps" at the walls of the potential well produced by the electrons, ions produced by ionization of neutral gas within this well cannot escape from it as their energy is less than its depth. Such potential gaps can appear if the space charge of electrons oscillating in the magnetic gaps is large. The potential in the gap "sags," and ions can escape from the trap towards the negatively charged electrodes producing the retarding electrostatic fields for the electrons. This imposes a limit on the maximum density which can be contained in the trap. In the ring magnetic gap of cusp geometries ion containment ceases for an electron density in the gap given by [9, 10]

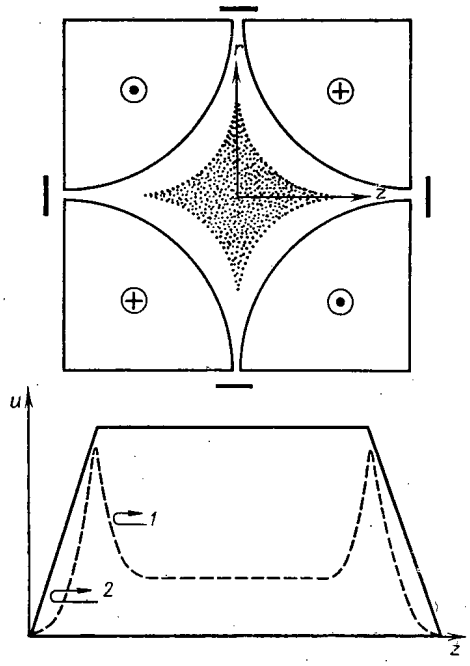

Fig. 1. Potential distribution (reckoned from cathode potential) required for the electromagnetic containment of plasma in the trap. The solid lines denote the vacuum potential distribution; the dashed curve denotes the potential distribution with plasma in the trap; 1) ions; 2) electrons; the radial (r) potential distribution is the same as the axial (z).

Translated from Atomnaya Énergiya, Vol. 32, No. 2, pp. 131-136, February, 1972. Original article submitted December 21, 1970; revision submitted March 22, 1971.

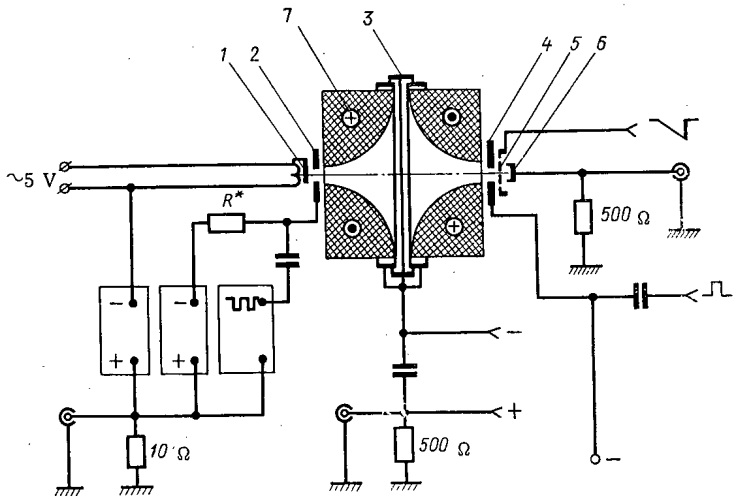

Fig. 2. Experimental arrangement. 1) Electron gun; 2) modulator; 3) blocking electrode in ring gap; 4) electrostatic shutter; 5) grid for analyzing electron energy spectrum; 6) Faraday cylinder; 7) magnet coils.

$$n=\frac{U_W}{2\pi e d_1(d_2-d_1/3)}, \tag{1}$$

where U_W is the potential of the well relative to the walls of the magnetic gap; $2d_2$ is the width of the magnetic gap; $2d_1$ is the width of the electron sheet, and $d_2 > d_1$.

The corresponding expression for the axial magnetic gaps has the form

$$n=\frac{U_W}{\pi e r_1^2\left(5/9+\frac{2}{3}\log\frac{r_2}{r_1}\right)}, \tag{2}$$

where r_2 is the radius of the axial gap; and r_1 is the radius of the region occupied by the electrodes. In a high β plasma, i.e., a sharp boundary between the plasma and the magnetic field, d_1 equals the Larmor radius of the ions ρ_i if there are no electric fields in the boundary layer [1].

If there is a large electric field in the boundary layer, the quantity d_1 can be put equal to $2\rho_e$ and $r_1 \sim 10\ d_1$.

The plasma density in the trap must increase as the size of the magnetic gaps is decreased and as the magnetic field in the gaps is increased. Injection must ensure that a high β plasma is produced within the trap. Increasing the energy of the electrons in the trap produces a deeper potential well, permitting containment of a plasma with a higher temperature. The lifetime of the plasma, which is determined by the lifetime of the electrons, must increase as the pressure of the residual gas in the trap is decreased. The purpose of the work reported in the present article was to investigate the influence of these conditions on the accumulation of hot plasma in the trap.

EXPERIMENTAL ARRANGEMENT

The magnetic field of the trap (Fig. 2) is produced by two liquid-nitrogen-cooled coils connected in opposition. The geometrical volume of the trap is 500 cm^3. The maximum field in the axial gaps is 5.5 kOe. The diameter of the axial gaps is 18 mm and the width of the ring gap is 4 mm. Blocking electrodes at a negative potential relative to the walls of the chamber are situated beyond the magnetic gaps outside the trap.

A diffusion pump with two nitrogen traps evacuates the apparatus to 10^{-6}-10^{-7} mm Hg, after which an ion sorption pump reduces the pressure to 10^{-8} mm Hg. The chamber containing the magnetic trap and the casing of the ion sorption pump were made from stainless steel. Metal vacuum seals were used throughout. The system was provided with water cooling and with a device for heating at 400°C.

Electrons are injected by an electron gun 1, which gives a current of 100 mA at electron energies 1-3 keV. To permit optimization of the injection conditions the gun could be moved relative to the input aperture

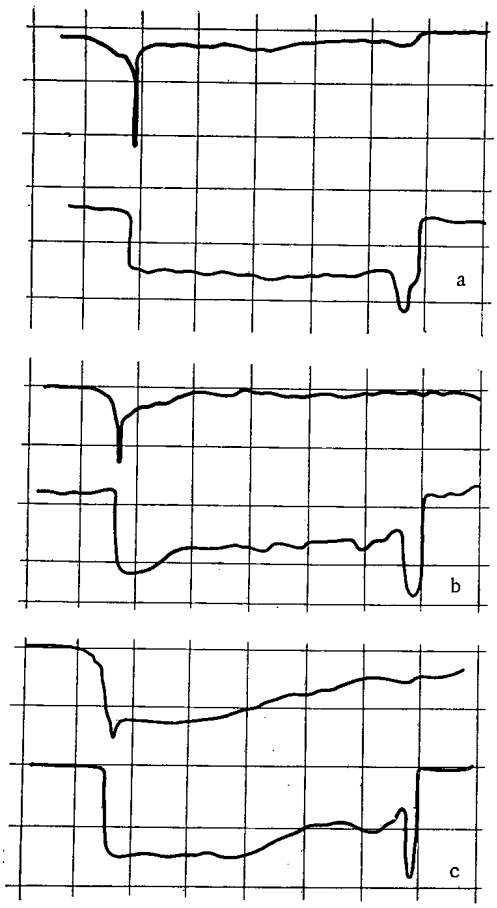

Fig. 3. Oscillograms of injection current (upper trace of each pair) and ion current to ring electrode (lower trace of each pair) for various pressures. a) 10^{-6} mm Hg, b) 5.10^{-7} mm Hg; c) 2.10^{-7} mm Hg. H = 2000 Oe, E = 400 eV, time scale 200 μsec/div.

of the trap. A diaphragm for modulation of the input electron beam is situated between the cathode of the gun and the input aperture. The cathode of the gun is negative relative to the walls of the chamber. Modulating electrode 2 is connected to a dc bias supply and, through a capacitor, to a square-wave generator, by means of which the electron beam can be switched on and off. The duration of the injection pulses could be varied from 10 μsec to 20 msec.

An arrangement for analyzing electrons in energy is situated at the other end of the trap. This arrangement includes a diaphragm 4, serving as an electrostatic shutter, a grid 5 supplied with a retarding potential, and a Faraday cylinder 6.

Plasma was produced in the trap by ionizing the residual gas. Optimum conditions were obtained utilizing the data in [7-11]. If, during the time it is in the trap, an electron loses some of its kinetic energy, it will be unable to return to the cathode of the electron gun. In the initial stages of the accumulation of plasma in the trap, the only way an electron can lose energy is through ionization and excitation of the neutral gas in the trap. As plasma accumulates, however, it will play an increasing role in the capture of electrons.

If the loss of electrons is small, a negative space charge can build up in the trap. The potential well of this space charge has a depth of the order of the energy of the injected electrons. A certain time after the start of injection, the injection current from the electron gun must begin to fall. The ultimate injection current will characterize the loss of electrons in the trap.

The number of particles accumulated in the trap was determined during the decay of the plasma after termination of the injection pulse. The number of ions was found from the ion current I_i to the negative electrode in the ring gap $N_i \approx 6.10^8 \int I_i dt$; the number of captured electrons was determined from the electron current to the Faraday cylinder in the axial gap. To extract electrons from the trap, a positive square pulse was applied to the diaphragm of the electrostatic shutter. The electron energy distribution was measured by the method of retarding potentials. By varying the delay between the end of the injection pulse and the moment the shutter is opened by the positive pulse, it was possible to determine the lifetime of electrons in the trap and the temporal variation of their energy spectrum. Unfortunately, the narrowness of the magnetic gaps of the trap, a necessity if dense plasmas are to be contained, precluded the use of high-frequency and probe diagnostic techniques.

RESULTS

The rate at which space charge accumulates in the trap is proportional to the injection current from the electron gun. Consequently, the transient processes occurring during the initial stage of plasma accumulation were observed at low-power injections: injection current ~5 mA, beam energy 1 keV. Oscillograms of the injection current of electrons and of the leakage of ion current to the negative electrode in the ring gap are shown in Fig. 3 for various residual gas pressures. The initial jump in the injection current is due to the formation of space charge, after which the injection current goes on replenishing electron losses. The ionization of the residual gas leads to an increase in the losses, as a result of which the injection current required to maintain equilibrium also increases. The ion leakage current also testifies to the accumulation of plasma in the trap. At low pressures the rate of ionization is lower (so that plasma accumulates more slowly) than at high pressures.

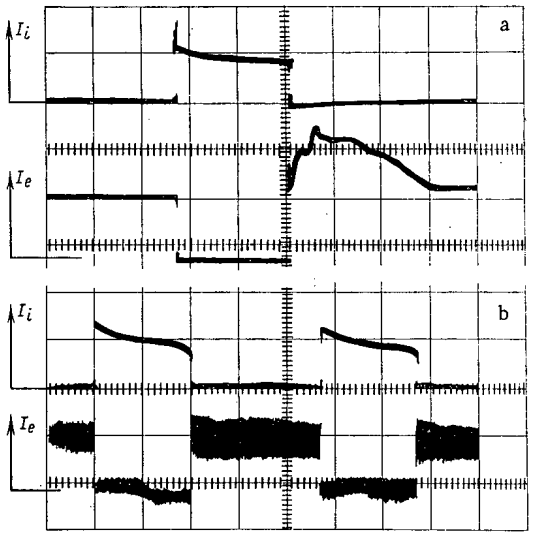

Fig. 4

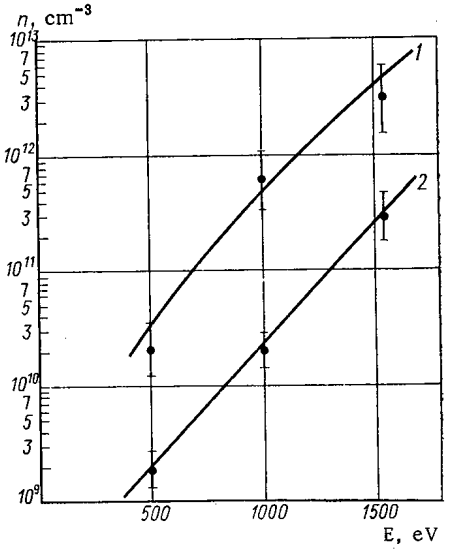

Fig. 5

Fig. 4. Oscillograms of injection current (the lower trace of each pair) and current to the ring electrode during pauses between injection pulses (the upper traces). a) Time scale 1 msec/div, electron current 2 mA/div, ion current 20 μA/div, H = 750 Oe, E = 300 eV, p = $2 \cdot 10^{-7}$ mm Hg; b) time scale 10 msec/div, H = 5550 Oe, p = $9 \cdot 10^{-7}$ mm Hg, E = 550 eV, I_e = 10 mA/div, I_i = 6 μA/div.

Fig. 5. Ion density as function of injection energy. p = 1.8 ± 10^{-7} mm Hg; τ_{inj} = 20 msec, 1) H = 5300 Oe, 2) H = 3750 Oe.

The rate of accumulation of ions is described by the equation

$$\frac{dn_i}{dt} = n_e n_0 < \delta_e v_e > - \frac{n_i}{\tau}, \qquad (3)$$

where n_e, v_e denote the electron density and velocity; σ_e is the cross section for ionization by electrons; n_i, τ denote the ion density and lifetime. The experimental results show that the number of accumulated ions increases with time (with duration of injection) and is directly proportional to the pressure (density) of the neutral gas. Increasing the duration of injection to 1-2 msec is accompanied by a rapid rise in the number of ions in the trap, to $\sim 10^{11}$, a density of $\sim 10^9$ cm^{-3}. Subsequent accumulation of plasma proceeds much more slowly for the following reasons. Ions will continue to accumulate in the trap for so long as the rate at which they are being lost is less than the rate at which they are being formed. The rate of formation of ions is proportional to the neutral gas density and to the density of fast electrons in the trap. On account of their low energy, the secondary electrons produced during the ionization of the residual gas will not contribute to any great extent to the rate at which ions are formed. Consequently, it is desirable to have in the trap as many fast electrons as possible. The injection current from the electron gun is limited, however, by the negative space charge within the trap. The number of fast electrons in the trap can be increased only by replacing secondary electrons lost from the trap by diffusion by electrons from the cathode of the electron gun. The rate of this process is small, since it is determined by the difference in the rates of diffusion of slow and fast electrons. Further, after the neutral gas in the trap has been completely ionized, further accumulation of ions under our conditions can occur only through ionization of gas entering the trap from the rest of the vacuum system, through the narrow gaps between the magnet coils.

The circuit for on-off modulation of the beam from the electron gun did not permit the duration of an injection pulse to be increased without limit. It was possible, however, to vary the repetition frequency of the injection pulses. Consequently, to permit investigation of the accumulation process, we utilized the following regime of operation. The injection current is raised to its maximum value, and the pauses between injection pulses arranged so that the plasma does not have time to collapse before the succeeding injection pulse is applied. The accumulation process is illustrated in Fig. 4, which shows oscillograms of the injection current and the ion current in the ring gap. The upper pair of oscillograms were taken at the beginning of the accumulation process, and the lower pair under conditions of saturation. The ion current is quite small while the injection pulse is being applied. Termination of injection, when the excess negative

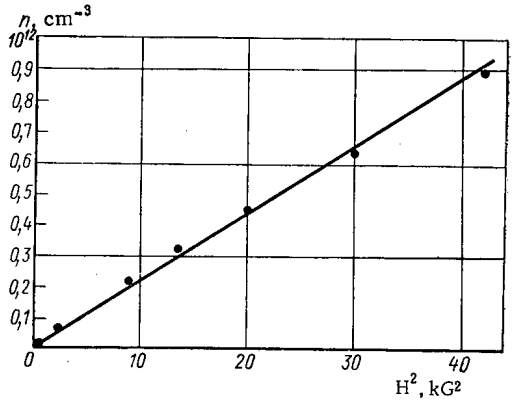

Fig. 6

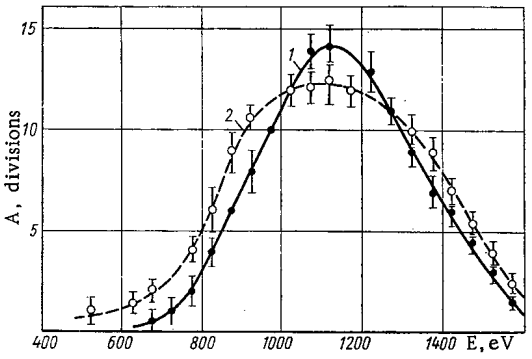

Fig. 7

Fig. 6. Ion density as function of magnetic field. $p = 10^{-6}$ mm Hg, E = 500 eV, I_e = 10 mA. Duration of injection pulses 20 msec; pause between injection pulses 2 msec.

Fig. 7. Electron energy distribution after injection has been switched off. E = 1700 eV, $p = 10^{-7}$ mm Hg; 1) $\tau_{delay} = 0$ μsec; 2) $\tau_{delay} = 1500$ μsec.

charge is no longer maintained by the electron current from the electron gun, is followed by a more intense loss of ions through the ring magnetic gap. The number of ions which leave during the pause between injection pulses is proportional to the density of accumulated ions. This quantity rises from pulse to pulse and reaches saturation in a few seconds. The pulse of ion current is almost rectangular. The ion lifetime was determined from the decay of the ion current when injection was switched off. It was 5-10 msec.

The pressure in the rest of the vacuum system (of volume 200 liters) was observed to fall during the accumulation process. Density estimates based on the reduction in pressure agree with estimates based on the number of ions leaving the trap through the ring gap during the pause.

The ion density in the trap under saturation conditions must be determined by the rate at which ions are being lost. The ions in the potential well can leave it either as a result of collisions, or as a result of diminution of potential in the magnetic gaps. The density limitation associated with ion loss through the magnetic gaps was discussed at the beginning of the article. It can be seen from Fig. 5 that the ion density increases with increasing energy of the injected-electrons. Increasing the energy of the injected electrons creates a deeper potential well and so shifts the density limit associated with the potential "sag" towards higher values. This also means that a greater current can be injected into the trap.

The loss of plasma through diffusion across the magnetic field must get less as the magnetic field is increased. Increasing the magnetic field will also counteract the diminution of potential in the magnetic gaps, which is proportional to the thickness of the sheet of electrons leaving the trap through the magnetic gaps. Figure 6 shows the square-law dependence of density on magnetic field. The maximum density estimated in our experiments is $\sim 10^{12}$ cm^{-3} (magnetic field in gaps ~5500 Oe, energy of injected electrons 1.5 keV, residual gas pressure 10^{-7} mm Hg). This value is almost 100 times greater than the density of the neutral gas. The low residual gas pressure implies a long accumulation time. This regime is justified, however, as the lifetime of the plasma particles increases as the neutral gas pressure is reduced.

The lifetime of electrons in the trap must depend on their energy. The slow, secondary electrons formed by ionization of the neutral gas and captured by the magnetic field must pass more rapidly to the walls of the trap than fast electrons. Figure 7 shows the energy distribution of electrons leaving the axial magnetic gap in the pause between injection pulses. One of these curves was measured immediately after the injection current was switched off. The other was measured 1.5 msec later. There are effectively no low-energy electrons. The mean energy of the electrons is ~1 keV; the energy of the electrons injected into the trap is 1700 eV. The energy distribution does not change much over 1.5 msec. This implies that fast electrons have a longer lifetime than cold electrons and that energy losses are small. This conclusion is further supported by measurements of the temporal dependence of the electron current in the axial magnetic gap for various retarding potentials.

The energy losses are characterized by the injection current under steady-state conditions. In the ideal case of zero losses, the injection current must "cut off" completely. In reality, the injection current goes to make up the losses. If the current is multiplied by the injection energy, we obtain the power P consumed in making good the losses in the trap. For E = 1700 eV and an injection current of 10 mA, P = 17 W. The total energy of the electrons in the trap is approximately equal to $W = \bar{E}N$, where $\bar{E}$ and N denote the mean energy and the number of electrons in the trap. For $\bar{E}$ = 1 keV we have W = 0.12 J. The energy lifetime can be estimated as $\tau_{energy} = W/P \approx 7.5$ msec. The loss of ions from the negative potential well must be accompanied by an increase in the depth of the well, and the loss of ions must occur simultaneously with the loss of electrons across the magnetic field. The main energy losses are, evidently, those due to the passage of electrons across the magnetic field.

The long lifetimes of the plasma particles testify to the stability of the plasma within the trap. Low-frequency oscillations of diochotron type [12] are observed to develop under saturation conditions (see Fig. 4) in the magnetic gaps of the trap. These oscillations further increase the rate at which cold electrons pass to the walls of the magnetic gaps.

LITERATURE CITED

1. Berkovich et al., Second Geneva Conference (1958) [Russian translation], Vol. 1, Atomizdat, Moscow (1959), p. 146.
2. H. Grad, Phys. Rev. Letters, 4, 222 (1960).
3. T. Allen and R. Bickerton, Nature, 191, 794 (1961).
4. M. G. Koval'skii, S. Yu. Luk'yanov, and I. M. Podgornyi, Yaderni Sintez, 1, 81 (1962).
5. D. Hagerman, Nuc. Fus. Suppl., 1, 75 (1962).
6. O. A. Lavrent'ev, Ukr. Fiz. Zh., 8, 440 (1963).
7. O. A. Lavrent'ev, Ukr. Fiz. Zh., 8, 446 (1963).
8. O. A. Lavrent'ev et al., Ukr. Fiz. Zh., 8, 452 (1963).
9. O. A. Lavrent'ev, in: Magnetic Traps [in Russian], Izd. AN USSR, Kiev (1965), Third Edition, p. 77.
10. A. Ware and J. Faulkner, Nucl. Fus., 9, 353 (1969).
11. K. D. Sinel'nikov et al., in: Plasma Physics and the Problems of Controlled Thermonuclear Synthesis [in Russian], Izd. AN USSR, Kiev (1965), Fourth Edition, p. 388.
12. Yu. I. Pankrat'ev et al., At. Énerg., 31, 274 (1971).

NONLINEAR THEORY FOR THE EXCITATION OF REGULAR OSCILLATIONS BY A RELATIVISTIC ELECTRON BEAM

V. I. Kurilko, A. P. Tolstoluzhskii, and Ya. B. Fainberg

UDC 621.384.6:621.3.038.624

1. The collective interaction of charged-particle beams with plasmas is an effective mechanism for exciting high-frequency fields and may be used, in particular, to accelerate charged particles [1, 2]. Nonlinear theory for this interaction has shown that the maximum amplitudes of the fields excited, governed by the opposition of these fields to the beam motion, increase with increasing electron energy. It is interesting in this connection to extend the study to relativistic electron beams. Nonlinear theory for the collective interaction of a relativistic electron beam with a plasma was first worked out in [3]. It was shown in [3-5] that the energy of a relativistic beam can be used efficiently to excite collective plasma oscillations. The primary interest in these studies, however, was in the instability of an unbounded homogeneous beam in an unbounded plasma, while under actual experimental conditions the beam is frequently injected into a bounded plasma. In this case new beam particles continuously enter the interaction region. The energy of the oscillations which they excite may accumulate in the plasma* and lead to an increase in the field amplitude.

The dynamics of the excitation of regular oscillations in an interaction between a modulated pulsed beam and a slow-wave cavity ($V_p \leq c$) was analyzed in [9, 10] with an account of accumulation. †

In this paper we will examine theoretically the dynamics of the development of the two-stream instability in the interaction of an unmodulated relativistic beam with such a cavity. Our goal is to determine the maximum amplitude of the excited field, with an account of the opposition of this field to the motion of the beam particles, and to determine the energy distribution of the beam at the cavity exit. This distribution is interesting, in particular, for the development of the self-acceleration of an electron beam proposed in [13].

2. We thus assume that an unmodulated pulsed electron beam is injected into a slow-wave cavity ($V_p = V_0$; where $V_0 \lesssim c$ is the velocity of the beam particles at the entrance to the cavity), in which a regular oscillation at frequency Ω and having a wave number $k_\parallel$ is excited. The condition of field regularity reduces to the requirement that the growth increment δl for the instability be small in comparison with the distance $\Delta\omega \equiv \Delta k_\parallel V_0 = \pi V_0/L$ (where L is the cavity length) between individual frequencies in the spectrum of driving forces exerted on the cavity by the beam [9, 10]. In this case we can neglect the excitation of spatial harmonics of the cavity field not in synchronism with the beam. Then the self-consistent system of equations for this problem can be written

$$\frac{\partial f}{\partial t} + v\frac{\partial f}{\partial z} + eE_\parallel \frac{\partial f}{\partial p} = 0; \tag{1a}$$

$$\frac{\partial^2 E_\parallel}{\partial t^2} + \Omega^2 E_\parallel = -4\pi \frac{\partial}{\partial t} j; \tag{1b}$$

$$j \equiv g(r) \int dp v(p) f(t, z, p); \quad E_\parallel \equiv E(t) \cos k_\parallel z \Phi(r); \quad 2\pi \int g(r)\, r\, dr = 1; \quad \Phi(0) = 1.$$

*Accumulation of the energy of irregular oscillations excited by an electron beam in a plasma half-space was studied in the quasilinear approximation in [6-8].

†The efficiency of the interaction of a relativistic beam with a retarding structure was studied in the approximation of a specified field in [11, 12] on the basis of the energy spectrum of the electrons leaving the system.

Translated from Atomnaya Énergiya, Vol. 32, No. 2, pp. 137-142, February, 1972. Original article submitted March 29, 1971.

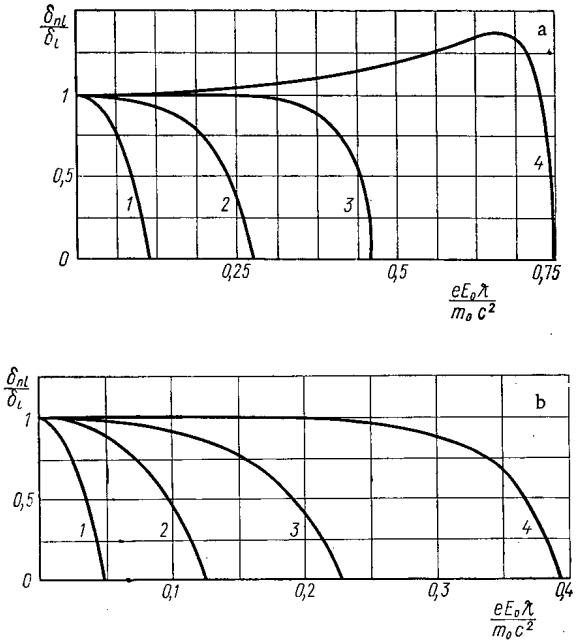

Fig. 1. Dependence of the growth increment on the field amplitude and injection energy for L = 4 (a) and L = 6 (b). 1) $\gamma_0 = 3$; 2) $\gamma_0 = 5$; 3) $\gamma_0 = 7$; 4) $\gamma_0 = 10$.

We assume here that the beam is focused in the z = const plane by a strong longitudinal magnetic field and that the characteristic transverse dimension of the beam is small in comparison with the corresponding wavelength ($|d(\ln g(r))/dr| \ll |d(\ln \Phi(r))/dr|$).

We seek a solution of kinetic equation (1a) by the method of characteristics:

$$\left.\begin{aligned} &\frac{\partial}{\partial\tau_1} p_1(\tau_1, q_0) = eE_{\|}[z_1(\tau_1, q_0);\ t(\tau_1, q_0)];\ p_1(0, q_0) = p_0; \\ &\frac{\partial}{\partial\tau_1} z_1(\tau_1, q_0) = v_1(p_1);\ z_1(0, q_0) = 0; \\ &q_0 \equiv (t_0, p_0);\ v(p) \equiv \frac{p}{m_0}\left[1 + \left(\frac{p}{m_0 c}\right)^2\right]^{-1/2}, \end{aligned}\right\} \quad (2)$$

where τ_1 is the Lagrange time of the particle which enters the cavity at time $t_0 \equiv t - \tau_1$ in Euler time, and z_1 and p_1 are the Lagrange coordinate and momentum of this particle.

If the z_1 and p_1 integrals in system (2) are known, the solution of kinetic equation (1a) is

$$df = dn\delta[z - z_1(\tau_1, q_0)]\,\delta[p - p_1(\tau_1, q_0)], \quad (3)$$

where $dn \equiv I(q_0)dq_0$ is the number of beam particles in the trajectory whose parameters q_0 lie in the interval $(q_0,\ q_0 + dq_0)$. The function $I(q_0)$ is determined unambiguously by the injection conditions; in our case of a monoenergetic beam, $dn = I(t_0)dt_0$ is the number of beam particles which enter the cavity during the time interval $(t_0,\ t_0 + dt_0)$, and $I(t_0)$ is the current of beam particles at the cavity entrance. We thus find the final expression for the beam current density in the cavity:

$$j(r, z, t) = eg(r)\int dt_0 I(t_0)\,\dot{z}_1(\tau_1, t_0)\,\delta[z - z_1(\tau_1, t_0)]; \quad (4)$$

$$0 < z_1(\tau_1, t_0) < L.$$

Substituting Eq. (4) into Eq. (1b), we find an equation giving the time dependence of the amplitude E_0 and the phase ψ of the field in the cavity ($E(t) \equiv -E_0(t)\cos[\Omega t - \psi(t)]$). The problem of finding the explicit form of trajectory z_1 as a function of the field amplitude is simplified because under the spectrum-regularity condition $\delta l \ll \Delta\omega$, which is equivalent to the requirement that the transit time $T_p \equiv L/V_0$ be small in comparison with the characteristic time $T_f \equiv \delta\bar{l}^{-1}$ of the field increase ($T_p \ll T_f$ [9, 10]), system (2) has a first integral [14]:

$$\begin{aligned} &\beta\gamma = \beta_0\gamma_0(1+\alpha) + \gamma_0[(1+\alpha)^2 - 1]^{1/2}\operatorname{sgn}\cos\zeta; \\ &\alpha \equiv R(\Theta)\beta_0^2\gamma_0\left\{\sin^2\zeta - \sin^2\left[\zeta + \frac{1}{2}\Delta(\tau, \zeta)\right]\right\}, \end{aligned} \quad (5)$$

where we have introduced the dimensionless variables $\beta \equiv \dot{z}_2/e$ (the particle velocity), $\gamma \equiv (1-\beta^2)^{-1/2}$ (the particle energy), $\Theta \equiv \Omega t$; $\tau \equiv \Omega t_1$; $2\zeta \equiv \Omega t_0$ (the phase at which the particle enters the cavity), $R(\Theta) \equiv eE_0(t)k_{\|}/m_0\Omega^2 = eE_0\lambda/m_0c^2\beta_0$ (the field amplitude), and $\Delta(\tau, \zeta) \equiv k_{\|}(z_1 - V_0\tau_1)$ (the field-induced deviation of the particle trajectory from the line $z_1 = V_0\tau_1$ corresponding to motion without a field).

The final equation for the time dependence of the field amplitude in the cavity is found by substituting (5) into the first integral of system (1), (2):

$$\begin{aligned} &\frac{dR^2}{d\Theta} + \frac{8J}{\beta_0}\int_0^{\pi} d\zeta\,\{\gamma\beta[T(R, \zeta); \zeta] - \gamma_0\beta_0\}; \\ &J \equiv \frac{4\pi e^2 I}{m_0 s\Omega^3 L};\ S \equiv 2\pi\int r\,dr\Phi^2(r). \end{aligned} \quad (6)$$

This relation could also be found directly from the energy-conservation law,

$$\frac{\partial W}{\partial t} + \operatorname{div}\mathbf{S} = -\mathbf{jE}$$

by integrating it over the cavity volume and averaging over an oscillation period.

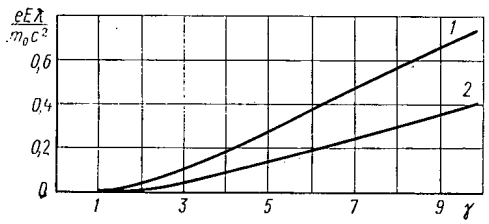

Fig. 2. Dependence of the maximum field amplitude on the injection energy. 1) L = 4; 2) L = 6.

Equation (6) shows that the field amplitude increases at a rate proportional to the rate at which energy is lost by beam particles in the cavity [15, 6-8].

The dependence of the transit time T of the particle across the cavity on the field amplitude R and the entrance phase ζ is given by the integral equation

$$k_{||}L = T(R, \zeta) + \Delta[T(R, \zeta); \zeta] = \int_0^{\Delta(T;\zeta)} d\Delta/\dot{\Delta} + \Delta(T; \zeta), \qquad (7)$$

which follows directly from $z_1(T; \zeta) = L$.

It is convenient to switch to a new variable in this latter equation, the phase $\varphi(R, \zeta)$ of the phase oscillations of the particle in the cavity field. Then the final system of equations giving the time dependence of the field amplitude is

$$\frac{dR}{d\Theta} = -\frac{4J\gamma_0}{\beta_0 R}\int_0^{\pi} d\zeta \{\beta_0 R_1 \sin^2\varphi - [(1+R_1\sin^2\varphi)^2 - 1]^{1/2}\operatorname{sgn}\cos\zeta\}; \qquad (8a)$$

$$\pi L - \gamma_0^2\left\{\left[\arcsin(\sin\zeta\cos\varphi) - \frac{\pi}{2}\right]\operatorname{sign}\cos\zeta - \zeta + \frac{\pi}{2}\right\} = \frac{\gamma_0^{3/2}}{\sqrt{R}}\int_0^{\varphi}\frac{dx\,(1+R_1\sin^2 x)}{[(2+R_1\sin^2 x)(1-\sin^2\zeta\cos^2 x)]^{1/2}}; \qquad (8b)$$

$$R_1 \equiv \beta_0^2\gamma_0 R\sin^2\zeta; \quad 2\pi L \equiv k_{||}L.$$

It is easy to see that in the case of a nonrelativistic beam ($\gamma_0^2 - 1 \ll 1$), Eq. (8) converts into the corresponding equation in [10], but Eq. (8b) is more symmetric in this case; we can carry out an analytic study and numerical calculations for arbitrary phase oscillations for the accelerated particles.

3. Let us analyze the solutions of system (8). At small field amplitudes ($\pi^2L^2R \ll \gamma_0^3$), we find, expanding the left and right sides of Eq. (8b) in series in powers of $R^{1/2}$,

$$\sin\varphi(R, \zeta) = \varphi_0[1 + A_3\varphi_0^2 + A_5\varphi_0^4 + \tilde{A}_7\varphi_0^6]; \quad \varphi_0 \equiv \pi L|\cos\zeta|(2R)^{1/2}\gamma_0^{-3/2}; \quad A_3 \equiv \mu t - \frac{1}{6}(1-t^2); \quad \mu \equiv \gamma_0^2/2\pi L; \quad t \equiv \operatorname{tg}\zeta;$$

$$A_5 \equiv 2\mu^2t^2 - \frac{7}{12}\mu t(1-t^2) + \frac{1}{120}(1-14t^2+t^4) - \frac{R_1}{4\varphi_0^2}; \quad \tilde{A}_7 \equiv \mu t\left[5\mu^2t^2 + \frac{1}{360}(31-254t^2+31t^4) - \frac{5R_1}{4\varphi_0^2}\right]. \qquad (9)$$

In the last term in Eq. (9) we have retained only those terms which make nonvanishing contributions after the averaging over the entrance phase ζ.

Substituting Eqs. (9) into Eq. (8a) and integrating over the entrance phases of the particles retarded ($0 < \zeta < \pi/2$) and accelerated ($\pi/2 < \zeta < \pi$) by the cavity field, we find the nonlinear increment δ_{nl} for the growth of the field amplitude, within terms of the order of R^2:

$$\frac{dR}{d\Theta} = \delta_{nl}(R^2)R; \quad \delta_{nl} \equiv -\frac{4J}{\beta_0 R}\int_0^{\pi} d\zeta[\gamma\beta(T, \zeta) - \gamma_0\beta_0] = \delta_l + \delta_l\frac{\pi^2L^2R^2}{4\gamma_0^2}\left[\frac{3}{4}(5-\beta_0^2) - \frac{\pi^2L^2}{90\gamma_0^2}(113-38\beta_0^2)\right]; \quad \delta_l \equiv \frac{\pi^3L^2}{\gamma_0^3}J. \qquad (10)$$

The first term in this equation, which corresponds to the growth increment of the linear theory, is governed by the second term in brackets in (9). Calculating the dependence of the particle energy at the cavity exist on the entrance phase, in the same approximation, from (5),

$$\gamma(\zeta) = \frac{1}{\gamma_0}\cdot\frac{\gamma_0^2\beta_0^2 + (1+\alpha)^2}{1+\alpha-\beta_0[(1+\alpha)^2-1]^{1/2}\operatorname{sgn}\cos\zeta}, \qquad (11)$$

we see that in the linear stage the energy distribution turns out to be asymmetric with respect to the injection energy, so that the energy of the particles at the cavity exist, averaged over the entrance phases, turns out to be equal the injection energy.

The nonlinear correction to the growth increment is seen from (10) to depend strongly on $\lambda \equiv 2\gamma_0/\pi L$. At small energies ($\lambda \ll 1$), the growth increment during the initial stage of growth decreases with increasing amplitude, while with $\lambda > 1$, on the other hand, it increases. The following physical explanation can be offered for this difference: at low injection energies and with long cavities, phase regrouping of the beam particles, which stabilizes the growth of the field amplitude, manages to occur even at low amplitudes.*

*The stabilization of the growth of regular oscillations due to a change in the beam distribution function in coordinate space, due to phase oscillations of beam particles captured by the wave, occurs even when there is a slight deformation of this function in velocity space [2, 16, 17]; for irregular oscillations, the effect turns out to be predominant [6, 7, 18, 19].

For this reason, the energy taken from the beam by the field turns out to be small [10], so the decrease in the longitudinal mass of the retarded particles, which lead to an increase in the growth increment, does not become apparent. For short cavities and for relatively large injection energies ($\lambda > 1$), the decrease in the longitudinal mass at the beginning of the interaction turns out to be more important than the phase regrouping, which does not manage to occur under these conditions. For this reason, the growth increment, which is inversely proportional to the longitudinal mass, increases with increasing field amplitude in the latter case.

Equations (9) and (10) lose their validity for large field amplitudes ($\pi^2 L^2 R \gtrsim \gamma_0^2$), so system (8) was solved numerically to find the dependence of the nonlinear increment on the field amplitude and to find the dependence of the maximum amplitude on the injection energy and the energy distribution of the beam particles at the cavity exit. The $\varphi(\zeta)$ dependence was calculated for fixed injection energy γ_0, cavity length L, and field amplitude R for 100 retarded and 100 accelerated particles. The nonlinear growth increment ($\delta_{nl} \equiv R'/R$) was determined from these dependences with the help of Eq. (8a). Figure 1 shows the dependence of the nonlinear increments on the field amplitude for several γ_0 and L values.

Here the ordinate axes show the ratio of the nonlinear growth increment δ_{nl} to the corresponding linear increments. The abscissa axes show the field amplitude in units of $eE_0\lambda/m_0c^2$ (the energy acquired by a particle over a wavelength). This figure shows that with $\lambda < 1$ the growth increment δ_{nl} decreases monotonically with increasing amplitude, while with $\lambda > 1$ it increases at small amplitudes and begins to decrease only near the maximum values of this amplitude. The critical injection energy $\gamma_* \equiv (\pi/6)L\sqrt{10}$ at which the growth increment δ_{nl} begins to increase with increasing amplitude is found from the condition for the vanishing of the coefficient of R^2 in (10). It is easy to see that we have γ_* (L = 4) ≈ 6.7, and γ_* (L = 6) ≈ 10, in complete agreement with the results of the numerical calculation, shown in Fig. 1.

As a result of the increase on the increment with increasing field amplitude with $\lambda > 1$, there is also an increase in the field intensity R_{eff} corresponding to the maximum efficiency of the beam–cavity interaction (to the maximum growth rate of the field amplitude). There is accordingly an increase in the magnitude of this maximum. It is easy to see that with $\gamma_0 > \pi L$, the corresponding field amplitude is approximately maximal ($R_{eff} \simeq R_{max}$).

Figure 1 also shows that the length of the current pulse required to reach the maximum amplitude R_{max} differs from the time R_{max} characterizing the field growth in linear theory by a numerical coefficient of the order of unity, approximately equal to $\ln((R_{max} - R_0)(R_0 \equiv R(0))$.

Figure 2 shows dependences of the maximum field amplitude corresponding to the vanishing of the nonlinear increment δ_{nl} on the injection energy γ_0 for two cavity lengths L. In this range of parameters the maximum field amplitude is seen to increase linearly with increasing injection energy.

Figure 3 shows dependences of the particle energy at the cavity exit on the entrance phase $\vartheta \equiv 2\zeta$ for the maximum field amplitude and for an injection energy of $\gamma_0 = 5$. It is easy to see that many of the beam particles have energies of the order of twice the injection energy at the cavity exit. The dependences of the energy on the injection phase are similar for other injection energies ($\gamma_0 = 7$; 10), we so conclude that this cavity is suitable for self-acceleration of a relativistic electron beam [13].

These results refer to injection energies which are not too high, in which case the maximum amplitudes of the excited field are relatively low. In this case ($eE_0\lambda/m_0c^2 < 1$), the dependence of the phase φ of the phase oscillations on ζ is continuous. It can be shown that at sufficiently high field amplitudes ($R > R_{cr}$), the $\varphi(\zeta)$ dependence becomes discontinuous. The critical field amplitude, corresponding to the appearance of discontinuities in $\varphi(\zeta)$, can be found by differentiating Eq. (8b) with respect to ζ. Equating the coefficient of $d\varphi/d\zeta$ to zero, we find

$$R \sin^2 \zeta_* \sin^2 \varphi(R, \zeta_*) = \frac{\gamma_0}{\gamma_0 + 1}. \tag{12}$$

It is easy to see that this equation can have real solutions only for sufficiently high field amplitudes:

$$R > R_{cr} \equiv \frac{\gamma_0}{\gamma_0 + 1}; \quad \left(\frac{eE_{cr}\lambda}{m_0c^2} = \sqrt{\frac{\gamma_0 - 1}{\gamma_0 + 1}}\right).$$

In the nonrelativistic case, we have $R_{max} \ll 1$ [10], so this inequality cannot hold. At relativistic injection energies, it holds when $R_{max} \geq R_{cr} \approx 1$. By continuing the lines in Fig. 3 to the line $eE_0\lambda/m_0c^2 = 1$, we find the following values for the corresponding injection energies: γ_{cr} (L = 4) ≈ 13; γ_{cr} (L = 6) ≈ 20.

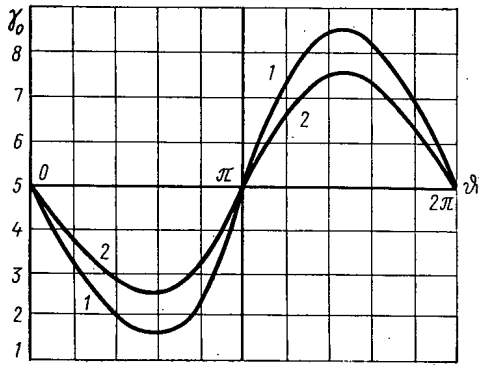

Fig. 3. Dependences of particle energies at the cavity exit on the entrance phase ($\gamma_0 = 5$): 1) L = 4; 2) L = 6.

Substituting (12) into (5), we see that the point ζ_* corresponds to a particle which loses all its energy during the transit time and stops at the cavity exit. This can occur only at sufficiently large field amplitudes, in accordance with inequality (12a).

It should be noted here that the discontinuities in the first integral of the system of characteristic equations (2) at v = 0 occur because the derivative dp/dz becomes infinite at this point. A similar situation is known to occur in the kinetic theory of a steady-state diode [20], for which the corresponding characteristic separates the particles returning to the cathode and going on to the anode. In our problem, with inequality (12a), the beam electrons can also return, particularly since electrons which have lost much of their energy can be captured by the oppositely directed wave. However, since we neglected this wave in equations of motion (2) and in first integral (5), our analysis holds only when inequality (12a) does.

The authors thank G. Ya. Lyubarskii for useful advice.

LITERATURE CITED

1. Ya. B. Fainberg, Proc. Symp. CERN, 1, 84 (1956); At. Énerg., 6, 431 (1959); Usp. Fiz. Nauk, 93, 617 (1967).
2. Ya. B. Fainberg, At. Énerg., 11, 313 (1961).
3. Ya. B. Fainberg and V. D. Shapiro, in: Interaction of Charged-Particle Beams with Plasmas [in Russian], Izd. Akad. Nauk USSR, Kiev (1965), p. 92.
4. Ya. B. Fainberg, V. D. Shaprio, and V. I. Shevchenko, Zh. Éksp. Teor. Fiz., 57, 966 (1969).
5. L. I. Rudakov, Zh. Éksp. Teor. Fiz., 59, 2091 (1970).
6. A. A. Vedenov, At. Énerg., 13, 5 (1962).
7. Ya. B. Fainberg and V. D. Shapiro, Zh. Éksp. Teor. Fiz., 47, 1389 (1964).
8. B. N. Breizman and D. D. Ryutov, Zh. Éksp. Teor. Fiz., 57, 1401 (1969); ZhÉTF Pis. Red., 11, 606 (1970).
9. V. I. Kurilko and I. Ullshmid, Nuclear Fusion, 9, 129 (1969).
10. V. I. Kurilko, Zh. Éksp. Teor. Fiz., 57, 885 (1969).
11. M. I. Petelin, Izv. VUZ. Radiofiz., 13, 1586 (1970).
12. V. K. Yulpatov, Izv. VUZ. Radiofiz., 13, 1784 (1970).
13. L. N. Kazanskii, A. V. Kisletsov, and A. N. Lebedev, At. Énerg., 30, 27 (1971).
14. J. Slater, Rev. Mod. Phys., 20, 473 (1948).
15. L. Brillouin, J. Appl. Phys., 20, 1196 (1949).
16. A. V. Gaponov, Zh. Éksp. Teor. Fiz., 39, 326 (1960); A. V. Gaponov, M. I. Petelin, and V. K. Ylpatov, Izv. VUZ. Radiofiz., 10, 1414 (1967).
17. V. B. Krasovitskii and V. I. Kurilko, Zh. Éksp. Teor. Fiz., 48, 383 (1965); 49, 1831 (1965); V. B. Krasovitskii, V. I. Kurilko, and M. A. Strzhemechnyi, At. Énerg., 24, 545 (1968).
18. A. A. Vedenov, E. P. Belikhov, and R. Z. Sagdeev, Usp. Fiz. Nauk, 73, 701 (1961); Nuclear Fusion, Suppl. II, 465 (1962).
19. W. Drummond and D. Pines, Nuclear Fusion, Suppl. III, 1049 (1962).
20. A. A. Vlasov, Many-Particle Theory [in Russian], Gostekhizdat, Moscow–Leningrad (1950).

VERIFICATION OF NEUTRON DIFFUSION THEORY FOR A MEDIUM WITH CHANNELS (LATTICE OF CHANNELS WITH LARGE TRANSVERSE DIMENSIONS) BY MEANS OF THE PULSE METHOD

I. F. Zhezherun

UDC 621.039.512.4:546.45

The diffusion parameters of virtually all the moderators used in atomic engineering have been measured by means of pulsed neutron sources. Papers on the pulse method of investigating diffusion in anisotropic media have appeared in recent years. In almost all the published papers, the anisotropic media consisted of lattices of empty (more accurately, air-filled) channels in different moderators: Plexiglas [1], heavy and ordinary water [2, 3], beryllium oxide [4], and graphite [5-8]. The longitudinal $D_{\parallel}$ and the transverse $D_{\perp}$ diffusion coefficients characterizing diffusion along and across the channels were measured for these media. Table 1 provides the published data on $D_{\parallel}$ and $D_{\perp}$, reduced to the diffusion coefficient D_0 for the continuous medium, which has also been measured by means of the pulse method.

The value of D_0 is usually obtained by analyzing the dependence of the neutron decay (damping) constant α in moderator blocks of different sizes on the geometric parameter B^2 of blocks by using the well-relationship (see, for instance, [9]):

$$\alpha_{0} = (v\Sigma_a)_0 + D_0B^2 - C_0B^4. \quad (1)$$

Here, $(v\Sigma_a)_0$ is the neutron absorption rate per unit volume of the block material, and D_0 and C_0 are the diffusion and diffusion cooling coefficients, respectively.

For a moderator in the shape of a rectangular parallelepiped,

$$B^2 = \pi^2 (x_{\text{eff}}^{-2} + y_{\text{eff}}^{-2} + z_{\text{eff}}^{-2}), \quad (2)$$

where x_{eff}, y_{eff}, and z_{eff} are the effective block dimensions along the x, y, and z axes.

The values of $D_{\perp}$ and $D_{\parallel}$ given in Table 1 were obtained by means of a relationship which is a generalization of (1):

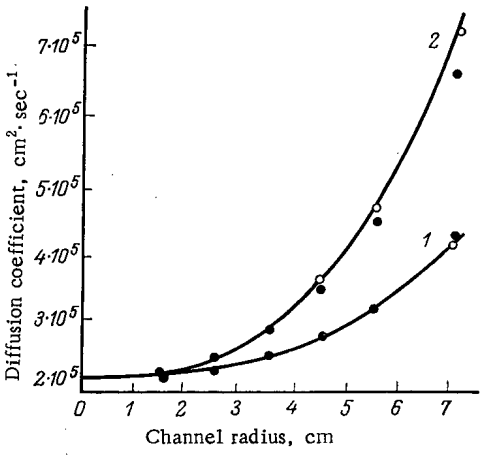

Fig. 1. Comparison between the experimental and theoretical diffusion coefficients for lattices of empty channels in graphite. 1) and 2) Theoretical values of $D_{\perp}$ and $D_{\parallel}$ after Benoist, respectively; the black points are the experimental results from [8]; the white points are the results from [8], recalculated for channels of finite length.

Translated from Atomnaya Énergiya, Vol. 32, No. 2, pp. 143-152, February, 1972. Original article submitted May 6, 1971; revision submitted June 29, 1971.

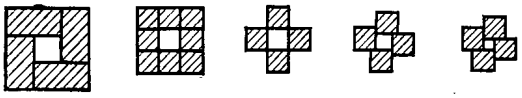

Fig. 2. Briquet arrangements for square lattices of empty channels (plan). 1) Lattice of 5 × 5-cm channels spaced at 15 cm in beryllium oxide; 2)-5) channel lattices in beryllium (2, 4 × 4-cm section and 12-cm spacing; 3, 4 × 4-cm section and 5.64-cm spacing; 4, 3 × 3-cm section and 5.0-cm spacing; 5, 2 × 2-cm section and 4.47-cm spacing).

$$\alpha = v\Sigma_a + D_\perp B_\perp^2 + D_\parallel B_\parallel^2 - C_\perp B_\perp^4 - C_\parallel B_\parallel^4 - C_\times B_\perp^2 B_\parallel^2, \qquad (3)$$

where $B_\perp^2 = \pi^2(x_{eff}^{-2} + y_{eff}^{-2})$; $B_\parallel^2 = \pi^2 z_{eff}^{-2}$ (the z axis is directed along the channels).

Relationship (3) has been used in different ways. Thus, it was assumed in [1, 4] that $C_\times = 0$; in [2, 5], all the diffusion cooling coefficients, i.e., the terms with $B_{\perp,\parallel}^4$, were rejected. This was justified to a certain extent in [5], where $D_\parallel$ was obtained experimentally for a large graphite block (EGCR reactor without fuel-containing channels) by combining the pulse and the exponential methods, but it was completely unjustified in [2], where the authors explain the discrepancy between their results and theoretical data mainly by the diffusion cooling effect. All the diffusion cooling coefficients were taken into account in other papers. However, it was assumed in [8] that

$$C_\times = C_\perp + C_\parallel. \qquad (4)$$

The calculated values given in Table 1 were obtained by means of the following expressions: The value of $D_\parallel$ was obtained by means of Behrens' equation [10], which was subsequently derived by many authors using various methods*; the value of $D_\perp$ was obtained by means of the equations of Behrens [10], Carter [13], Benoist [14, 15], and also of Leslie [3], which yield values that coincide with those obtained by means of the Benoist equation [14].

The above equations were obtained in the single-velocity approximation. This approximation is justified for graphite, beryllium, and beryllium oxide, where only a small percentage of neutrons possesses energies in the region of Bragg jumps at ordinary temperatures (where the dependence of the transport mean free path λ (v) on the neutron velocity v is important) and less justified for heavy, and especially, ordinary, water.

The following remarks should be made regarding the data in Table 1. First, the above-mentioned arbitrariness in using relationship (3), which is due to a lack of a rigorous theory, makes it somewhat difficult to compare the experimental data with other and with theoretical calculations, since different assumptions concerning C_i can affect appreciably the diffusion coefficients D_i. For instance, it is indicated in [6] that the assumption $C_\times = 0$ leads to the implausible result $D_\perp > D_\parallel$. A theoretical discussion of the diffusion cooling coefficients in porous media is given in [16]. This paper substantiates relationship (3), demonstrates the validity of expression (4) for an anisotropic medium, and establishes that

$$\frac{C_\parallel}{C_\perp} = \left(\frac{D_\parallel}{D_\perp}\right)^2. \qquad (5)$$

if λ(v) is independent of the velocity. These theoretical results simplify the use of expression (3) in experimental investigations. They also confirm the admissibility of comparing most of the data given in Table 1 with theoretical calculations and with each other, since relationship (4) was satisfied within the limits of the error in C_i in experiments where this relationship was not used beforehand.

In using relationships (4) and (5), there remains an arbitrary coefficient ($C_\perp$ or $C_\parallel$), which should be expressed in terms of known quantities. The point is that the aim of experiments with pulsed neutron sources in porous media is different from the aim of similar experiments with solid blocks. Actually, while the material characteristics that can be used in calculations are measured in experiments of the latter type, the diffusion coefficients $D_\parallel$ and $D_\perp$ are far from being such universal quantities. Besides the characteristics of the material, they also include the characteristics of the channels (porosity and channel dimensions and shape). Therefore, the purpose of experiments in porous media is the verification of theoretical expressions for $D_\parallel$ and $D_\perp$. Consequently, it would be desirable to have theoretical expressions also for the other coefficients in expression (3) ($C_\perp$, $C_\parallel$ and $C_\times$).

*Expressions similar to Behrens' equations were derived in 1948 by S. L. Sobolev and V. S. Furs (cited in [11, 12]).

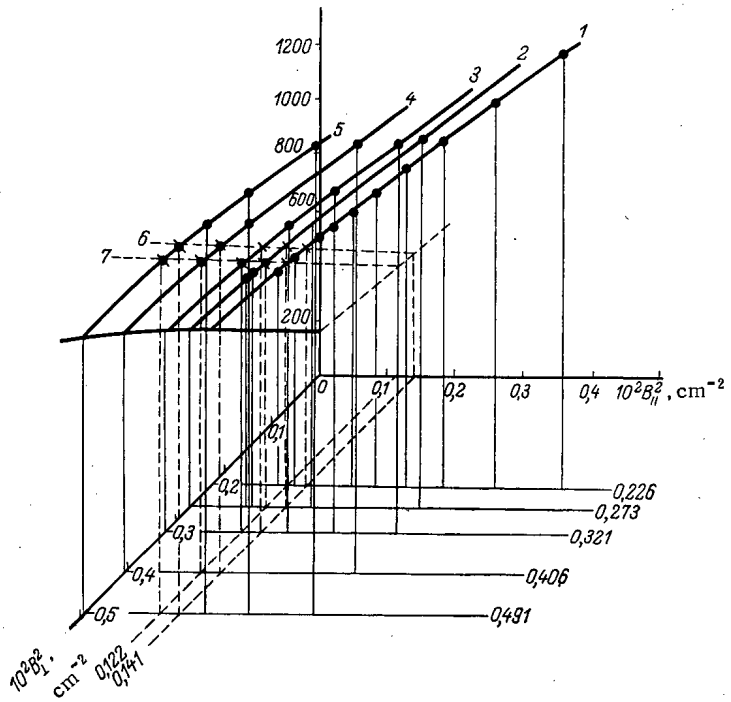

Fig. 3. Results obtained in measuring the decay constants α for beryllium-oxide blocks in a $B_{\perp}^2$, $B_{\|}^2$, α coordinate system. The points and crosses represent the α values when only $B_{\|}^2$ or $B_{\perp}^2$ varies. Curves 1-5 represent the intersections of the surface $\alpha = v\Sigma_a + D_{\perp}B_{\perp}^2 + D_{\|}B_{\|}^2 - C_{\perp}B_{\perp}^4 - C_{\|}B_{\|}^4 - (C_{\perp} + C_{\|})B_{\perp}^2B_{\|}^2 - GB_{\|}^3$ by the planes $B_{\perp}^2$, equal to $0.226 \cdot 10^{-2}$, $0.273 \cdot 10^{-2}$, $0.321 \cdot 10^{-2}$, $0.406 \cdot 10^{-2}$, $0.491 \cdot 10^{-2}$ cm^{-2}; curves 6 and 7 represent the intersections of the surface by the planes $B_{\|}^2$, equal to $0.122 \cdot 10^{-2}$ and $0.141 \cdot 10^{-2}$ cm^{-2}.

A simple derivation of expressions for the diffusion cooling coefficients in a porous medium is given in [17]. It has been shown that

$$C_{\perp} = C_0\left(\frac{D_{\perp}}{D_0}\right)^2; \quad C_{\|} = C_0\left(\frac{D_{\|}}{D_0}\right)^2; \qquad C_{\times} = 2C_0\frac{D_{\perp}D_{\|}}{D_0^2}. \tag{6}$$

Relationship (5) and the approximate relationship (4) are obtained from these expressions.

The second remark concerns the results pertaining to channels with large cross sections. It is evident from Table 1 that the experimental values of $D_{\perp}$ almost always (except the results of [2]) coincide with the values calculated by means of the Carter and Benoist equations within the limits of measurement accuracy.*

For channels with a large cross section [$(R/\lambda) > 1.5$; $R = 2V/S$ is the hydraulic radius of the channel, and V and S are its volume and surface area, respectively], the theoretical values of $D_{\|}$ somewhat exceed the experimental values, the more so, the larger the channel radius. This is clearly shown in Fig. 1 (black points), borrowed from [8]. The authors of this very thorough experimental and theoretical work, who are engaged in an extensive program of investigation of heterogeneous media (including lattices of empty channels and lattices containing pure absorbers and fissionable materials), have indicated that the finite channel length could be a possible cause of the above discrepancy, which they intend to investigate.

However, in investigating the neutron leakage from a moderator block with a single channel, an expression was derived in [11] for the correction for longitudinal leakage in considering a channel of finite

*The theoretical inadequacy of Behrens' equation for $D_{\perp}$ was first indicated in [18].

TABLE 1. Results of Measuring the Diffusion Coefficients in Anisotropic Media (Lattices of empty channels in the moderator) by means of the Pulse Method

Anisotropic medium reference	Dimension or radius of channel		Lattice spacing		Ratio of cavity volume to volume of solid material p	$D_\perp/D_0$				$D_\parallel/D_0$		Remark
						experiment	calculation			experiment	calculation	
	cm	R/λ	cm	α/λ			Benoist [14], Leslie [3]	Carter [13]	Behrens [10]			
Square lattice of round-section channels in Plexiglas [1]	0,85 0,85	1,93 1,93	2,90 3,60	6,60 8,16	0,368 0,213	1,41±0,10 —	— —	— —	1,789 —	2,18±0,19 —	2,308 —	Assumption: $C_\times = 0$
Same, in heavy water [2]	7,2 7,2 3,8 3,8 3,8	2,95 2,95 1,56 1,54 1,56	32,0 24,0 32,0 24,0 16,0	13,1 9,84 13,1 9,84 6,55	0,189 0,394 0,0463 0,0854 0,2152	1,19±0,030 1,375±0,030 1,044±0,030 1,117±0,030 1,252±0,030	1,584 2,026 1,105 1,179 1,400	1,363 1,731 1,093 1,142 1,338	1,694 2,222 1,129 1,203 1,449	1,731±0,060 2,406±0,098 1,277±0,050 1,326±0,060 1,539±0,086	2,204 3,128 1,190 1,325 1,711	$D_0 = 2.02 \cdot 10^5$ cm²/sec; it is assumed that $C_\parallel$, $C_\perp$ and $C_\parallel$, $C_\times$ equal zero
Triangular lattice of round-section channels in water [3]	1,65	3,84	9,35	21,7	0,452	1,24±0,04	1,21	—	1,51	—	—	Transport mean free path λ = 0.431 cm
Square lattice of round-section channels in graphite [5]	—	—	—	—	—	—	—	—	—	1,116±0,016	1,112	$C_\perp$, $C_\parallel$, and $C_\times$ equal zero; λ = 2.5 cm
Square lattice of square-section channels in beryllium oxide [4]	5×5	1,55	15,0	9,3	0,125	1,192±0,009	—	—	1,303	1,31±0,02	1,495	$D_0 = 1.34 \cdot 10^5$ cm²/sec; λ = 1.61 cm; $C_\times = 0$
Square lattice of round-section channels in graphite [6]	0,8	0,317	2,0	0,79	1,01	2,13±0,04	1,906	1,906±±0,006	2,169±±0,007	2,28±0,08	2,328±±0,013	$C_\times \neq C_\perp + C_\parallel$
Same, data borrowed from [7]	1,60 3,81 5,07 3,81 5,07 3,81 5,07	0,64 1,53 2,03 1,53 2,03 1,53 2,03	14,6 14,6 14,6 19,5 19,5 24,3 24,3	5,86 5,86 5,86 7,84 7,84 9,78 9,78	0,0371 0,2138 0,3801 0,1203 0,2138 0,0770 0,1369	1,05±0,01 1,33±0,04 1,98±0,08 1,12±0,05 1,42±0,07 1,05±0,02 1,22±0,06	1,05 1,42 1,98 1,21 1,44 1,13 1,25	1,05 1,42 1,94 1,22 1,44 1,13 1,26	1,05 1,56 2,20 1,32 1,68 1,20 1,43	1,08±0,04 2,00±0,10 2,62±0,18 1,39±0,05 1,88±0,07 1,22±0,03 1,50±0,06	1,09 1,91 3,02 1,51 2,14 1,33 1,73	$D_0 = 2.06 \cdot 10^5$ cm²/sec; λ = 2.49; $C_\times \neq C_\parallel + C_\perp$
Same, data borrowed from [8]	1,5 2,5 3,5 4,5 5,5 7,0	0,6 1,0 1,4 1,8 2,2 2,8	20,0	8,0	0,0180 0,0516 0,1064 0,1890 0,3114 0,6251	1,017±0,007 1,068±0,007 1,159±0,010 1,300±0,010 1,507±0,015 2,019±0,024	1,023 1,074 1,161 1,295 1,492 1,984	— — — — — —	— — — — — —	1,050±0,010 1,150±0,010 1,343±0,014 1,647±0,019 2,121±0,024 3,208±0,039	1,037 1,145 1,362 1,724 2,268 3,504	$D_0 = 2.07 \cdot 10^5$ cm²/sec; λ = 2.5 cm; $C_\times = C_\perp + C_\parallel$

Declassified and Approved For Release 2013/03/01 : CIA-RDP10-02196R000300100002-9

TABLE 2. Measurement of the Decay Constant α in Blocks with Empty Channels

Medium	Characteristics of the medium	Block dimensions along the axes, cm			α, sec^{-1}	$B^2 \cdot 10^2$, cm^{-2}
		x	y	z (parallel with the channels)		
1	Square lattice of channels with 5×5-cm sections in beryllium oxide. Lattice parameters: $a = 15.0$ cm; R = 2.5 cm; $R/\lambda = 1.337$; p = 0.125	60,2	60,2	50,0	1709,1	0,832
		75,3	60,2	50,0	1563,1	0,747
		90,4	90,4	40,0	1549,4	0,740
		60,2	60,2	60,0	1524,6	0,733
		60,2	60,2	70,0	1413,7	0,672
		75,4	75,3	50,0	1407,2	0,662
		75,4	75,3	50,0	1411,8	0,662
		90,4	90,4	45,0	1365,1	0,640
		60,2	60,2	80,0	1323,8	0,631
		60,2	60,2	80,0	1337,5	0,631
		75,4	90,4	50,0	1323,1	0,614
		60,2	60,2	90,0	1281,3	0,603
		60,2	60,2	90,0	1271,8	0,603
		75,3	60,2	70,0	1265,6	0,587
		90,4	90,4	50,0	1243,7	0,567
		75,4	75,3	60,0	1221,3	0,563
		75,4	60,2	80,0	1201,7	0,546
		75,3	60,2	90,0	1128,1	0,518
		75,3	60,2	90,0	1117,0	0,518
		90,4	90,4	55,0	1140,7	0,511
		75,4	75,3	70,0	1108,4	0,509
		75,4	75,3	70,0	1115,7	0,509
		90,4	90,4	60,0	1051,8	0,468
		75,4	75,3	80,0	1036,3	0,461
		75,4	75,3	80,0	1041,6	0,461
		75,4	90,4	70,0	1033,1	0,454
		90,4	90,4	65,0	985,7	0,434
		75,4	75,3	90,0	978,1	0,433
		75,4	75,3	90,0	981,7	0,433
		75,4	90,4	80,0	956,7	0,413
		90,4	90,4	70,0	932,9	0,407
		90,4	90,4	70,0	936,9	0,407
		75,4	90,4	90,0	885,1	0,385
		75,4	90,4	90,0	894,5	0,385
		90,4	90,4	75,0	888,5	0,384
		90,4	90,4	80,0	863,7	0,366
		90,4	90,4	80,0	875,3	0,366
		75,4	90,4	100,2	840,0	0,364
		75,4	90,4	105,1	828,0	0,356
		90,4	90,4	85,0	823,7	0,351
		90,4	90,4	90,0	803,9	0,338
		90,4	90,4	90,0	805,3	0,338
		90,4	90,4	95,0	770,4	0,327
2	Square lattice of 4×4-cm channels in beryllium. Lattice parameters: $a = 12.0$ cm; R = 2.0 cm; $R/\lambda = 1.342$; p = 0.125	48,3	60,1	44,0	1864,0	1,072
		60,4	60,1	44,0	1688,0	0,939
		60,2	60,4	60,0	1389,2	0,745
		60,4	60,3	80,0	1188,0	0,641
		60,4	84,4	60,0	1229,5	0,625
		60,4	72,4	68,0	1179,2	0,618
3	Same. Lattice parameters: $a = 5.64$ cm; R = 2.0 cm; $R/\lambda = 1.342$; p = 1.0	64,0	64,0	64,0	2052,4	0,775
		64,0	72,4	56,0	2107,3	0,680
		56,0	56,0	84,0	2134,7	0,642
		80,0	74,0	44,0	2349,6	0,621
		56,0	56,0	56,0	2535,8	0,608
4	Square lattice of 3×3-cm channels in beryllium. Lattice parameters: $a = 5.0$ cm; R = 1.5 cm; $R/\lambda = 1.01$; p = 0.5625	50,0	50,0	48,0	2506,1	1,047
		50,0	50,0	80,0	1975,7	0,822
		65,0	65,0	48,0	1929,5	0,781
		60,0	55,0	64,0	1830,1	0,742
5	Square lattice of 2×2-cm channels in beryllium. Lattice parameters: $a = 4.47$ cm; R = 1.0; $R/\lambda = 0.67$; p = 0.250	49,2	53,6	56,0	1798,7	0,952
		58,1	62,6	48,0	1676,9	0,871
		40,2	53,6	68,0	1658,6	0,865
		53,6	58,1	56,0	1648,0	0,854

length. This correction is applied by adding to the right-hand side of (3) the term $-GB_{\parallel}^3$ [17], where

$$G = 1.725 \frac{p}{1+p} Q \frac{R^2}{\lambda} D_0, \tag{7}$$

while Q is a coefficient dependent on the channel shape.

TABLE 3. Results of Measurements of the Diffusion Parameters in Anisotropic Media, Compared with the Calculated Values

Medium	Anisotropic medium	Channel dimensions, cm	Channel dimensions, R/λ	Lattice spacing a, cm	Lattice spacing a, a/λ	Ratio p of cavity volume to material volume	$v\Sigma_a$, sec^{-1}	$D_\perp/D_0$, experiment	$D_\perp/D_0$, calculation, Carter [13]	$D_\perp/D_0$, calculation, Behrens [10]	$D_\parallel/D_0$, experiment	$D_\parallel/D_0$, calculation	Experiment, $C_\perp \cdot 10^{-5}$, cm^4/sec	Experiment, $C_\parallel \cdot 10^{-5}$, cm^4/sec	Remark
1	Square lattice of empty channels in beryllium oxide	5×5	1,337	15,0	8,03	0,125	159,0	1,844±±0,037 1,91±±0,03 1,88±±0,01	1,85	1,97	2,201±±0,055 2,09±±0,02 2,07±±0,02	2,23	2,41±±6,35 10,7±±6,0 —	27,38±±11,90 — —	$c_\times = c_\perp + c_\parallel$; $c_\times = c_\perp + c_\parallel$, $c_\parallel = c_\perp \left(\frac{D_\parallel}{D_\perp}\right)^2$; $c_\times = c_\perp + c_\parallel$, $c_{\perp,\parallel} = c_0 \left(\frac{D_{\perp,\parallel}}{D_0}\right)^2$
2	Square lattice of empty channels in beryllium oxide	4×4	1,342	12,0	8,05	0,125	234,2	1,45±±0,08 1,45±±0,04	1,48	1,85	2,08±±0,14 1,84±±0,06	2,05	10,9±±4,0 —	— —	$c_\times = c_\perp + c_\parallel$, $c_\parallel = c_\perp \left(\frac{D_\parallel}{D_\perp}\right)^2$; $c_\times = c_\perp + c_\parallel$, $c_{\perp,\parallel} = c_0 \left(\frac{D_{\perp,\parallel}}{D_0}\right)^2$
3	Same	4×4	1,342	5,64	3,78	1,00	136,2	3,12±±0,15 3,07±±0,05	2,83	2,98	4,07±±0,24 3,97±±0,09	3,90	26,1±±21,5 —	— —	$c_\times = c_\perp + c_\parallel$, $c_\parallel = c_\perp \left(\frac{D_\parallel}{D_\perp}\right)^2$; $c_\times = c_\perp + c_\parallel$, $c_{\perp,\parallel} = c_0 \left(\frac{D_{\perp,\parallel}}{D_0}\right)^2$
4	"	3×3	1,01	5,0	3,35	0,5625	173,2	2,16±±0,09 2,25±±0,04	2,12	2,19	2,49±±0,14 2,62±±0,08	2,70	1,04±±0,6 —	— —	$c_\times = c_\perp + c_\parallel$, $c_\parallel = c_\perp \left(\frac{D_\parallel}{D_\perp}\right)^2$; $c_\times = c_\perp + c_\parallel$, $c_{\perp,\parallel} = c_0 \left(\frac{D_{\perp,\parallel}}{D_0}\right)^2$
5	"	2×2	0,67	4,47	3,0	0,25	212,6	1,76±±0,22 1,70±±0,04	1,64	1,66	1,85±±0,24 1,80±±0,09	1,84	11,3±±24,1 —	— —	$c_\times = c_\perp + c_\parallel$, $c_\parallel = c_\perp \left(\frac{D_\parallel}{D_\perp}\right)^2$; $c_\times = c_\perp + c_\parallel$, $c_{\perp,\parallel} = c_0 \left(\frac{D_{\perp,\parallel}}{D_0}\right)^2$

Declassified and Approved For Release 2013/03/01 : CIA-RDP10-02196R000300100002-9

The results obtained in [11] can be applied to widely spaced channel lattices, where the interference between channels is negligible. However, it can be shown that the correction for longitudinal leakage depends very slightly on the interference between channels. The allowance for interference involves addition of the terms $\sim B_{\parallel}^4$ with small numerical coefficients.

With an allowance for relationships (6) and the correction for the channel length, expression (3) assumes the following form:

$$\alpha = v\Sigma_a + D_{\perp}B_{\perp}^2 + D_{\parallel}B_{\parallel}^2 - \frac{C_0}{D_0^2}(D_{\perp}B_{\perp}^2 + D_{\parallel}B_{\parallel}^2)^2 - GB_{\parallel}^3. \quad (8)$$

The present paper provides the results of investigations of neutron diffusion in blocks with channel lattices, performed by means of the pulse method. The correction for the channel length and relationships (4)-(6) for the diffusion cooling coefficients were used in processing the experimental results. Moreover, the experimental results from [8] were processed in a similar manner.

EXPERIMENTAL ARRANGEMENT

We used $10 \times 10 \times 5$-cm briquets of sintered beryllium oxide with a mean density of 2.80 g/cm^3, prepared by cold pressing with subsequent calcination, and $4 \times 4 \times 4$-cm beryllium briquets with a mean density of 1.79 g/cm^3, prepared by means of the powder metallurgy method. The briquets were combined into parallelepiped blocks of different sizes, so that square lattices of channels with square cross sections were obtained (Fig. 2 and Table 2). In certain lattices, the side surfaces of blocks were not flat so that their transverse dimensions were determined with respect to their base areas.

The nuclear diffusion parameters of beryllium and beryllium oxide that were used were measured earlier [12], also by means of the pulse method. For beryllium, they were $(v\Sigma_a)_0 = 261.3 \pm 6.9$ sec^{-1}; $D_0 = (1.233 \pm 0.007) \cdot 10^5$ cm^2/sec; $C_0 = (3.13 \pm 0.08) \cdot 10^5$ cm^4/sec; $\lambda = 1.49$ cm. For beryllium oxide, $(v\Sigma_a)_0 = 185 \pm 5.8$ sec^{-1}; $D_0 = (1.548 \pm 0.009) \cdot 10^5$ cm^2/sec; $C_0 = (4.63 \pm 0.24) \cdot 10^5$ cm^4/sec; $\lambda = 1.87$ cm.

The blocks with channels were placed in the beam of the linear electron accelerator in the large experimental room of the Institute of Atomic Energy. They were covered on all sides with 0.5-1.0-mm sheet cadmium and 5-g/cm^2 boron carbide. The measurement conditions and the equipment were the same as in [12].

DISCUSSION OF RESULTS

The typical decay in time of the neutron density in the blocks consisted of the sum of an exponential (with insignificant additions of higher harmonics during the initial period) and a weak background, produced basically by delayed neutrons from the accelerator's plutonium target. The background was virtually absent when a portable neutron source was used. The decay in the blocks did not deviate from an exponential behavior.

The results of counting rate measurements with respect to the analyzer channels were processed by means of a computer, using the method of least squares [19] and the well-known procedure of successive rejection of the initial points of the decay curve for a reliable separation of the fundamental harmonic. The decay constants α thus obtained for different lattice blocks are given in Table 2. The errors $\Delta\alpha$ always amounted to approximately 0.7%. These errors were estimated on the basis of repeated measurements of α for blocks assembled at different times. These measurements were justified by the fact that the errors foreseen by the program [19] were incorrect and apparently had lower values. In Table 2, the extrapolated additions $2 \cdot 0.71\lambda_{\perp} = 1.72 \cdot 10^{-3} D_{\perp}$ along the x and y axes and $2 \cdot 0.71\lambda_{\parallel} = 1.72 \cdot 10^{-3} D_{\parallel}$ along the z axis have been accounted for (during the iteration process) in the geometric parameters B^2.

The diffusion parameters were determined from the measured decay constants α for each anisotropic medium by successive iterations according to the method of least squares [19], while the values of α_i had weights inversely proportional to the squares of their errors $\Delta\alpha_i$. For the first medium (blocks of beryllium oxide; see Table 2), we used a) relationships (3) and (4) and introduced corrections for the finite channel length (7) (first line in Table 3); b) relationships (3)-(5) and (7) (second line); c) relationships (3), (4), (6) and (7) (third line). The value of $v\Sigma_a$ was determined by calculation, using data for the continuous medium. For the other four media (beryllium blocks), we used only the relationships indicated in items b and c (the first and second lines, respectively). The measurements for these media should be considered as tentative, performed in order to confirm the feasibility of determining the diffusion coefficients of anisotropic media from measurements with a small number of blocks. The parameters obtained are given in Table 3. The theoretical values of $D_{\parallel}/D_0$ and $D_{\perp}/D_0$ in this table were obtained by means of Behren's equations [10]:

TABLE 4. Comparison between the Diffusion Parameters Obtained in [8] without Correction for Finite Channel Length (First lines for all media) and our Parameters, Obtained with Respect to the Values of α from [8] by Using the Correction (the next three lines)

Medium	Anisotropic medium	Channel radius R		Lattice spacing a		Ratio p of cavity volume to solid material volume	$c\Sigma_a$, sec^{-1}	$D_\perp \cdot 10^{-3}$, cm^2/sec		$D_\parallel \cdot 10^{-3}$, cm^2/sec		Experiment		Remark
		cm	R/λ	cm	a/λ			experiment	calculation (Benoist)	experiment	calculation	$C_\perp \cdot 10^{-5}$, cm^4/sec	$C_\parallel \cdot 10^{-5}$, cm^4/sec	
1	Square lattice of empty cylindrical channels in graphite	7,0	2,8	20,0	8,0	0,6251	54,63	418,0±5,0	410,65	664,0±8,0	725,42	230,0±40,0	700,0±50,0	$C_\times = C_\perp + C_\parallel$;
								411,3±7,6		718,3±12,8		266,5±55,8	412,1±116,1	$C_\times = C_\perp + C_\parallel$;
								406,8±5,2		738,2±5,1		220,6±44,7	726,4	$C_\times = C_\perp + C_\parallel$, $C_\parallel = C_\times \left(\frac{D_\parallel}{D_\perp}\right)^2$;
								397,4±2,1		712,8±4,0		--	—	$C_\times = C_\perp + C_\parallel$, $C_{\perp,\parallel} = C_0 \left(\frac{D_{\perp,\parallel}}{D_0}\right)^2$
2	Same	5,5	2,2	20,0	8,0	0,3144	63,33	312,0±3,0	308,81	439,0±5,0	469,56	120,0±20,0	300,0±40,0	$C_\times = C_\perp + C_\parallel$;
								308,6±5,5		458,9±8,3		122,2±40,7	174,8±66,5	$C_\times = C_\perp + C_\parallel$;
								307,2±3,8		464,2±3,2		109,7±32,6	250,5	$C_\times = C_\perp + C_\parallel$, $C_\parallel = C_\perp \left(\frac{D_\parallel}{D_\perp}\right)^2$;
								304,2±1,6		466,1±2,6		—	—	$C_\times = C_\perp + C_\parallel$, $C_{\perp,\parallel} = C_0 \left(\frac{D_{\perp,\parallel}}{D_0}\right)^2$
3	"	4,5	1,8	20,0	8,0	0.189	67,91	269,0±2,0	268,09	341,0±4,0	356,91	80,0±20,0	160,0±30,0	$C_\times = C_\perp + C_\parallel$;
								267,3±4,5		352,6±6,9		81,67±35,1	130,9±54,8	$C_\times = C_\perp + C_\parallel$;
								267,5±3,3		352,9±2,6		82,48±28,2	122,4	$C_\times = C_\perp + C_\parallel$, $C_\parallel = C_\perp \left(\frac{D_\parallel}{D_\perp}\right)^2$;
								265,2±1,4		348,9±2,1		—	—	$C_\times = C_\perp + C_\parallel$, $C_{\perp,\parallel} = C_0 \left(\frac{D_{\perp,\parallel}}{D_0}\right)^2$

Declassified and Approved For Release 2013/03/01 : CIA-RDP10-02196R000300100002-9

$$\frac{D_\kappa}{D_0} = 1 + \frac{p}{1+p}\left[1 + \frac{R}{\lambda} q_\kappa + p \frac{\left(\frac{2R}{p\lambda}\right)}{\exp\left(\frac{2R}{p\lambda}\right) - 1}\right], \quad (9)$$

(where $q_\perp = 3/4\ \bar{l}^2/\bar{l}^2 = 1.115$; $q_\parallel = 3/2\ \bar{l}^2/\bar{l}^2 = 2.23$; and $\bar{l}$ is the mean chord of the cavity), and also by means of Carter's equations [13]:

$$\frac{D_\perp}{D_0} = 1 + \frac{p}{1+p}\left(1 + \frac{R}{\lambda} \frac{1 + 2p + \frac{p\lambda}{2R}}{1 + \frac{1}{2}p + \frac{R}{\lambda}}\right). \quad (10)$$

The Benoist equation from [14] can be reduced to Carter's equation (10) by suitable transformations.

It is evident from Table 3 that the experimental data are in agreement with the calculation results. All the 43 experimental points (see Fig. 3) pertaining to medium 1 (beryllium-oxide blocks) lie with an accuracy of ~1% on the second-order surface defined by Eqs. (3) and (4), whose parameters are indicated in Table 3. Each parameter is derived by averaging a set of parameters obtained by successive rejection of 10 experimental points α_i on the side of large B^2 values. With such rejection, the parameters are stable, displaying random fluctuations in either direction from the mean values.

The correction for the finite channel length in the media investigated hardly affects the value of $D_\perp$ (it is reduced by 0.2-1.5%) and considerably augments $D_\parallel$: by 1% for medium 1; by 3% for medium 2; by 9% for medium 3; by 4.5% for medium 4; and by 2% for medium 5. The experimentally obtained diffusion cooling coefficients have the correct sign, but the measurement accuracy is apparently insufficient to determine them reliably.

The correction for the finite channel length results in better agreement between theoretical and experimental values (especially for $D_\parallel$) for large-diameter channels. This is evident from Table 4, which provides the experimental data from [8] for lattices of empty channels with radii of 7.0, 5.5, and 4.5 cm in graphite (first lines). They were obtained by processing the measured decay constants α by means of a special, time-consuming method. It was necessary to reject a considerable number of points on the side of large B^2 values (11 points for R = 7.0 cm, eight points for R = 5.5 cm, and four points for R = 4.5 cm), since the parameters were unstable and varied monotonically with successive omissions of α_i. The next three lines provide our data, obtained by using the method of least squares [19] and relationships (3), (4), and (7); (3)-(5), (7), and (3); (4), (6), and (7), respectively. All the values of α_i measured in [8] were used for each medium; the parameters were stable with regard to the omissions of α_i on the side of large B^2 values and varied within the limits of error in either direction from the mean values indicated on the table (obtained from sets of 10 parameters). The thus obtained parameters (second line) are also given in Fig. 1 (white points); they show excellent agreement between the theoretical and experimental data for all channel radii.

These measurements show that the method of a pulsed neutron source ensures good accuracy in measuring the neutron diffusion parameters in anisotropic media consisting of hollow channels in moderator blocks with finite dimensions. In determining the diffusion coefficients $D_\perp$ and $D_\parallel$, it is necessary to introduce a correction for the longitudinal leakage, which takes into account the finite channel length. For our and other experimental data, correction (7) provides excellent agreement between the experimental and theoretical results; even for large cavities, such as channels with a diameter of 15 cm and a spacing of 20 cm in graphite.

The use of relationships (4)-(6) for the diffusion cooling coefficients yields good results and also simplifies the processing of experimental data.

The author is indebted to M. I. Pevzner* and the staff operating the linear accelerator for the opportunity to complete this project and to N. I. Laletin for the valuable discussions.

LITERATURE CITED

1. M. Capic et al., Nucl. Sci. Engng., 19, 74 (1964).
2. E. Utzinger, W. Heer, and H. Zutz, Proc. of the Symposium on Pulsed Neutron Research, Vol. 2, IAEA, Vienna (1965), p. 137.

*Deceased.

3. R. Page, J. Nucl. Energy, 21, 403 (1967).
4. L. Bennet, Trans. Amer. Nucl. Soc., 10, 281 (1967).
5. B. Joshi, Nucleonik, 10, 323 (1968).
6. I. F. Zhezherun, At. Énerg., 24, 28 (1968).
7. S. Bull, Trans. Amer. Nucl. Soc., 11, 296 (1968).
8. V. Deniz, J. Le Ho, and M. Sagot, Nucl. Sci. Engng., 32, 201 (1968).
9. G. Dardell, Trans. Roy. Inst. Technol., N75, Stockholm (1954).
10. D. Behrens, Proc. Phys. Soc., A62, 607 (1949).
11. N. I. Laletin, At. Énerg., 7, 18 (1959).
12. I. F. Zhezherun, At. Énerg., 14, 193 (1961); At. Énerg. 16, 224 (1964); Proc. of the Symposium on Neutron Thermalization and Reactor Spectra, Vol. 2, IAEA, Vienna (1968), p. 499.
13. C. Carter, J. Nucl. Energy, A15, 76 (1965).
14. P. Benoist, Nucl. Sci. Engng., 34, 285 (1968).
15. P. Benoist, A General Formation of the Diffusion Coefficient in a Heterogeneous Medium which may Contain Cavities, Report AERE-Trans. 842 (SPN 522).
16. A. V. Stepanov, Preprint No. 10, FIAN, Moscow (1969).
17. N. I. Laletin, At. Énerg., 32, No. 4 (1972).
18. N. Laletin, Proc. of the Second United Nations Inter. Conf. on the Peaceful Uses of Atomic Energy, Vol. 16, Geneva (1958), p. 601.
19. I. N. Salin, Preprint No. 11-3362, OIYaI, Dubna (1967).

ABSTRACTS

URANIUM EXTRACTION FROM LOW-GRADE SILICATE ORE WITH THE AID OF THIOBACTERIA

E. G. Kuznetsova and I. P. Kuligina

UDC 546.791:669.822.3

Uranium may be extracted from low-grade silicate ore constituting the residue of radiometric grading (30-mm class) by means of thiobacteria, provided that pyrite or ferrous sulfate is added and that air has access to the mass of ore. The extraction (leaching) of the uranium is accelerated if the ore is wetted (sprayed) with acidified Leten solution.

When 3 to 5% pyrite is added to the ore and the ore is wetted with Leten solution (without ferrous sulfate) acidified to pH = 2.0, 80% of the uranium is extracted in 80 days. Extending the leaching time to 3.5 months increases extraction to 97.8%.

On treating the ore with Leten solution having an iron concentration of 10 g/liter and pH = 2.0, 83.1% of the uranium is extracted in 69 days. The ferrous sulfate can be oxidized to ferric sulfate, with the aid of Thiobacillus ferrooxidans bacteria, and then used for leaching. This accelerates the dissolution of uranium at the start of the process, without affecting the final results.

There is no need to introduce these bacteria specially into the ore prior to leaching, since the bacteria already present in the ore will multiply rapidly in response to the wetting and aeration. The addition of bacteria would only accelerate the onset of the leaching process.

Virtually no uranium at all is leached out when pyrite is added to the ore under sterile conditions with no bacteria present. When ferrous sulfate is added to the material being leached, however, the process takes place even in the absence of bacteria (as a result of partial chemical oxidation of the iron), but the uranium extraction levels are considerably lower (by about 20%) than under otherwise similar conditions with bacteria present. When the ore is treated with sulfuric acid (bringing the pH of the ore pulp to 1.8-2.0), the uranium is leached out at the same rate either under sterile conditions or in the presence of bacteria, but the extraction level still remains 24-30% below that obtained when acidification is accompanied by the simultaneous introduction of the iron compounds referred to earlier.

The use of more acid solutions to wet the ore reduces the amount of iron required.

The experiments were conducted at temperatures 25-27°C and at a solid–liquid ratio of 1:2.0 to 1:2.5.

Translated from Atomnaya Énergiya, Vol. 32, No. 2, p. 153, February, 1972. Original article submitted May 13, 1971; abstract submitted November 8, 1971; final revision submitted September 8, 1971.

EFFECT OF NOISE CURRENTS ON MEASURING CIRCUITS OF REACTOR CONTROL SYSTEMS

A. G. Ivanov and V. M. Matyukhin

UDC 621.039.564.2

A procedure for estimating the effect of noise on shielded cable of nuclear reactor control systems is described; the procedure is based on the use of distributed-parameter electrical circuits. The real terminal impedances of the cables are made equal to three types of loads in this procedure: to a matched load ($z \approx z_0$, where z_0 is the cable characteristic impedance), an open-circuit load ($z \gg z_0$), and a short-circuit load ($z \ll z_0$).

Analytical formulas were derived for several typical cable terminations which make it possible to estimate the noise at the instrument input, if the type of cable, the cable grounding arrangement, and the magnitude of the loads are known. For example, when the shield of a matched cable is grounded only at the instrument picking up the signal, the noise current level at the instrument input can be calculated on the basis of the formula

$$i_{\text{noise}} = j \frac{u_g z_s l^2}{8 z_0 z_{g\text{-}s}} \left[\frac{l^2\beta^2 + 1}{l^2\beta^2} \operatorname{tg} \beta l - \frac{1}{\beta l} \right],$$

where u_g is the average noise voltage over a "meter of ground" along the cable-laying path; z_s is the resistance of the cable shield connection; $z_{g\text{-}s}$ is the characteristic impedance of the ground-to-shield circuit; l is the length of the cable; β is the phase coefficient; j is the imaginary-number unit.

Analysis of the formulas derived, as confirmed by experimental investigations, showed that a cable 100 m in length and matched to the load becomes sensitive to the noise of frequencies below 200 kHz. Cable shortened at one and open at the other end is only slightly sensitive to noise at low frequencies, but features resonance peaks at frequencies above 200 kHz. Noise at frequencies lying in the resonance region arrives virtually unhindered at the input of the instruments.

Reliance on this procedure under concrete conditions has made it possible to determine proper technical measures for shielding and noiseproofing control systems of nuclear reactors to eliminate effects of noise currents. It has been shown, specifically, that symmetrical LC-filters and RC-filters should be placed across the inputs of the instruments in order to protect low-frequency measurement cables from noise currents, and the shields of the connecting cables should be grounded at one point.

The following options are available for shielding high-sensitivity broad-band measuring channels from noise currents: using shields with a low coupling impedance, increasing the characteristic impedance of the ground-to-shield circuit, coil (lumped) loading of the cable, or insulating the measuring channel from the ground.

Translated from Atomnaya Énergiya, Vol. 32, No. 2, pp. 153-154, February, 1972. Original article submitted February 8, 1971; abstract submitted August 2, 1971.

HEAT EXCHANGE CRISIS IN THE BOILING-UP OF LIQUIDS

A. N. Vasil'ev and P. L. Kirillov

UDC 621.039.553.34

Certain technological devices and equipment are cooled by a liquid flowing at a high velocity through channels (nuclear reactor cores, high-power radar systems, transmitting electron tubes, etc.). Considerable overheating of the liquid boundary layer can occur with large thermal loads. The temperature of the cooled surface can be much higher than the saturation temperature even if, on the average, the liquid is not heated to the saturation point; however, the boiling is suppressed in spite of this.

Because of the intensive overheating of the liquid boundary layer, the vapor bubbles grow at a considerable rate in boiling, which can produce a vapor lock in the channel and, thus, reversal of circulation and damage.

The experiments were performed by using water, ethyl alcohol, and Freon-113 in 1Kh18N10T-steel pipes with diameters of 0.64-5.16 mm and lengths of 120-1465 mm at velocities of 0.2-40 m/sec and outlet pressures of 0.28-1.0 atm abs. The method is described in [1].

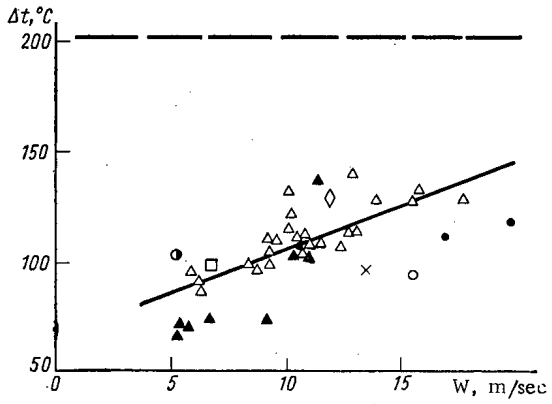

Fig. 1. Experimental dependences of the maximum water overheating on the velocity (p = 1 atm abs.; the curve of maximum overheating is shown at the top).

Notation	Capillary diameter, mm	Length of heated section, mm	Inlet temperature of the liquid, °C
△	4,0×3,0	210	20
●	3,0×1,96	210	20
◇	4,0×3,0	270	20
□	4,0×3,0	331	20
○	3,0×1,96	331	20
▲	1,98×0,96	210	60
◑	1,53×1,2	210	60
×	4,0×3,0	210	60

Two sets of conditions were observed. In one of them, there was intensive overheating of the wall (see Fig. 1), and the crisis occurred due to the abrupt boiling-up of the liquid in the channel. The other set of conditions was characterized by surface boiling.

The wall temperature distributions (first set of conditions) are in satisfactory agreement with the theoretical results based on the equations of convective heat exchange for a single-phase flow [2-4] for any ratio of the wall temperature to the saturation temperature. This constitutes one of the proofs of the absence of boiling under such conditions. The other proofs of this are the absence of wall temperature fluctuations, continuous readings of the electric probe in the flow, the absence of the pressure fluctuations characteristic for surface boiling, which was confirmed by tensometry, the absence of deposits on the wall in using the "salt method," and visual observations.

The condition for the onset of the heat exchange crisis is obtained in the first approximation by equating the growth rate of the vapor lock to the mean velocity of the liquid. Subsequent transformations yield the following equation, which generalizes the data from our investigations:

$$q_{cr} = 1.04 \cdot 10^5 p_{cr} \left(\sqrt{W^3} \frac{d}{\sqrt{l}} \right)^{0.8}$$

Translated from Atomnaya Energiya, Vol. 32, No. 2, pp. 154-155, February, 1972. Original article submitted March 16, 1971.

LITERATURE CITED

1. A. N. Vasil'ev and P. L. Kirillov, in: Problems in the Heat Physics of Nuclear Reactors [in Russian], Atomizdat, Moscow (1969), p. 49.
2. S. S. Kutateldze, Fundamentals of the Heat Exchange Theory [in Russian], Nauka, Novosibirsk (1970).
3. B. S. Petukhov, Teplofizika Vysokikh Temperatur, 1, 85 (1963).
4. V. P. Skripov, Heat and Mass Exchange [in Russian], Vol. 2, Izd. AN BSSR, Minsk (1962), p. 60.

AN APPROXIMATE METHOD FOR CALCULATING FAST NEUTRON SHIELDS

B. S. Sychev

UDC 621.039.538

The calculation of shields against neutrons produced in the operation of proton synchrotons presents certain difficulties because of the complex geometry of the radiation source and shield. We propose to determine the fast neutron flux density outside a shield from the expression

$$\Phi(x, \theta, R) = \gamma f(\theta) \frac{I_p}{R^2} e^{-\frac{x}{\lambda}} B\left(\frac{x}{\lambda}, E_0, \theta\right), \quad (1)$$

where I_p is the number of protons per second interacting with a target in the acceleration channel, R is the distance from the target to the point of observation, θ is the angle with the proton beam at the target position, $f(\theta)$ is the angular distribution of neutrons leaving the target, x is the shield thickness along the line connecting the point of observation and the target, γ is the neutron multiplication factor in the accelerator assembly ($\gamma = 1$ for a single target), λ is the inelastic neutron interaction from free path, and $B(x/\lambda, E_0, \theta)$ is the buildup factor for the neutron flux.

If the beam is lost in the accelerator chamber it is necessary to replace I_p by the specific linear losses of protons and to integrate Eq. (1) over the length of the extended source.

The validity of Eq. (1) is confirmed by the experiments on the attenuation of the radiation dose rate in the longitudinal shield of the Brookhaven 30 GeV proton synchroton [1] (Fig. 1). The detectors were placed along radial directions in the plane of the ring at various distances from the target along the beam axis. Estimates show that the semiempirical method described is applicable for angles $\theta > 30°$.

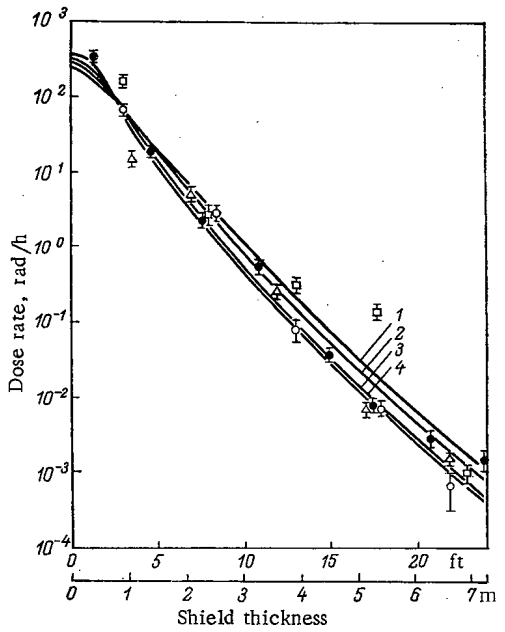

Fig. 1. Attenuation of absorbed dose rate in the side shield of a proton synchrotron at various distances r from the target. The intensity of the proton beam is 10^{12} protons/sec. Experiment. Values of r(m): □, 8.4; ●, 9.4; ○, 18; △, 15.7. Calculation. Values of r(m): 1) 6; 2) 10; 3) 14; 4) 16.

LITERATURE CITED

1. W. Casey et al., Nucl. Instrum. and Methods, 55, 253 (1967).

Translated from Atomnaya Énergiya, Vol. 32, No. 2, p. 155, February, 1972. Original article submitted June 24, 1971.

A UNIVERSAL EXPRESSION FOR THE CHARACTERISTICS OF THE SCATTERED ELECTRON DISTRIBUTION AS A FUNCTION OF THE MEDIUM AND THE INITIAL ELECTRON PARAMETERS

V. V. Arutyunov, V. F. Baranov, and A. G. Zrazhun

UDC 539.171.2

Monoenergetic electrons with energies E_0 from 0.2 to 5 MeV are incident on aluminum and tissue-equivalent barriers and on a semiinfinite absorber. Monte Carlo calculations of the differential and integral characteristics of the scattered electron distribution show certain regularities. The angle of incidence of the electrons θ_0 varies from 0 to 75°. The thickness of the absorber d varies from 0.1 R_0 to 0.8 R_0, where R_0 is the maximum range of electrons of energy E_0.

When electrons with energies from 0.4 to 5 MeV are incident normally on aluminum or tissue-equivalent (z = 7.2) barriers the angular distribution of transmitted electrons can be described to within ±10% by the expression

$$\psi(d, \theta) = \psi(d, 0°) \exp\left\{-\left[\frac{\theta(1+0.012E_0)}{\theta_{1/e}}\right]^2\right\} \cos\theta, \quad (1)$$

where $\psi(d, \theta)$ and $\psi(d, 0)$ are respectively the numbers of electrons emerging from a unit area of the barrier per unit time per unit solid angle at angles θ and 0 with the normal. The values of $\theta_{1/2}$ do not depend on the value of the primary energy E_0 for aluminum or tissue-equivalent barrier thicknesses in the range d/R_0 = 0.1-0.7. The angle $\theta_{1/2}$ varies from 31.3° to 68.6° and from 22.5° to 68.6° respectively.

The energy distributions of electrons with primary energies up to 1 MeV and from 2 to 5 MeV can be described to within ±20% by two different universal functions.

For primary electron energies up to 5 MeV the average energy $\bar{E}$ of the electrons beyond an aluminum or tissue-equivalent barrier is independent of the angle of incidence between 0 and 60° and can be described within ±20% by the relation

$$\bar{E}/E_0 = 1 - c\frac{d}{R_0}, \quad (2)$$

where c = 1.1-0.15 (d/R_0) for tissue-equivalent material and 1.2-0.15 (d/R_0) for aluminum.

The absorbed dose rate P_2 per electron incident on the surface of a semiinfinite aluminum absorber of thickness $0.1 \leq d/R_0 \leq 0.65$ can be determined from the relation

$$P_2 = 1{,}6 \cdot 10^{-8}(ax^2 + bx + c)\ \text{rad/sec}, \quad (3)$$

where $x = d/R_0$.

The relation between the values of the absorbed dose rates in aluminum for slab (P_1) and (P_2) geometries is given by

$$P_2 = mP_1. \quad (4)$$

The quantities *a*, b, c, and m take on different values depending on the energy of the primary electrons and their angle of incidence on the aluminum barrier.

Translated from Atomnaya Energiya, Vol. 32, No. 2, p. 156, February, 1972. Original article submitted May 11, 1971.

CALCULATION OF BREMSSTRAHLUNG INTENSITY BY THE MONTE CARLO METHOD*

V. V. Arutyunov and V. F. Baranov

UDC 539.125.5.348

An algorithm is presented for using the Monte Carlo method to calculate the spectral density of bremsstrahlung produced by a broad beam of electrons incident on the surface of an absorber. The electron trajectories in a barrier are assumed to consist of segments of length equal to the thickness of the Moller layer of the material, satisfying the Moller theory. The energy of the gamma photon emitted by the electron along each segment is chosen by lottery using the simple approximate expressions for the bremsstrahlung across sections obtained by the authors. The angle between the emitted gamma photon and the direction of motion of the electron before penetrating the layer is assumed equal to the electron scattering angle as determined by the Moller theory. The history of the gamma photon is traced with a probability determined by using the approximate expressions mentioned above, but for the Compton interaction of the photon. When the energy of the gamma photon reaches 50 keV it is assumed that both the photon and the electron are absorbed.

By using this model the spectral intensities of the bremsstrahlung behind aluminum barriers up to 3 g/cm^2 thick was calculated. The electron energies were varied from 0.2 to 5 MeV and their angles of incidence from 0 to 75°.

Calculated bremsstrahlung intensity spectra behind aluminum barriers of various thicknesses are presented for primary electron energies of 0.5, 1, and 3 MeV. Within the limits of experimental error (±20%) there is good agreement between the measured and calculated values.

Values of the bremsstrahlung efficiency (the fraction of the primary energy transformed into bremsstrahlung) are presented for monoenergetic electrons incident at various angles on an aluminum barrier.

The good agreement between the calculated and experimental data shows the reliability of the method for calculating the bremsstrahlung intensity for the range of primary electron energies considered.

DOSIMETRIC CHARACTERISTICS OF NEUTRON THRESHOLD DETECTORS†

T. V. Koroleva, K. K. Koshaeva, and S. N. Kraitor

UDC 539.12.08:539.1.074.88

We consider the measurement of neutron dose by using a set of threshold detectors consisting of U^{235}, U^{235} + Cd, U^{235} + 1 g/cm^2 B^{10}, Np^{137}, U^{238}, and S^{32} which had been selected to measure neutron spectra [1].

*Translated from Atomnaya Énergiya, Vol. 32, No. 2, pp. 156-157, February, 1972. Original article submitted May 11, 1971.

†Translated from Atomnaya Énergiya, Vol. 32, No. 2, p. 157, February, 1972. Original article submitted June 23, 1971.

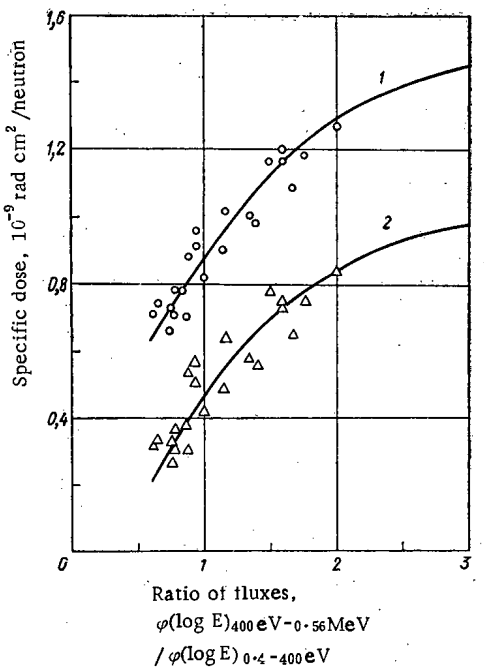

Fig. 1. Specific surface dose (1 and ○) and neutron kerma (2 and △) in the 400 eV-0.56 MeV range as functions of the ratio of differential neutron fluxes.

The average values of the specific dosimetric magnitudes are calculated in the energy ranges 0.01-0.4 eV, 0.4-400 eV, 400 eV-0.56 MeV, 0.56-1.4 MeV, 1.4-2.8 MeV, and 2.8-10 MeV. It is shown that above 0.56 MeV their spread does not exceed 4%. In the 400 eV-0.56 MeV range it amounts to 60%, which limits the accuracy of the measurements.

A method is proposed for calculating the specific neutron dose in the 400 eV-0.56 MeV range and for obtaining its dependence on the ratio of the fluxes in the 400 eV-0.56 MeV and 0.4-400 eV ranges which are obtained directly from the detector readings. For the surface dose and kerma it is shown by the solid curves in Fig. 1 and agrees with calculations using existing data on neutron spectra (circles and triangles). The spread of the specific dose determined this way does not exceed 13% for spectra harder than the Fermi spectrum.

The dose composition of the neutrons in the extracted beam and in the OIYaI IBR reactor room has been found by using the set of threshold detectors and the proposed methods of calculation.

LITERATURE CITED

1. K. K. Koshaeva, S. N. Kraitor, and L. B. Pikel'ner, Preprint OIYaI, PE-5421 (1970).

LETTERS TO THE EDITOR

SHORT-TERM REACTOR COOLING

S. O. Slesarevskii, M. N. Korotenko,
M. M. Nazarchuk, D. T. Pilipets,
and S. S. Stel'makh

UDC 621.039.517.5

The work described here was carried out on the VVR-M reactor of the Nuclear Research Institute of the Academy of Sciences of the Ukrainian SSR [IYaF AN UkrSSR], and constitutes an extension of research work on reactor temperature fields under both steady-state and transient operating conditions [1]. A specified number of chromel/copel microthermocouples was bonded to each component part of the fuel element. The thermocouple junction was held to the surface of the fuel element by a round tab of pure aluminum (thickness 0.1 mm, diameter 2 mm), after which the aluminum tab was welded on its perimeter to the wall of the fuel element, by using a TKM-4 capacitor-bank welding machine.

The thermocouple leads were bonded to the fuel element along its length by a similar process of welding an elongated (2 × 5 mm) aluminum tab to the fuel element. The thermocouple junctions were offset 4-5 mm from the thermocouple leads, so that a portion of the thermocouple leads would lie on a curve close to the isotherm. Figure 1 shows the thermocouples were allocated over the height of the fuel element and special-purpose measuring rod.

The temperature was recorded with the aid of N373/2 automatic recorders and the R307 recording potentiometer in tandem with a M 195/2 type null-indicating device. Errors introduced by the measuring instruments were taken into account in processing the results of the measurements, as well as the thermocouple calibration error, changes in contact thermal resistance and in the amount of heat carried off via the thermocouple leads, etc. The effect of reactor irradiation on thermocouple readings was determined by making comparisons with a control thermocouple. The total probable error in the measurements was found to be equal to one degree, when all the component errors were duly taken into account.

One of the basic conditions encountered in reactor operation is absence of water boiling in the core under either normal operating conditions or emergency conditions.

We made an earlier study of the temperature distribution in the core when the VVR-M was shut down instantaneously from several different power levels (all the way up to 10 MW) with simultaneous stoppage of coolant circulation. The experiments showed that the peak coolant temperature does not attain the level of the boiling point, in agreement with data reported in [2, 3]. This means that, at least for the VVR-M reactor, we can relax the requirement that standby cooling equipment be brought immediately into play in any emergency.

This paper is devoted to a study of the temperature distribution pattern after short-term cooling of the reactor core. The reactor had been operating at a level of 10 MW for 120 h prior to the shutdown. The temperature was continuously monitored from the instant the shutdown went into effect. The core was cooled down in the space of 15 to 20 min, with the aid of three primary-loop pumps (coolant flowrate 1420 m^3/h), and also in 15 min through the action of a single primary-loop pump (flowrate 470 m^3/h). The most unfavorable conditions were encountered in the latter case (Fig. 2a, 2b). The temperature distribution over the length of the fuel element and the distribution of the coolant temperature over the height of the reactor tank during the cooling process are shown in Fig. 2a, while Fig. 2b displays the temperature distributions after short-term cooling.

A stepwise increase in the temperature occurs at the instant when the coolant circulation is cut off (see Fig. 2b). We also observe some temperature pulsations of alternating sign which are maximized at

Translated from Atomnaya Énergiya, Vol. 32, No. 2, pp. 159-160, February, 1972. Original article submitted January 13, 1971.

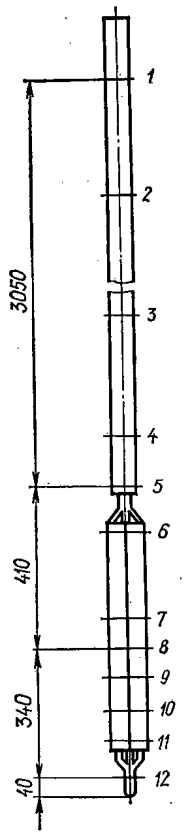

Fig. 1

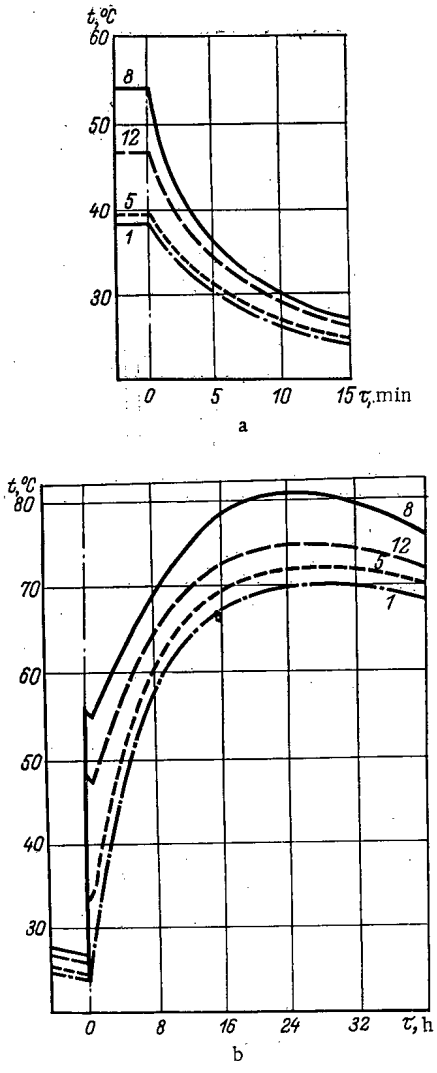

Fig. 2

Fig. 1. Location of thermocouples with respect to height of fuel element and measuring rod (numerals distinguish thermocouples).

Fig. 2. Temperature variation in reactor shutdown: a) in cooling by a single primary-loop circulation pump; b) after cooling for 15 min by natural circulation; -.-.-.-.-) thermocouple No. 1; - - - - -) thermocouple No. 5; ———) thermocouple No. 8; - - - - -) thermocouple No. 12.

the fuel-element wall. It must be stressed, nonetheless, that such phenomena, while smaller in absolute magnitude, are also observed after long-term cooling of the core (4 hours).

The temperature jumps are not identical over the height of the tank, and are determined both by the amount of heat accumulated in the reactor structure and by the rate of residual heat evolution. The greatest temperature increment was recorded on the wall of the fuel element (thermocouple No. 8). After thermal equilibrium had become established between the entire reactor structure and the surroundings, the temperature declined smoothly.

It is clear from analysis of the experimental results that a reactor shutdown with simultaneous shutoff of coolant circulation is a safe operation from the standpoint of heat transfer physics. But under ordinary reactor shutdown conditions there are steep temperature peaks to content with, and the relatively high coolant

temperature renders this operating regime severely rigid. Experiments on long-term cooldown (4-5 h) have shown convincingly that reactor shutdowns of this type are uneconomical. Experiments on short-term reactor cooldown (15-20 min) indicate the possibility of shortening reactor cooldown time, since the level of temperatures in the shut-down reactor differs only insignificantly in that case from the level of temperatures attained in reactor shut-down with long-term cooldown.

LITERATURE CITED

1. M. V. Pasechnik et al., III Geneva International Conference on the Peaceful Uses of Atomic Energy P/165 (1964).
2. H. Bobin et al., Nucl. Engng., 8, 439 (1963).
3. I. Aleksandrowicz et al., Institute of Nuclear Research, Report No. 1170/1XA/PR, Warszawa (1970).

FAST NEUTRON FLUXES IN EXPERIMENTAL CHANNELS OF THE MR REACTOR

A. V. Borodin, V. I. Vikhrov,
V. F. Krasnoshtanov, V. N. Perevezentsev,
and G. E. Shatalov

UDC 539.125.5

We present the results of determining fast neutron fluxes and spectra in the material-testing and loop channels of the MR reactor [1]. The fast neutron fluxes were determined by normalizing the spectrum calculated by the Monte Carlo method by means of the threshold reactions

$$In^{115}(n, n')In^{115m},\ Fe^{54}(n, p)Mn^{54},$$
$$Ti^{46}(n, p)Sc^{46},\ Mg^{24}(n, p)Na^{24},\ Al^{27}(n, \alpha)Na^{24}.$$

The Monte Carlo calculation of fast neutron spectra used a program for the M-20 computer which permitted the calculation of the flux in a cylindrical reactor without taking account of inelastic scattering and resonance absorption of neutrons; the scattering was assumed isotropic in the center of mass system.

The reactor can be described in two ways in the calculation. In the first way the reactor is represented by 10 coaxial regions each of homogeneous composition. The neutron sources in the regions are specified on the surfaces of cylinders of arbitrary radius with arbitrary longitudinal distributions. In the second way homogeneous channels are located arbitrarily in the homogeneous moderating material of the reactor. All but one of the channels are identical in composition. The neutron sources are specified in the channels with arbitrary transverse and longitudinal distributions. In this description the reactor can have a side reflector.

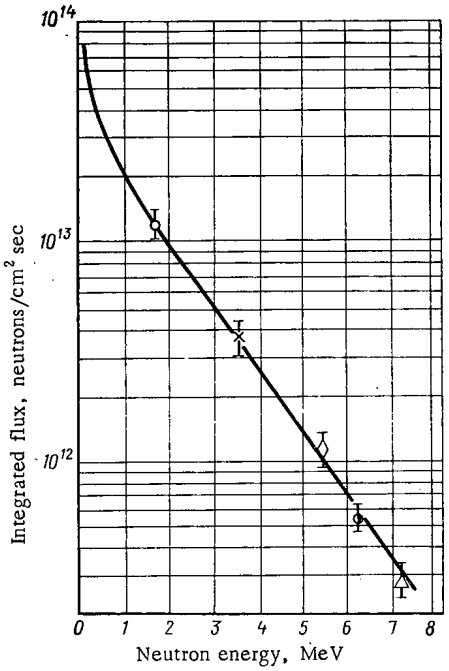

Fig. 1. Fast neutron energy spectrum in a material-testing channel: ○) In^{115} (n, n') In^{115m}; ×) Fe^{54} (n, p) Mn^{54}; ◇) Ti^{46} (n, p) Sc^{46}; ◐) Mg^{24} (n, p) Na^{24}; △) Al^{27} (n, α) Na^{24}.

This program can be used to compute the fast neutron spectrum in material-testing channels and in loop channels of complex composition and geometry. A statistical accuracy of ~10% was achieved in recording neutrons in 10-16 energy groups in the 0.1-10 MeV range.

The technique of exposing and measuring threshold detectors is described in [2, 3].

The fast neutron energy spectrum in one of the material-testing channels of the MR reactor is shown in Fig. 1. The points represent the experimental values of the fluxes obtained with threshold detectors; the solid curve is the calculated spectrum normalized to the experimental points.

The determination of the neutron spectrum in the loop channels of the reactor where the fuel elements are tested is of practical importance. The structural features of the reactor do not permit the determination of the fast neutron flux with special detectors.

Translated from Atomnaya Énergiya, Vol. 32, No. 2, p. 161, February, 1972. Original article submitted May 6, 1971.

The fluxes in the loop channels were determined by normalizing the calculated spectral shape by using the $Fe^{54}(n, p) Mn^{54}$ threshold reaction. The reaction occurs in the iron of the fuel element cladding.

In conclusion it should be noted that the methods described for determining fast neutron fluxes and spectra are used successfully in practice in irradiating materials in the MR reactor.

LITERATURE CITED

1. W. Goncharov et al., Proc. of the III International Conference on the Peaceful Uses of Atomic Energy, Vol. 7, New York (1965), p. 314.
2. V. I. Vikhrov and N. F. Pravdyuk in: Dosimetry of Large Doses [in Russian], FAN, Tashkent (1966), p. 100.
3. N. F. Pravdyuk et al., ibid, p. 111.

HEAT-TRANSFER PROPERTIES OF CERMET COMPOSITIONS OF THE SYSTEM Al_2O_3 – Mo

V. A. Osipova and Kh. A. Kyaar

UDC 536.21:223.621.762

The work described in this article is a continuation of research begun earlier [1] which has contributed to determinations of the heat-transfer properties of cermet compositions 80% Al_2O_3 + 20% Mo and 60% Al_2O_3 + 40% Mo (wt. %) at temperatures 500-1300°K. Aluminum oxide (alumina) serves as the initial powder constituent in the ceramic component. The chemical composition of the molybdenum powder is cited below (wt. %):

Mo	W	Ta	Nb	Ti	Zr
99,91	0,046	0,03	0,01	0,03	0,03

Dispersion analysis revealed that 90% of the initial powder consists of particles sized 0.001 mm to 0.003 mm, and 10% consists of particles sized 0.005 mm to 0.01 mm. The average density of the 80% Al_2O_3 + 20% Mo specimen is 4450 kg/m^3, and the average density of the 60% Al_2O_3 + 40% Mo specimen is 5120 kg/m^3. The overall porosity of the cermet compositions fell within the range 1-4%. The experimental specimens were prepared by sintering, and their diameter was 40 mm, height ≈ 70 mm. The specimens were assembled from separate disks 5 to 10 mm thick.

The complex dynamic method of monotonic heating was the basis for the investigations of the heat-transfer properties. This method enabled us to find the complex of heat-transfer parameters (λ, a, c_p) over the entire range of heating temperatures by staging a single experiment. The high-temperature vacuum arrangement has been described in an earlier article [2]. Another variant of the experimental arrangement is discussed elsewhere [3].

The heat flux is measured by the standard-body method. The specific heat standard is a specimen consisting of the spectrally pure α-modification of aluminum oxide. The automatic control system that was developed keeps the heat flux constant over the surface of the test specimen. The control process is monitored on an ÉPP-09 recorder strip chart. The maximum deviation from the temperature set point over the interval investigated remained within 5°K.

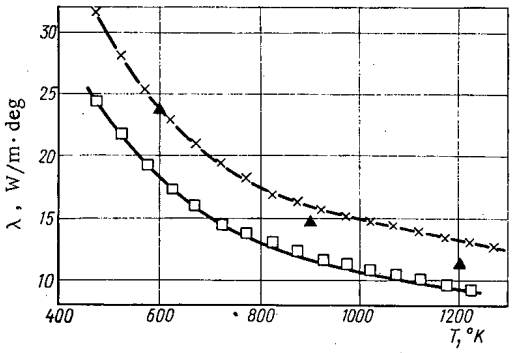

Fig. 1. Thermal conductivity of cermet compositions: □) 80% Al_2O_3 + 20% Mo; ×) 60% Al_2O_3 + 40% Mo; ▲) theoretically predicted data [4].

Chromel-alumel thermocouples 0.2 mm and 0.3 mm in diameter, and VR5/VR20 tungsten–rhenium thermocouples 0.2 mm in diameter, were employed in the experiment. The thermocouples were selected beforehand by the criterion of matching the thermoelectric characteristics for measuring the temperature drop and the time lag. Since the specimens act as electrical insulators over the range of temperatures investigated, the temperature drop over the radius of the experimental specimen is measured by a differential circuit. During a single experiment 50-60 experimental points were obtained. The results were then averaged

Translated from Atomnaya Énergiya, Vol. 32, No. 2, pp. 162-163, February, 1972. Original article submitted January 20, 1971; final revision submitted July 8, 1971.

TABLE 1. Thermal Conductivity λ(W/m · °K) and Thermal Diffusivity a ($\times 10^6/m^2/sec$) of Cermet Compositions

T°, K	80% Al_2O_3 + 20% Mo		60% Al_2O_3 + 40% Mo	
	λ	a	λ	a
473	24,5	6,8	31,8	10,5
573	19,4	5,0	25,3	6,8
673	15,9	3,9	21,0	5,4
773	13,8	3,2	18,3	4,6
873	12,2	2,8	16,4	4,1
973	11,1	2,5	15,2	3,7
1073	10,1	2,3	14,5	3,3
1173	9,5	2,1	13,4	3,1
1273	—	—	12,8	2,9

graphically. The maximum relative error in the results was 11% in determinations of thermal conductivity, and 7% in determinations of thermal diffusivity. The experiments were carried out at a constant heat flux density of 8000 W/m^2 over the temperature range from 500° to 1300°K. The results of the measurements appear in Table 1 and in Fig. 1. The temperature dependence of the thermal diffusivity is similar to the te mperature dependence of the thermal conductivity.

In the diagram, the experimental data for the composition 60% Al_2O_3 + 40% Mo are compared to the dependence obtained by computational means for the matrix system [4]. Microstructural analysis of the specimens showed that the aluminum oxide is a matrix in which molybdenum particles become imbedded. Reliable data [5] on the thermal conductivity of aluminum oxide and on the thermal conductivity of molybdenum [5-7] were obtained on the basis of these calculations.

LITERATURE CITED

1. V. A. Osipova and M. I. Pak, At. Énerg., 26, 72 (1969).
2. M. I. Pak and V. A. Osipova, Teploénergetika, No. 12, 68 (1966); Teploénergetika, No. 6, 63 (1967).
3. V. A. Osipova, Experimental Investigation of Heat Transfer Processes [in Russian], Énergiya, Moscow (1969).
4. V. I. Odolevskii, Zh. Tekh. Fiz., 21, 667 (1951).
5. Thermophysical Properties of High-Temperature Solid Materials, New York–London (1967).
6. A. Agte and I. Vacek, Tungsten and Molybdenum [in Russian translation], Énergiya, Moscow (1964).
7. I. N. Makarenko, L. N. Trukhanova, and L. P. Filippov, Teplofiz. Vis. Temp., 8, 445 (1970).

CARBON ELECTROTRANSFERENCE IN BERYLLIUM

V. P. Gladkov, V. S. Zotov, and M. D. Skorov

UDC 539.125.525

The study of electrotransference of impurity elements in solid metals is helpful in obtaining several important characteristics of materials. For example, direct current can be passed through a beryllium specimen during zone refining to enhance the effectiveness of carbon removal from the specimen [1]. The authors in question account for the result, true enough, in terms of the combined effect of electrotransference and the Peltier effect tending to render the temperature gradient steeper in the molten zone.

This led to a study of carbon electrotransference in solid beryllium with a hexagonal-close-packed lattice. Polycrystalline powdered beryllium metal with an average grain size of 56 μ was used in the investigations. The impurity content, according to chemical analysis data, was (in wt. %): oxygen 0.15, carbon 0.06, aluminum 0.05, iron 0.1, silicon 0.07, chromium 0.02, copper 0.03, manganese 0.02, nickel 0.015, magnesium 0.002.

The end faces of the specimens (specimen diameter 0.5 cm, length 0.6 cm) were polished and then coated with a suspension of elemental carbon C^{14} in tsaponlak [a nitrocellulose varnish]. Pairs of such specimens combined on their active sides were clamped between beryllium current leads and placed in a vacuum chamber ($\approx 10^{-4}$ torr) to be annealed. Direct current (current density 508 A/cm^2) was passed through the specimens during the anneal.

The test specimens were heated to the working temperatures by an externally placed heater, and the experimental temperature was monitored by a Pt – Pt + 10% Rh thermocouple to within ± 5°C. After annealing, the anode and cathode parts of the pair of specimens were analyzed layer by layer, using a T-25-BFL counter (mica window diameter 25 mm, mica thickness 1.0 mg/cm^2). The analysis revealed a dependence characterizing the carbon distribution in depth through the specimens.

The amount of carbon applied to the end faces of the specimens brought about boundary conditions corresponding to diffusion from a "constant source."

The equation for diffusion from the constant source into the field of the constraining force assumes the form

$$\frac{\partial c(x, t)}{\partial t} = D\frac{\partial^2 c(x, t)}{\partial x^2} \pm \vartheta \frac{\partial c(x, t)}{\partial x}; \tag{1}$$

$$\left.\begin{array}{l} c(0, t) = c_0, \quad t > 0; \\ c(x, 0) = 0, \quad x \geqslant 0; \\ c(\infty, t) = 0, \end{array}\right\}, \tag{2}$$

where c(x, t) is the concentration of the diffusant; D is the diffusion coefficient, which is independent of the concentration; ϑ is the directed rate of displacement of material in response to the constraining force; c_0 is the constant concentration corresponding to the limit of solubility of the investigated impurity in the metal. In the general case, the solution of Eq. (1) with the boundary conditions (2) acquires the form [2]:

$$c(x, 0) = \frac{c_0}{2}\exp\left(\frac{\vartheta}{D}x\right)\left[\operatorname{erfc}\left(\frac{x+\vartheta t}{2\sqrt{Dt}}\right) + \exp\left(-\frac{\vartheta}{D}x\right)\operatorname{erfc}\left(\frac{x-\vartheta t}{2\sqrt{Dt}}\right)\right]. \tag{3}$$

Upon changing direction, the concentration fields in the semiinfinite spaces are related by the formula

Translated from Atomnaya Énergiya, Vol. 32, No. 2, pp. 163-164, February, 1972. Original article submitted April 9, 1971.

TABLE 1. Carbon Electrotransference in Beryllium

Experimental temperature, °K	ρ, $\mu\Omega \cdot$ cm [5]	D, cm^2/sec	$\vartheta \cdot 10^{-3}$ cm/sec	Mobility U, (cm/h)/(V/cm)	z^*
1473±4	46,0	$1,3 \cdot 10^{-9}$	2,34	$2,02 \cdot 10^{-4}$	—0,254
1373±5	41,5	$2,2 \cdot 10^{-9}$	2,49	$3,48 \cdot 10^{-4}$	—0,164
1273	37,5	$2,0 \cdot 10^{-10}$	2,56	$2,71 \cdot 10^{-6}$	—26,5

$$c(x, t)_+ = c(x, t) - \exp\left(\frac{\vartheta}{D} x\right), \quad (4)$$

where $c(x, t)_+$ and $c(x, t)_-$ are the concentrations in the anodic and cathodic parts of the specimens respectively.

In order to calculate the effective charge, we can make use of the equation [3]

$$z^* = \alpha \frac{kT}{ej\rho} \cdot \frac{\vartheta}{D}, \quad (5)$$

where k and e are the Boltzmann constant and the charge on the electron; j is the current density; ρ is the electrical resistivity of the specimen; α is a coefficient accounting for the crystalline structure of the metal ($\alpha = 0.78$ [4]). The ratio ϑ/D was computed on the basis of Eq. (4).

Results of measurements of carbon electrotransference in beryllium at the three temperatures are given in Table 1.

Electrotransference of carbon toward the anode takes place at the selected temperatures, so that the effective charge on the carbon in the beryllium is negative. The electrotransference is brought about by the interaction between the electric field and electrically charged activated atoms and by entrainment of atoms by the moving electrons as a result of elastic collisions. The formula for the effective charge therefore incorporates both the parameters of the diffusing impurity (diffusant) and the characteristics of the conduction electrons [6]:

$$z^* = z_i + nle\sigma_i, \quad (6)$$

where z_i is the coulombic charge on the atom; n is the density of conduction electrons; l is the electron path length; σ_i is the scattering cross section of the impurity atom. It is unfortunately not possible to carry out the calculations completely on the basis of Eq. (6).

In the approximation of a two-zone model of a solid, the effective charge is related to the temperature [7] as:

$$z^* = z_i + \frac{b}{T + \rho_0/\alpha}, \quad (7)$$

where ρ_0 and α are the parameters of the temperature dependence of the resistivity, and b is a constant. An estimate of z_i based on Eq. (7) yields $z_i = -233$ (1273-1473°K) and $z_i = -2$ (1373-1473°K). The value of the intrinsic charge (−233) clearly lacks any physical meaning, and the approximation resorted to is invalid in this range of temperatures. But in the temperature range 1373-1473°K, the charge on the carbon diffusing through the beryllium has an entirely acceptable significance. Negative ionization of the carbon atoms must result in an increase in the dimensions of those atoms, so that the view that carbon forms interstitial solid solutions with beryllium is hardly tenable [5].

Results of a study of electrotransference in 25 binary systems have been analyzed [8]. Findings were that the mobilities and the migration mechanism are interrelated, so that U = 0.01 to 7.2 (cm/h)/(V/cm) in the case of interstitial impurities, and $U = 3 \cdot 10^{-4}$ to $1.5 \cdot 10^{-3}$ (cm/h)/(V/cm) in the case of substitutional impurities. In our work, we arrived at the value $U \approx 10^{-4}$ or lower values (see Table 1). Carbon in beryllium is in all likelihood a substitutional impurity, according to the evidence.

We can draw the following inferences from the foregoing discussion:

1) carbon electrotransference in polycrystalline beryllium of grain size 56 μ was studied in our work;

2) the effective charges in the beryllium were determined at 1273, 1373, and 1473°K, and found to be respectively −26.5, −0.154, and −0.264;

3) in the approximation of the two-zone model of a solid, we calculated the intrinsic charge on the carbon diffusing through the beryllium ($z_i = -2$ over the 1373-1473°K interval);

4) it is assumed that substitutional solid solutions are capable of existing in the system beryllium–carbon.

LITERATURE CITED

1. V. N. Grinyuk et al., Izv. Akad. Nauk SSSR, Metally, 4, 77 (1967).
2. B. I. Boltaks, Diffusion in Semiconductors [in Russian], Fizmatgiz, Moscow (1961).

3. W. Sait, Diffusion in Metals [Russian translation], Izd-vo Inostr. Lit., Moscow (1958).
4. P. P. Kuz'menko, and G. P. Grinevich, in: Diffusion Processes in Metals [in Russian], Kiev (1968), p. 5.
5. I. I. Papirov and G. F. Tikhinskii, Physical Metallurgy of Beryllium [in Russian], Izd-vo AN SSSR, Moscow (1968).
6. V. B. Fiks, Ionic Conduction in Metals and Semiconductors [in Russian], Fizmatgiz, Moscow (1969).
7. D. F. Kalinovich et al., Fiz. Tverd. Tela, 10, No. 8, 1480 (1968).
8. J. Verhoeven, J. Metals, 26, 1 (1966).

THERMODYNAMICS OF THE EXTRACTION OF PLUTONIUM (IV) FROM PERCHLORIC AND NITRIC ACID SOLUTIONS IN THE PRESENCE OF OXALIC ACID

A. S. Solovkin and A. I. Ivantsov

UDC 66.061.9:546.799.4

As was shown by an analysis of the literature [1] and our own data, performed according to the methods of [2-4], the extraction of Pu (IV) from nitric acid media by solutions of 2-thenoyltrifluoroacetone (HA) in C_6H_6 is described by the equations

$$Pu^{4+}\ (aq) + 4HA\ (org) \rightleftarrows PuA_4\ (org) + 4H^+\ (aq),$$

$$Pu(OH)^{3+}\ (aq) + 3HA\ (org) \rightleftarrows Pu(OH)A_3(org) + 3H^+\ (aq),$$

while extraction from perchloric acid media is also described by the equation

$$Pu^{4+}\ (aq) + ClO_4^-\ (aq) + 3HA\ (org) \rightleftarrows Pu(ClO_4)A_3\ (org) + 3H^+\ (aq).$$

In accord with this, the dependence of the distribution coefficient on the composition of the aqueous and organic phases is expressed by the equation

$$D = \frac{a_{HA}^3}{a_{H^+}^3}\left(K_0^0 \frac{M'_{Pu^{4+}}\gamma_{Pu^{4+}}a_{HA}}{a_{H^+}} + K^0_{ClO_4}M'_{Pu^{4+}}\gamma_{Pu^{4+}}a_{ClO_4} + K^0_{OH}M'_{Pu(OH)^{3+}}\gamma_{Pu(OH)^{3+}}\right). \quad (1)$$

where a_i and γ_i are the activities and activity coefficients of the corresponding ions and molecules; M'_i represents the fractions of i ions in the aqueous phase; K_0^0, K^0_{OH}, and $K^0_{ClO_4}$ are the thermodynamic equilibrium constants of the reactions indicated above.

From a comparison of the experimental and calculated values of D it follows (Table 1) that Eq. (1) permits a satisfactory description of the distribution of Pu (IV) in a broad range of compositions of the aqueous and organic phases.

TABLE 1. Extraction of Pu (IV) by Solutions of HA in C_6H_6 ($K_0^0 = 4 \cdot 10^6$, $K^0_{ClO_4} = 3.5 \cdot 10^6$, $K^0_{OH} = 2.2 \cdot 10^7$)

Concentration, M				D	
HNO_3	$LiNO_3$	$HClO_4$	HA	experiment	calculation
0,471	—	—	0,0129	1,08	1,3
0,471	—	—	0,015	2,26	2,08
0,471	—	—	0,0172	3,59	3,27
0,5 *	—	1,5	0,05	0,35	0,38
1,56†	3,5	—	0,19	1,54	1,61
4,91‡	—	—	0,19	0,044	0,046

*$\gamma_{Pu^{4+}} = 0.021$, $\gamma_{Pu(OH)^{3+}} = 0.039$.

†$\gamma_{Pu^{4+}} = 0.12$, $\gamma_{Pu(OH)^{3+}} = 0.125$, $\gamma_{H^+} = 7.0$, $M'_{Pu(OH)^{3+}} = 0.03$.

‡γ_i is correspondingly equal to 0.155, 0.152 and 3.74, $M'_{Pu(OH)^{3+}} = 0.014$.

When oxalic acid is introduced into the system, the distribution coefficient of Pu (IV) is reduced, and moreover, as was indicated by a statistical analysis of the experimental data, the formation of a complex ion inextractable by HA proceeds according to the only possible reaction

$$Pu(OH)^{3+} + H_2C_2O_4 \rightleftarrows Pu(OH)C_2O_4^+ + 2H^+.$$

In the calculation of the quantity

$$\beta^0_{H_2C_2O_4} = \frac{[Pu(OH)C_2O_4^+]a_{H^+}^2}{[Pu(OH)^{3+}]\gamma_{Pu(OH)^{3+}}[H_2C_2O_4]} = 2{,}4 \cdot 10^7$$

it was assumed that $\gamma_{Pu(OH)C_2O_4^+}/\gamma_{H_2C_2O_4} = N \approx \text{const}$. Since the experimental values of D correspond satisfactorily to the calculated values both in extraction with HA (Table 2) and with TBP (Table 3) in a broad interval of compositions of the aqueous phase, it is evident that $N \approx \text{const}$.

Translated from Atomnaya Énergiya, Vol. 32, No. 2, pp. 164-166, February, 1972. Original article submitted June 1, 1971.

TABLE 2. Extraction of Pu (IV) by a 0.05 M solution of HA in C_6H_6 in the Presence of $H_2C_2O_4$

Concentration, M			D	
HNO_3	$HClO_4$	$H_2C_2O_4 \cdot 10^3$	experiment	calculation
2,0	...	0,8	0,042	0,043
2,0	—	1,6	0,027	0,024
2,0	—	8,0	0,0055	0,0055
0,1	1,9	0,8	0,142	0,138
0,1	1,9	1,6	0,079	0,080
0,1	1,9	4,0	0,037	0,035
0,1	1,9	8,0	0,013	0,018

TABLE 3. Extraction of Pu (IV) by a Solution of TBP (20% by volume) in Decane in the Presence of $H_2C_2O_4$

Concentration, M		D	
HNO_3	$H_2C_2O_4 \cdot 10^3$	experiment	calculation
2,0	22,4	0,068	0,063
2,0	33,6	0,038	0,041
4,0	5,6	6,25	6,55
4,0	11,2	4,0	4,0
4,0	22,4	2,25	2,22
4,0	44,8	1,20	1,05
4,0	78,4	0,6	0,7

In the presence of $H_2C_2O_4$ the values of D were calculated using the equation

$$[Pu(OH)C_2O_4^+] = \frac{\beta^0_{H_2C_2O_4}[Pu(OH)^{3+}]\gamma_{Pu(OH)^{3+}}[H_2C_2O_4]}{a^2_{H^+}[Pu^{4+}]}.$$

The calculation of all the necessary parameters in the extraction of Pu (IV) by HA and TBP was performed according to the methods described in [2-5].

It is interesting to note that the mechanism of the extraction of Pu (IV) by HA from perchloric acid media does not differ from the mechanism found for zirconium, [4], i.e., in both cases compounds of the same composition MA_4 and $M(ClO_4)A_3$ are formed in the organic phase. Moreover, Pu (IV) is extracted from nitric acid in the form of PuA_4 and $Pu(OH)A_3$, whereas zirconium is extracted in the form of ZrA_4 and $Zr(NO_3)A_3$. The change in the mechanism of the extraction of plutonium in comparison with zirconium from perchloric to nitric acid solutions can be explained as follows.

The high electrostatic characteristics of the Zr^{4+} ion leads to the fact that as we go from perchloric acid to nitric acid solutions, the hydrate shell of the Zr^{4+}_{aq} ion does not undergo any structural changes, and the structure of the hydrate shell promotes the insertion both of a ClO_4^- ion and of a NO_3^- ion (to a lesser degree, see [4]) into the extractable HA complex. In contrast to this, the structure of the hydrate shell of the Pu^{4+}_{aq} ion changes from perchloric to nitric acid solutions. Although in perchloric acid solutions it is close to the structure of the Zr^{4+}_{aq} ion, which is indicated by the insertion of the ClO_4^- anion into the extractable complex, in nitric acid media the change in the structure of the hydrate shell of the Pu^{4+}_{aq} ion is such as to prevent insertion of the NO_3^- anion into the extractable complex. The change in the structure of the hydrate shells of quadruply charged cations of the actinide elements with changing composition of the aqueous phase has been demonstrated for U^{4+}_{aq} [6-8] and Np^{4+}_{aq} [8, 9] ions. It is natural to assume that the tendency for a change in the structure of the hydrate shell of M^{4+}_{aq} ions will increase in the series $Pu^{4+}_{aq} < Np^{4+}_{aq} < U^{4+}_{aq} < Th^{4+}_{aq}$.

LITERATURE CITED

1. Plutonium. Handbook [in Russian], Atomizdat, Moscow (1971).
2. A. S. Solovkin, Zh. Neorgan. Khim., 15, 1914 (1970).
3. A. S. Solovkin, At. Énerg., 30, 545 (1971).
4. A. S. Solovkin and A. I. Ivantsov, Zh. Neorgan. Khim., 16, 22 (1971).
5. A. S. Solovkin, Salting Out and the Quantities Description of Extraction Equilibria [in Russian], Atomizdat, Moscow (1969).
6. A. S. Solovkin, Zh. Neorgan. Khim., 14, 1124 (1969).
7. A. G. Rykov and V. Ya. Vasil'ev, Radiokhimiya, 12, 714 (1970).
8. V. Ya. Vasil'ev, Dissertation [in Russian], NIIAR, Melekess (1970).
9. A. G. Rykov and N. B. Blokhin, Radiokhimiya, 12, 717 (1971).

SIMULATION EXPERIMENT ON THE WATER – OIL CONTACT IN EXPLORATION OF STRATAL FRESH WATER BY RECORDING DELAYED NEUTRONS

Ya. E. Kostyu, A. P. Osipenko, and V. A. Shkoda-Ul'yanov

UDC 543.53

Work on developing procedures for breaking the water – oil contact surface in wells with slightly mineralized or fresh stratal waters is acknowledged high priority. Results of a preliminary experiment and estimate calculations reported by some authors [1, 2] attest to the possibility, in principle, of delimiting water-saturated and oil-saturated strata in rock under these conditions, by making use of the reaction O_8^{18} (γ, p) N_7^{17}. The results of the investigations described below, carried out with a simulated well, confirm the basic conclusions arrived at by these authors. The model simulating the oil well was a metal tank 160 × 120 × 80 cm. The cased well hole was simulated by a steel column and cement rings. The tank was divided into two compartments, filled with crude petroleum and water or with mixtures (sand – water and sand – petroluem, the porosity of the sand being ≈ 21%). Standard equipment (two independent channels) was utilized in the measurements. SNM-11 neutron counters, as radiation detectors, were encased in paraffin (to simulate a filled well) and were inserted in a steel tube (column) at the same distances from the γ-ray beam, which passed through the strata at right angles to the axis of the well hole. The intensity of the betatron emission was ≈ 10 to 15 R/min per meter while the measurements were being taken.

The filled compartments of the tanks, i.e., the simulated "strata," were irradiated to the point of complete saturation of N_7^{17} activity (approximately six half-lives). After 100 msec had elapsed after the beam of γ-photons had been switched off, both counting channels automatically went into operation and the delayed neutrons formed in the strata as a result of the reaction O_8^{18} (γ, p) N_7^{17} ($\beta^-/T_{1/2}$ = 4.15 sec) $O_8^{17} \rightarrow O_8^{16} + n$ were recorded.

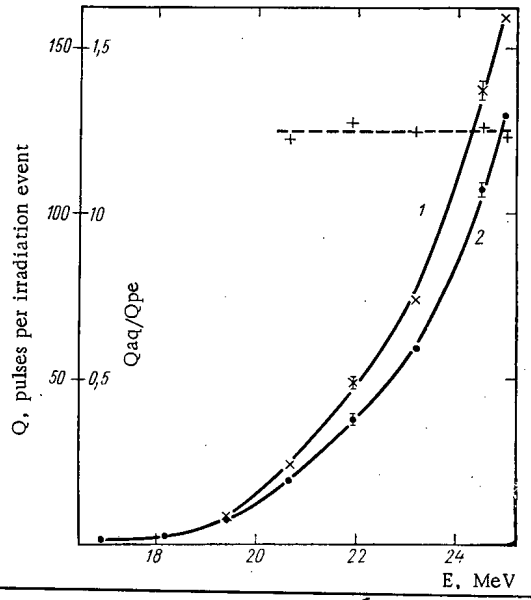

Fig. 1. Yield of delayed neutrons per irradiation event from aquiferous (1) and petroliferous (2) strata as a function of the energy of the incident γ-radiation (broken line indicates ratio of yields of delayed neutrons).

Translated from Atomnaya Énergiya, Vol. 32, No. 2, pp. 166-167, February, 1972. Original article submitted February 15, 1971; final revision submitted August 9, 1971.

TABLE 1

E, MeV	Q_{dn} (from water) / Q_{dn} (from petroleum)
21,22	5,59 (30 cm); 4,04 (20 cm); 3,66 (10 cm)
21,72	6,74 (30 cm)
21,99	7,32 (30 cm)

TABLE 2

Q_{ac}/Q_{pt}	Distance from water – oil surface, cm	Q_{ac}/Q_{pt}	Distance from water – oil surface, cm
1,27	40	1,24	20
1,30	30	1,17	10

Table 1 lists ratios of yields of delayed neutrons (Q_{dn}) as a function of the energies of the bombarding γ-photons obtained during the measurements when the compartments were filled with water and with crude petroleum (without the cement rings in place, but with an iron tube) (the parentheses indicate the distances from the baffle separating the two compartments at which the middle of the γ-ray beam entered the water or petrol petroleum).

The effect of cement rings, which is related to the presence of oxygen in the cement, to attenuation of the intensity of the γ-ray beam as it passes through the cement ring, and also the to removal of the delayed-neutron detectors from the "effective volume," was studied in the course of the experiments. The compartments were filled with water and petroleum alternately in the measurements, with and without a simulated casing string fitted onto the cement ring. Information on the effect of the cement ring can be obtained from the ratio of the delayed-neutron yields measured with the cement ring in place and without it. The ratio of the delayed-neutron yields against water and petroleum when the cement rings were used was 1.73, as against 6.33 without the cement rings. The 1.73 values can be increased if the energy and intensity of the bombarding γ-photons are increased.

Measurements pertaining to the breaking of the water–oil contact surface were carried out using γ-photons of the maximum energy in the bremsstrahlung spectrum, 23.5 MeV. A total of 10^4 pulses from seven to 10 series of measurements were taken for each point. The resulting yields of ratios of delayed neutrons from the aquiferous stratum (Q_{ac}) and petroliferous stratum (Q_{pt}) are tabulated below (Table 2) as a function of the distance from the water–oil surface to the center of the γ-ray beam.

It is clear from the tabular data that the proposed method is useful in separating the aquiferous and petroliferous strata in cased wells with fresh or slightly mineralized stratal waters. It is worth noting that the method suffers from a limitation imposed by the presence of considerable quantities of chlorine or other neutron absorbers in the stratal water, wherever that is the case.

The efficiency of the detectors along the well axis was ascertained in order to verify any fringe effects. It was found that this efficiency varies only negligibly, so that there is no need to introduce any corrections (the maximum deviation from the average is 2%).

The yields of delayed neutrons from the aquiferous and petroliferous strata were also measured as functions of the γ-photon energy. The results of these measurements appear in Fig. 1. The curves correspond to averaged data of six series of measurements with four to seven values in each series ($\approx 10^3$ pulses in the high-energy region were taken for each data point).

It is clear from Fig. 1 (curve 1 and 2) that the total yield of delayed neutrons from the strata increases with the energy, so that the statistical accuracy of the results can only be enhanced thereby. Whether the profundity of the investigation is improved with increasing energy must be ascertained by performing additional investigations with an unexpanded range of variation in the energy of the bombarding γ-radiation.

Figure 1 also shows the ratio of yields of delayed neutrons against the aquiferous and petroliferous strata. It is clear from these data that the difference in the yields of delayed neutrons in the range from 20.7 to 24.5 MeV amounts to roughly 25% and barely changes at all, so that the ratio of the yields arises directly with the porosity and with the oil-saturation ratio.

Preliminary information on the depth of the investigations carried out by the method proposed were obtained in measurements using a specimen enriched with the isotope O^{18} (50% enrichment, weight 45 g). The specimen was placed in the water-filled compartment at various distances from the casing tube. It was found that the radius of the zone of investigation was roughly 45 cm when the energy of the γ-photons was 21.5 MeV.

In conclusion, the authors express their thanks to colleagues of the department of nuclear physics of the Uzhgorod State University for the kind assistance in carrying out the experiment reported on here, and

also to VNIIYaGG [All-Union Geophysics and Geochemistry Scientific Research Institute] (Moscow) for helpful consultations and for their persistent interest in the progress of the work.

LITERATURE CITED

1. M. M. Dorosh et al., At. Énerg., 21, 35 (1966).
2. A. K. Berzin et al., Inventors' Certificate No. 174284, dated December 9, 1963.

SEPARATION OF LIQUID MIXTURES BY THERMODIFFUSION THROUGH AN ELECTRIC FIELD

V. P. Kuchinov, B. I. Nikolaev, and A. A. Tubin

UDC 621.039.3

The thermodiffusion method of separation offers certain advantages in the production of small quantities of varpor-phase high-enrichment isotopes [1]. Special interest centers on possible applications of thermodiffusion in the separation of isotopes and molecular mixtures in the liquid phase, since the value of the thermodiffusion constant in that case is at least one order of magnitude greater than the corresponding vapor-phase constant [2]. But the theoretically possible separation coefficients are not actually attained in the use of thermodiffusion techniques, because of the inevitable appearance of parasitic mixing flow patterns in the separation column. The effect of these dissipating parasitic flow patterns is particularly pronounced in liquid columns, because of the difficulties in keeping the effective gap constant (within tenths of a millimeter) in such columns over an extended length. Reliance on various techniques for suppressing these parasitic flow patterns (rotation of one of the column cylinders, use of porous packings, perforated baffles, different washers and recesses, etc.) complicates the column design while intensifying the separation process.

The work reported on here involved an experimental investigation of the effect of a constant electric field (as a possible intensification factor) on the process of separating liquid mixtures in thermodiffusion columns. A cylindrical column standing 150 mm high, with a gap 0.665 ± 0.005 mm, and average diameter of transverse cross section of effective gap 20.705 mm, was prepared for the experiment. Tanks 26.7 cm^3 in volume were placed at the ends of the column. The column inner cylinder was cooled with thermostatted

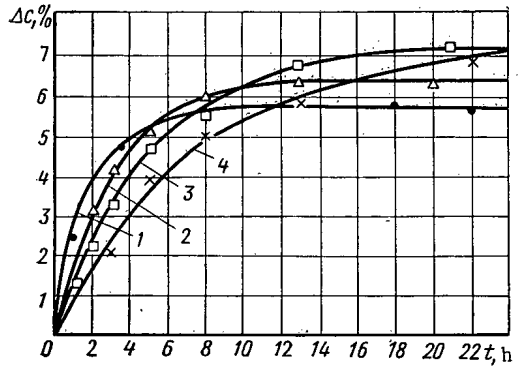

Fig. 1

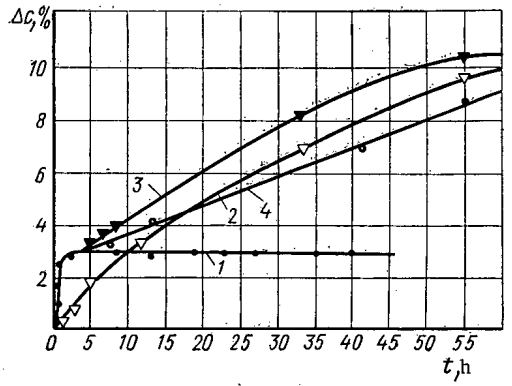

Fig. 2

Fig. 1. Time dependences of difference in concentrations along column length at different electric field strengths: 1) E = 0; 2) E = 15 kV/cm; 3) E = 30 kV/cm; 4) E = 45 kV/cm.

Fig. 2. Time dependences of difference in concentrations over length of modified column, at different electric field strengths: 1) E = 0; 2) E = 25 kV/cm; 3) E = 25 kV/cm; 4) E = 37.5 kV/cm (field imposed at t = 4 h).

Translated from Atomnaya Énergiya, Vol. 32, No. 2, pp. 167-169, February, 1972. Original article submitted June 16, 1971.

water, while the outer was heated by an electric heater unit. The column design and the procedure followed in the measurements are described in detail elsewhere [3]. The inner and outer cylinder were connected to a high-voltage source in order to keep the electric field constant throughout the effective column gap. The systems investigated consisted of equivolume mixtures of nonpolar organic liquids: normal heptane – benzene and normal hexane – cyclohexane.

Figure 1 shows the time dependences of the degree of separation of a normal heptane – benzene mixture at different electric field strengths in the effective gap: here Δc is the difference in the concentrations at the ends of the column (the experiments were conducted at an average temperature $\bar{T} = 10°C$ and at a temperature difference between the walls $\Delta T = 8°C$). It is clear from the diagram that the superposition of the electric field brings about an increase both in the separation of the mixture in the column and in the transient period of the equilibrium state. For example, the equilibrium concentration drop over the length of the column (Δc_{eq}) increases by more than 20% at E = 45 kV/cm over the zero-field level.

Similar dependences were obtained in the separation of a normal hexane – cyclohexane mixture.

The experiments showed that a reversal of the direction of the electric field has no effect on the equilibrium concentration drop or on the transient period of the equilibrium state. This last fact indicates a clear-cut dependence of the separation effect on the intensity of the electric field.

Investigations have shown that appreciable parasitic streams exist in an electrically heated thermodiffusion column; Δc_{eq} increased at a rate of 0.05% per 1°C as the temperature drop across the column effective gap was increased [4]. In order to minimize the effect of parasitic convection on the separation process in the presence of an electric field, the thermodiffusion column was modified: the outer column cylinder was also heated with water supplied from a thermostat. In this modified column, Δc_{eq} increased at a rate of 0.01% per 1°C as ΔT increased. As a consequence of the minimization of the stray flow patterns in the column, the relaxation time of the process (τ) increased to $\tau = 5.85$ h as against $\tau = 2$ h in the case of the electrically heated column.

In order to shorten the transient period of the equilibrium state, the effective gap in the modified column was widened to (0.800 ± 0.005) mm. Investigations were carried out with the column so modified, using a mixture of normal heptane and benzene at $\Delta T = 20°C$ and $\bar{T} = 27°C$. The time dependences $\Delta c = \Delta c(t)$ for different electric field strengths are plotted in Fig. 2.

It is clear from Fig. 2 that a lower value of the equilibrium separation effect is achieved in a shorter time span in the modified thermodiffusion column in the absence of an electric field. Application of an electric field results, as in the former case, in a longer transient period.

The experiments showed that the change in the separation effect in response to application of an electric field of up to 20 kV/cm in intensity falls within the range of error of the measurements. Any further increase in the intensity of the electric field results in an appreciable increase in the degree of separation.

In order to achieve a shorter transient period, the process was staged in the following sequence. The process began with separation in the absence of electric field until an equilibrium state set in, which took two hours; then the electric field was established in the column. As is clearly evident from Fig. 2, this procedure made it possible to save ≈ 6 h in the experiment when a 25 kV/cm field was applied, ≈ 20 h when E = 37.5 kV/cm, and about two full days when E = 50 kV/cm. The modified procedure for the separation process made it possible to achieve the equilibrium state in practice when E = 25 kV/cm. In that case application of the electric field leads to increased separation in the equilibrium state, by a factor of roughly 3.2. The equilibrium state was not attained at E = 37.5 kV/cm, but the general nature of the time dependences demonstrates a further increase in Δc_{eq} as the intensity of the electric field is increased.

Analysis of the results obtained leads to the inference that the use of an electric field in a thermodiffusion column results in suppression of the parasitic flow patterns. There is no doubt, however, that the process of separation of nonpolar mixtures in the thermodiffusion column is affected by phenomena other than those dealt with here (such as electrical convection, changes in the transport coefficients, and so on).

LITERATURE CITED

1. R. Schwind, Chem. Proc. Engng., 50, 75 (1969).
2. K. Alexander, Usp. Fiz. Nauk, 76, 711 (1962).
3. B. I. Nikolaev and A. A. Tubin, Teor. Osnovy Khim. Tekhnol., 4, 432 (1970).
4. R. Ya. Gurevich and G. D. Rabinovich, Inzh.-Fiz. Zh., 19, 809 (1970).

SEPARATION OF ISOTOPES OF NITROGEN AND HYDROGEN IN THE PHOTODISSOCIATION OF AMMONIA

B. U. Utirov, G. M. Panchenkov, V. K. Korovkin, and Yu. G. Basov

UDC 621.039.335

The photochemical method of separation of isotopes is of great interest as a result of the possibility of producing substantial enrichment in the separatory cell. This can occur under the condition that the reaction vessel is irradiated with monochromatic light, exciting molecules with one isotope of the given element, which then reacts with some substance, while the molecules containing the remaining isotopes of the given element do not react with the substance. To provide for such a scheme of separation it was necessary to have a selective radiation source. Since this problem presents considerable technical difficulties from the standpoint of phototechnics, a PRK-2 mercury lamp, possessing only a continuous spectrum of radiation in the region of interest to us, was used to separate isotopes of nitrogen and hydrogen in the photodissociation of NH_3. In this case substantial separatory effects can be achieved in comparison even with electrogas processes, distinguished by high coefficients of separation of isotopes (CSI) [1]. This is possible in the case when the curve characterizing the energy spectrum of the source studied takes a steep form in the region of energies of excitation of the isotopes [2].

The photodissociation of ammonia was conducted on a molybdenum glass circulation apparatus, the principal scheme of which as applied to experiments on the photodissociation of ozone was described in [3]. Before the beginning of the experiments a thermostat was turned on, and the system was evacuated to a pressure of 10^{-2} torr. After the vacuum pump was shut off, purified nitrogen was admitted. Then a circulation pump was turned on, and after 5 min of mixing, the PRK-2 lamp was ignited. At the end of the

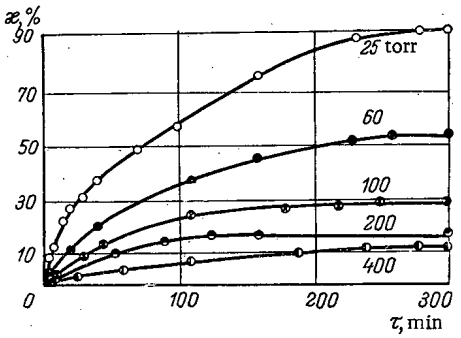

Fig. 1

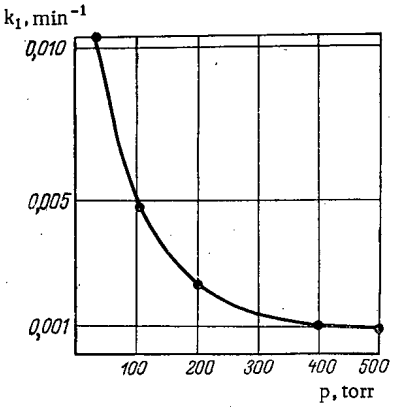

Fig. 2

Fig. 1. Dependence of the degree of decomposition of ammonia on the time of circulation: solid lines – calculation; points – experiments.

Fig. 2. Dependence of the rate constant of the dissociation of ammonia on the pressure at a temperature of the walls of the reactor of 20°C.

Translated from Atomnaya Énergiya, Vol. 32, No. 2, pp. 169-170, February, 1972. Original article submitted March 25, 1971.

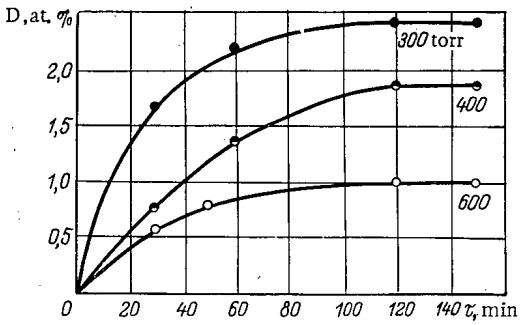

Fig. 3. Dependence of the deuterium content in ammonia on the time of circulation of a hydrogen–ammonia mixture in the process of isotopic exchange under the action of light (temperature of wall 20°C).

experiment the increase in the pressure in the system on account of the dissociation of ammonia was measured (at a constant temperature of the walls of the reactor during the experiment). The kinetics of the decomposition of ammonia was followed according to the change in the pressure in the system. A kinetic study of the process was conducted at temperatures of the walls of the reactors from −20 to 30°C and pressures of 18-600 torr.

Figure 1 presents the dependence of the degree of decomposition of ammonia on the time of circulation of the gas τ. The degree of decomposition of NH_3 at $\tau = 300$ min decreases with increasing initial pressure: from 92.4% at 25 torr to 9.14% at 400 torr. At a pressure of 600 torr the reaction practically does not take place.

To determine the nature of the activation of the decomposition of NH_3 a kinetic analysis was conducted [2]. Figure 2 presents the dependence of the rate constant of the dissociation of ammonia on the pressure at a temperature of the walls of the reactor of 20°C (experimental results). At high pressures the number of collisions leading to association of NH_3 molecules is great, and the rate of the reverse reaction – the rate of formation of ammonia – far exceeds the rate of decomposition of NH_3, as can be seen from Fig. 2.

Samples of ammonia were collected for mass spectrometric isotopic analysis of nitrogen in special ampoules containing 2 ml of frozen 2 N HCl. To study the isotopic effects due to the presence of hydrogen, samples of ammonia enriched with deuterium were preliminarily prepared. For this purpose, purified ammonia and hydrogen enriched with deuterium up to 12.5 atomic %, produced by electrolysis of heavy hydrogen water, were admitted to the evacuated system in definite proportions. Under the action of the light of a mercury lamp, there was an exchange reaction, at the end of which the deuterium-enriched ammonia was frozen out. This ammonia served as the source of gas in experiments studying the redistribution of isotopes of hydrogen in the dissociation of ammonia. Figure 3 presents the time dependence of the deuterium concentration in ammonia on the time of circulation of the hydrogen–ammonia mixture. In 2 h an equilibrium of the process of isotopic exchange was already practically established. Using this method, samples of ammonia enriched with deuterium can be obtained. The hydrogen produced in the thermal decomposition of ammonia on a nickel catalyst at 500-600°C was subjected to mass spectrometric isotopic analysis. In this case the hydrogen of ammonia of the initial composition was compared with that remaining after the cessation of the dissociation of NH_3 under the action of light.

The isotopic composition of nitrogen was determined on an MI-1305 mass spectrometer according to the molecular peaks corresponding to the masses 28 and 29, after conversion of N_2 from ammonia to the free state by a hypobromide method [4].

The CSI in the dissociation of ammonia can be calculated according to the formula

$$\alpha = \frac{X_1}{1-X_1} \Big/ \frac{X_2}{1-X_2}, \qquad (1)$$

where X_1 and X_2 are the atomic fractions of a rare isotope in the residual ammonia and its decomposition products. The isotopic analysis of hydrogen is complicated by the formation of triatomic hydrogen ions in the ion source of the mass spectrometer. To determine the true ratio of the concentrations of HD and H_2 and the linear relationship between the ratio of the ion peaks of these masses and the pressure in the source, in this case we should extrapolate to zero pressure. At low concentrations of deuterium for example, up to 5 at.%, this error is inconsequential.

Our experiments indicated that in the photodissociation of ammonia there is a redistribution of nitrogen isotopes, and the rare isotope of nitrogen N^{15} is concentrated in the undecomposed ammonia with a CSI equal to 1.014 ± 0.01, the value of which does not depend either on the pressure or on the temperature of the walls of the reaction vessel within the limits of the experimental error.

The mechanism of the photodissociation of ammonia under the action of the light of a mercury lamp can be represented in the form [2]:

$$NH_3 + h\nu \rightarrow NH_2(\tilde{x}^2B_1) + H(^2S); \quad (2)$$

$$NH_3 + NH_2(\tilde{x}^2B_1) \rightarrow N_2(^1\Sigma_g^+) + 2H_2 + H(^2S); \quad (3)$$

$$NH_3 + H(^2S) \rightarrow NH_2(\tilde{x}^2B_1) + H_2. \quad (4)$$

We calculated the CSI for these steps according to the formulas cited in [5]. The values of the CSI for reactions of the type of (2), (3), and (4) are 1.0001, 1.015, and 1.0015, respectively. From the calculation it is evident that the basic contribution to the general isotopic effect is made by step (3).

As a result of our experiments studying the isotopic effects in hydrogen, it was established that the CSI, just as for nitrogen, is concentrated in the residue of ammonia, does not depend on the pressure and temperature, and is equal to 1.50 ± 0.04. Analogous calculations for this case indicated that the basic contribution to the isotopic effect with respect to hydrogen is made by step (2).

In the dissociation of NH_3 in an electric discharge, the values of the CSI are 1.43 for hydrogen and 1.006 for nitrogen [6]. Thus, the results of this work confirm the advantages of the photochemical method of preparation even when a light source with a continuous spectrum of radiation is used. The presence of selective indices permits a product with a high concentration of a rare isotope to be obtained comparatively simply and cheaply.

LITERATURE CITED

1. I. A. Semiokhin, Doctoral Dissertation [in Russian], Moscow (1970).
2. B. U. Utirov, Candidate's Dissertation [in Russian], Moscow (1970).
3. B. U. Utirov, G. M. Panchenkov, and V. K. Korovkin, Zh. Fiz. Khimii, 43, 1904 (1969).
4. In: The Production and Use of Labeled Atoms [Russian translation], Izd-vo Inostr. Lit., Moscow (1948), p. 48.
5. Yu. G. Basov, Zh. Fiz. Khimii, 43, 2149 (1969).
6. K. M. Salimova, Candidate's Dissertation [in Russian], Moscow (1969).

OPERATING CHARACTERISTICS OF DISPERSIVE AIR-EQUIVALENT SCINTILLATORS

G. P. Volosyuk, S. P. Vershinina,
O. A. Gunder, L. S. Prokof'eva,
and L. V. Sigalova

UDC 539.1.074.3

We investigated the influence of radiation and temperature effects on the dosimetric characteristics of detectors consisting of a plastic scintillator (PS) with 1/200 part by weight of ZnS(Ag) (luminous compound K-430).

The specimens (diameter 16 mm, height 10 mm) were irradiated on the cobalt apparatus of the Nuclear Physics Institute of the Academy of Sciences of the Uzbek SSR, which had an exposure dose rate of 6,000 R/sec. The investigations showed that the variation of the relative effectiveness of air-equivalent detectors as a function of gamma-ray energy remains constant up to absorption doses of $8 \cdot 10^6$ rad, whereas their light yield decreases (Fig. 1). According to [1], the variation of the relative efficiency of dispersive scintillation detectors as a function of gamma-ray energy is determined by the concentration and relative conversion efficiency of the components. The method used for determining the relative conversion efficiency for the PS and ZnS(Ag) is explained in [1].

On the basis of the experimental data, it was possible to assume that the absorption of light in the base material of the detector increases, while the conversion efficiency values of the components remain practically constant in the gamma-ray dose range investigated. The variation of the relative coefficient of transmission of light through the PS as a function of the absorbed gamma-ray dose was measured by the method proposed in [2]. The irradiated specimens were placed between a photomultiplier and an unirradiated detector of the same composition excited by alpha radiation. In our determination of the relative conversion efficiency of the PS we introduced a correction for the absorption of light in the detector. We assumed that the transmission of light was proportional to the coefficient of light collection of the detector. As can be

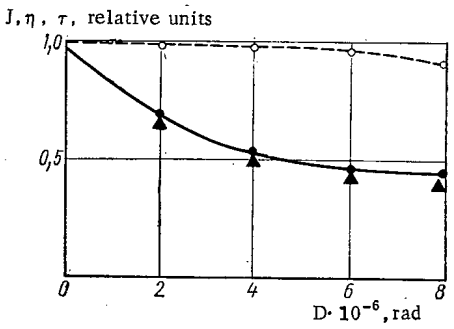

Fig. 1

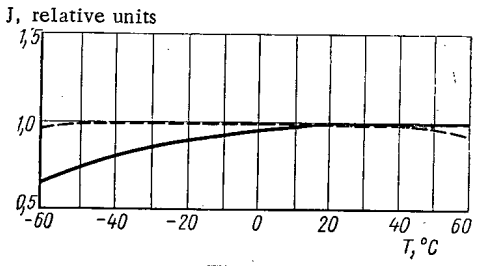

Fig. 2

Fig. 1. Variation of the transmission coefficient τ of the PS, the conversion efficiency η of the PS, and the light yield J of dispersive detectors, as functions of the absorbed gamma-ray dose D: ●) τ; ○) η; ▲) J.

Fig. 2. Light yield of PS and ZnS(Ag) as a function of temperature: - - -) PS; ——) ZnS(Ag).

Translated from Atomnaya Énergiya, Vol. 32, No. 2, pp. 171-172, February, 1972. Original article submitted January 4, 1971.

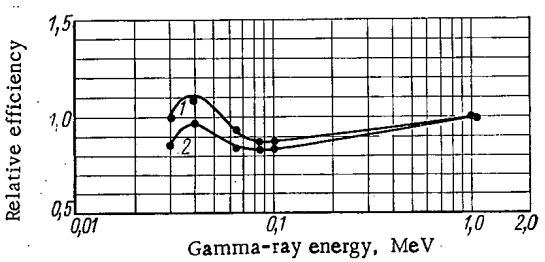

Fig. 3. Variation of relative detector efficiency at different temperatures: 1) 60 and 20°C; 2) −60°C.

seen from Fig. 1, the decrease in the light yield of dispersive detectors measured in current operation is due to the change in the transparency of the PS.

The relative coefficient of light transmission of the PS is halved when a gamma-ray dose of $5 \cdot 10^6$ rad is absorbed. In [2] the same change in the coefficient of light transmission of the PS was obtained for an absorbed gamma-ray dose of $3 \cdot 10^{10}$ rad. The discrepancy may be ascribed to the difference in the thicknesses of the specimens investigated. The thickness of the PS specimens investigated in [2] was 0.5 mm. The conversion efficiency of the ZnS(Ag) for an absorbed dose of $6 \cdot 10^6$ rad did not change. After 50 days of storage in an air medium at normal temperature and pressure and 60% humidity, the characteristics of the detectors under investigation were close to the values for unirradiated specimens.

In order to determine how the dosimetric characteristics of the detectors vary with temperature, we used an apparatus analogous to the one described in [3]. The detector was placed in a massive copper holder, which was cooled with liquid nitrogen or heated. The detector temperature was measured with a copper–constantan thermocouple. Light contact between the light guide and the detector was provided by means of the thermally stable glue. The decrease in the light yield of the ZnS(Ag), measured in current operation, in the low-temperature range, leads to a decrease in the relative efficiency of the detector at low gamma-ray energies (Fig. 2). However, the variation of the relative detector efficiency as a function of the radiation energy at −60°C remains satisfactory (Fig. 3).

We studied the influence of changes in time and climatic factors on the dosimetric properties of air-equivalent detectors.

The specimens under investigation were subjected to the effects of the following:

1) being kept in a moist heat chamber at a temperature of 50°C and a relative humidity of 98% for 7500 h; 2) being kept in a cold chamber at −20°C for 6000 h; 3) cyclic testing, in which the specimens were alternately placed in a moist heat chamber at 50°C and a cold chamber at −20°C, with intervening periods at normal temperature. After the tests, the detectors remained operative, i.e., they retained the same light yield and had the same variation of relative efficiency as a function of gamma-ray energy as before the tests.

The dosimetric properties of the detectors remained practically unchanged after storage for 2 or 3 years at a temperature of 20°C.

LITERATURE CITED

1. S. P. Vershinina et al., Atomnaya Énergiya, 26, 342 (1969).
2. I. M. Rozman and K. G. Tsimmer, Atomnaya Énergiya, 2, 54 (1957).
3. D. Jones and A. Ward, Proc. Phys. Soc., 486, 931 (1960).

ELECTRICAL DISCHARGE IN RADIOACTIVE DIELECTRICS

V. V. Gromov and V. V. Surikov

UDC 548.537:541.15

It was shown in [1] that the characteristic radiation on the surface of radioactive specimens with low conductivity must result in the accumulation of an electrical charge q_R which is positive in the case of beta emitters and negative for positron emitters. This charge is spread out over the complete-absorption layer R for the type of radiation in question in the material of a radioactive dielectric.

When a specimen containing a radioactive isotope is placed in a medium with high conductivity (ionized air, water, etc.), the charges accumulated in the layer R may be partially or totally compensated by current carriers of the surrounding medium. However, total neutralization of the charges does not take place in the case of specimens with low conductivity, since the electron and ion conductivity of dielectrics is low (or relatively low). Therefore, even if a radioactive dielectric is completely neutral electrically, a "double-charged layer" is formed in the region near its surface; one of the two thicknesses forming this layer is practically on the surface, while the other is in the interior of the specimen, at a distance R from its surface (Fig. 1). It should be noted that the distribution of charges in the specimen is governed by a more complicated law than that described above, but this simple model makes it fairly easy to make theoretical estimates of q_R and compare them with experimental data [1, 2].

The charge accumulated in the double-charged layer was measured for specimens of strontium sulfate and different types of glass containing Sr^{90} in equilibrium with Y^{90} (pure beta emitters, with the range of yttrium beta particles in the specimens approximately equal to 3 mm); the values found were 10 and 30 μCi/g, respectively, in terms of Sr^{90}, which confirmed the fact that a charged layer was formed in radioactive dielectrics [2], although the experimental results differed somewhat from those of theoretical calculations.

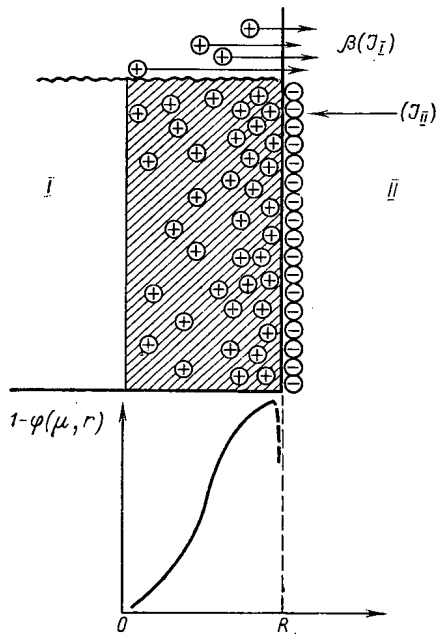

Fig. 1. Schematic diagram of the charge distribution in the surface layer of a beta-radioactive dielectric: I) dielectric; II) surrounding medium; J) current of charge-carriers; R) layer of total absorption of beta particles with maximum energy in the spectrum of the isotope under investigation; $\varphi(\mu, r)$ function defining the fraction of beta particles absorbed in the specimen with absorption coefficient μ and linear parameter r [1].

Translated from Atomnaya Énergiya, Vol. 32, No. 2, pp. 172-173, February, 1972. Original article submitted June 21, 1971.

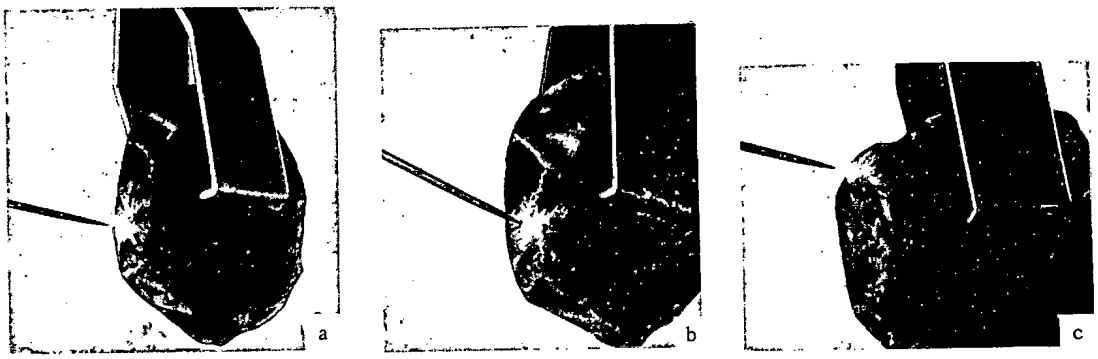

Fig. 2. Spontaneous discharge in glass containing 30 μCi of Sr^{90} in equilibrium with Y^{90} per gram of glass: a, b, c) different stages of development of the spark.

In addition to the measurements described "effects" related to the charging of radioactive dielectric specimens can be observed directly. If the formulas proposed in [1] for calculating q_R are correct, then the field strength in the layer R is approximately 10^5 V/cm for those types of radioactive glass which contain 30 μCi/g in terms of Sr^{90}. In that case, spontaneous electrical discharges must occur in the layer R (the breakdown voltage of most dielectrics is approximately 10^5 V/cm). A spark discharge of this kind was in fact observed by the authors in different kinds of radioactive glass, although to stimulate the discharges, we had to create mechanical stresses in the glass by pressing on the lump of radioactive glass with a metal or glass rod in the same way as was done in the case of irradiated dielectrics [3, 4].

The discharges were photographed with a high-speed SKS-1M-16 movie camera at a speed of 200 frames per second. We used a film negative with a sensitivity of 180 All-Union State Standard units. The preparation of radioactive glass lumps with a specific radioactivity of 30 μCi/g in terms of Sr^{90} was described in [2]. After exposure of the 16-mm film, positives were made with 35-mm film, from which the prints were made.

Figures 2a-c show the three most characteristic types of discharge. As can be seen from Fig. 1, the spark appeared in each case as soon as the rod (which was not grounded but simply held by hand) was retracted from the surface of the glass. A characteristic crackling was sometimes audible as the spark appeared. In most cases the sparks were formed immediately the first few times the rod was pressed against the glass. After that the sparking stopped. This indicated a decrease in the electric field intensity in the layer R as a result of microbreakdowns. After the radioactive lumps had been stored for a week, the spark-producing experiments were readily repeatable, since a fairly large charge had again built up in the layer R.

The experiments clearly show that a large electric charge does in fact accumulate in low-conductivity radioactive specimens; under certain conditions, this can lead to microbreakdowns in the surface layer of such specimens.

High specific radioactivity values on low-conductivity media are produced by the vitrification of radioactive wastes [5]. Apparently the occurrence of microdischarges in lumps of highly radioactive glass may even result in microfissures of the surface.

LITERATURE CITED

1. V. V. Gromov, At. Énerg., 26, 250 (1969).
2. V. V. Gromov, Zh. Fiz. Khimii, 45, No. 11 (1971).
3. I. Furuta, H. Hiraoka, and S. Okamoto, J. Appl. Phys., 37, 1873 (1966).
4. T. Proctor, Phys. Rev., 116, 1436 (1959).
5. N. E. Brezhneva et al., in: Treatment and Storage of High-Level Radioactive Wastes, IAEA, Vienna (1963), p. 441.

ISOTROPIC NEUTRON SOURCE USING THE LUÉ-25 LINEAR ELECTRON ACCELERATOR

V. P. Kovalev, V. P. Kharin,
V. V. Gordeev, and V. I. Isaev

UDC 621.384.649:539.125.5.03

Pulsed photoneutron sources based on linear electron accelerators are in widespread use in reactor physics and neutron physics, as tools in the study of neutron propagation through various media [1]. Neutron sources using linear accelerators also find applications in radiobiological experiments. Isotropic neutron sources are in demand in most practical applications of this sort. We can select that configuration and target material for the linear electron accelerator which will render the neutron source practically isotropic.

An investigation was made of the yields and angular distributions of photoneutrons from lead (Pb) targets of different configurations bombarded by 23 MeV neutrons, in order to achieve an isotropic neutron source.

The experiments were conducted using a linear electron accelerator output beam with a peak energy of 25 MeV [2]. The threshold reactions $P^{31}(n, p)Si^{31}$, $Al^{27}(n, p)Mg^{27}$, $Al^{27}(n, \alpha)Na^{24}$, with respective effective thresholds of 2.7, 4.5, and 8.1 MeV, are utilized for neutron detection. The characteristic feature of the linear electron accelerator neutron source is the high bremsstrahlung background. We therefore extended our study to cover the angular distribution of the bremsstrahlung from the target, the source of the neutrons. The bremsstrahlung background was measured by a 0.25 cm^3 ionization chamber with a 1.0 cm thick plexiglas attachment.

A beam of electrons ≈ 10 mm in diameter was aimed at the center of the target, which was positioned 30 cm from the output window of the accelerator. The neutron detectors were deployed at fixed angles around the target. The solid angles subtended by the detectors were respectively 4° and 6° in the case of phosphorus and aluminum detectors.

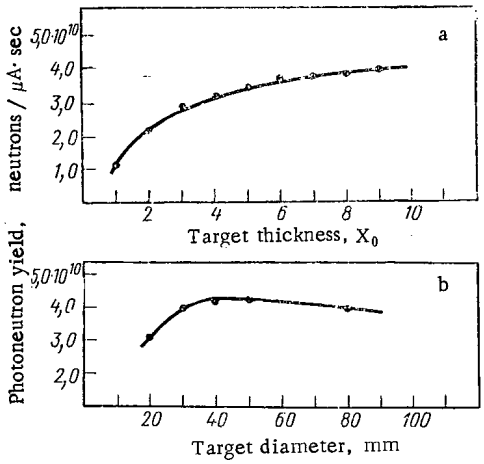

Fig. 1. Photoneutron yield as a function of thickness and diameter of lead target: a) diameter 30 mm; b) thickness 48 mm.

The activity induced as a result of the reaction $P^{31}(n, p)Si^{31}$ was recorded by a gas counter. The reactions on aluminum were detected from the characteristic γ-emission. The photoneutron yield was measured in terms of the slowing-down of neutrons in a paraffin sphere 30 cm in diameter. The detector for the slowed-down neutrons was a thin indium foil placed in the center of the sphere. The sphere was placed at a 90° angle to the direction of the incident beam of electrons, at a distance of 40 cm from the target. Absolute calibration of the neutron detector against a Pu–Be source with a known photoneutron energy spectrum was carried out beforehand. Corrections for the difference in the energy spectra of the Pu–Be photoneutron source and the spectrum of photoneutrons from the lead amounted to 4%. The efficiency for the neutron detector in these calculations was taken from [3].

Translated from Atomnaya Énergiya, Vol. 32, No. 2, pp. 173-175, February, 1972. Original article submitted May 11, 1971; final revision submitted June 14, 1971.

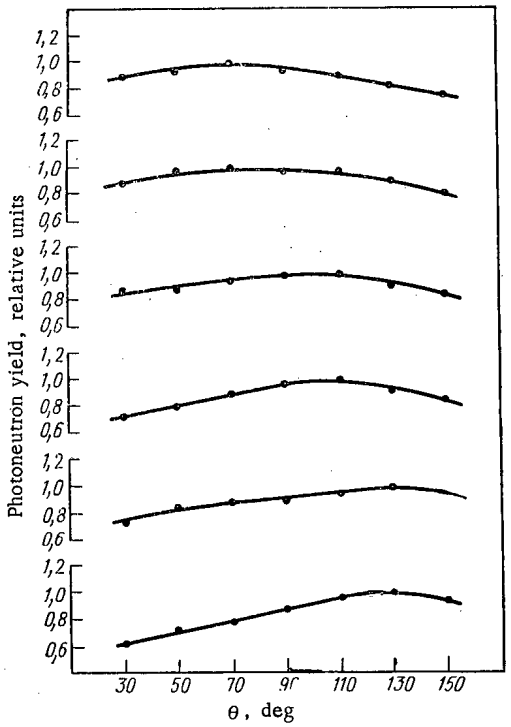

Fig. 2. Angular distributions of photoneutrons: detector $P^{31}(n, p)Si^{31}$ employed; h) depth of counter well. 1) h = 5 mm; 2) h = 10 mm; 3) h = 15 mm; 4) h = 20 mm; 5) h = 25 mm; 6) h = 30 mm.

The energy spectrum of the photoneutrons emitted from the lead was treated, in the case of 23 MeV electrons, as an evaporation spectrum with the temperature T = 1.35 MeV [4].

The yield of photoneutrons from lead was measured as a function of the thickness and diameter of a disk-shaped target, in order to optimize target dimensions. Figure 1 shows the results of these measurements. The highest photoneutron yield for a target 30 mm in diameter and energy of incident electrons 23 MeV is observed in the case of thicknesses greater than 9 X_0 (where X_0 is the radiation length) (see Fig. 1a). The maximum yield of photoneutrons from lead as a function of diameter is observed at target diameters 40-60 mm (see Fig. 1b).

The angular distributions of photoneutrons were measured for spherically shaped targets 40 mm and 60 mm in diameter. The effect of deeper wells in the target on the angular distribution of neutrons was also investigated. The targets were fabricated with a well 15 mm in diameter and variable depth. A well extending to 20 mm depth in the target reduces neutron yield by not more than 10%, at the same time exerting a perceptible effect on the angular distribution of neutrons. Figure 2 shows results of measurements of the angular distributions of photoneutrons from a target 60 mm in diameter with a variable-depth well, demonstrating the characteristic deformation of the angular distributions encountered in the case of a P(n, p) detector. The angular distribution closest to isotropic (within 15%) is that of the 60 mm diameter target with a 20 mm deep well. The yield of photoneutrons from that type of target is $4.0 \cdot 10^{10}$ neutrons/μA · sec.

Measurements using Al(n, p) and Al(n, α) detectors give indications of increased anisotropy in the angular distributions as the neutron recording threshold rises. The minimum anisotropy of the Al(n, p) detector is observed at well depth of 10 mm, and amounts to 27%, while the minimum anisotropy of 37% is obtained in the case of an Al(n, α) type detector at well depth 25 mm.

The minimum bremsstrahlung background for a target of optimized dimensions (sphere 60 mm in diameter, with well depth 20 mm) was obtained at a 145° angle to the direction of the electron beam, and found to be 1.7 R/μA · min. The maximum bremsstrahlung background is observed at angle 0°, and is found to be 75 R/μA · min. The background at 90° amounts to 3.3 R/μA · min.

The results of the investigation support our recommending the spherically shaped (60 mm diameter) lead target with 20 mm deep well as a practically isotropic neutron source for 23 MeV electrons.

LITERATURE CITED

1. Pulsed Method in Neutron Physics, edited by P. Griebner and E. Henley [Russian translation], Atomizdat, Moscow (1969).
2. V. I. Ermakov et al., At. Énerg., 29, 206 (1970).
3. R. Bramblett, R. Ewing, and T. Bonner, Nucl. Instrum. and Methods, 9, No. 1 (1960).
4. M. Toms and W. Stephens, Phys. Rev., 108, 77 (1957).

CALCULATION OF THE YIELD OF D – T NEUTRONS WITH PERIODIC REPLENISHMENT OF THE TARGET WITH TRITIUM

V. T. Tustanovskii

UDC 539.172.13

It was shown in [1] that the decrease in the yield of D–T neutrons from zirconium–tritium and titanium–tritium targets can be explained completely by the diffusive replacement of tritium by deuterium. The deuterons from the beam which are stopped in the target produce an excess hydrogen concentration, so deuterium and tritium diffuse from the target. The deuterium and tritium evolution rates at any time are proportional to the concentrations C^D and C^T. Since deuterons are constantly incident on the target, and both deuterium and tritium are evolved, the yield of D–T neutrons decreases, and the yield of D–D neutrons increases.

The tritium loss in the target can be made up through the use of a mixed deuterium–tritium beam or by alternately bombarding the target with deuteron and triton beams [2, 3].

Using the first method, we can achieve a constant neutron yield at a level a factor of three or more below the maximum yield $K_{0,T}$ [4], which occurs at the beginning of the target bombardment by the deuteron beam.

With the second method, we can achieve a neutron yield approaching the maximum yield $K_{0,T}$. For this purpose we must select proper conditions for the alternate bombardment of the target by deuterons and tritons.

We derive below the equations characterizing the change in the yield of D–T neutrons during periodic replenishment of tritium, and we report some calculated results.

According to [1], the yield K_T of the D-T reaction is

$$K_T = C_{0\vartheta} e^{-\alpha Q} \int_0^W \frac{\sigma_T}{B}\, dW, \tag{1}$$

where C_0 is the initial tritium concentration in the target, Q is the charge delivered to the target by the incident deuteron beam, W is the energy of the incident particles (in kiloelectron volts), σ_T is the effective cross section for the D–T reaction, B is the energy loss of the incident particles in the target layer (B = dW/dx); and

$$\alpha = 1.04 \cdot 10^{-2} \frac{A\bar{B}\nu}{\alpha_0 WS}. \tag{2}$$

where A is the atomic weight of the carrier in the target, ν is the number of particles in an ion of the bombarding beam, α_0 is the number of target nuclei per carrier atom, $\bar{B}$ is the target stopping power, averaged over the range (kiloelectron volts per milligram per square centimeter), and S is the cross-sectional area of the beam (square centimeters).

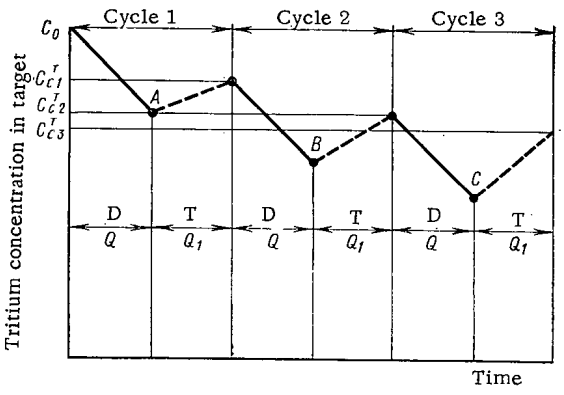

Fig. 1. Periodic replenishment of the target with tritons.

Translated from Atomnya Énergiya, Vol. 32, No. 2, pp. 175-177, February, 1972. Original article submitted May 20, 1971.

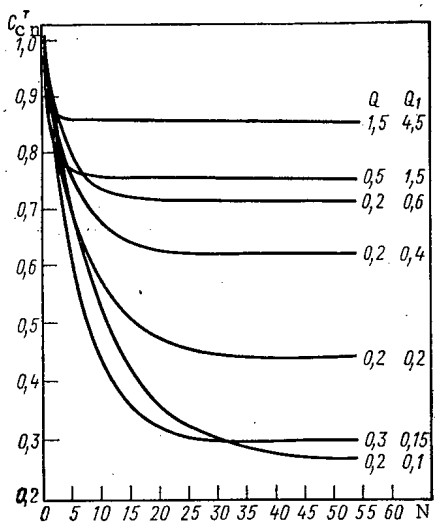

Fig. 2

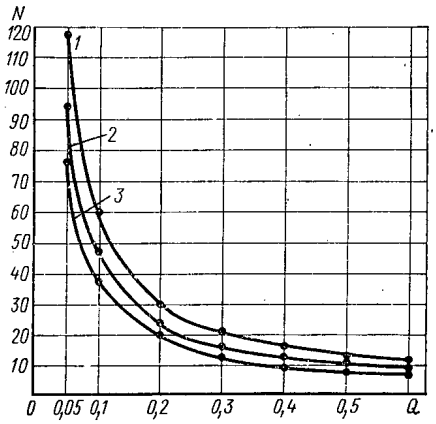

Fig. 3

Fig. 2. Dependence of the tritium concentration in the target on the number of cyles of periodic bombardment by the deuteron and triton beams (tritium – zirconium target, accelerating voltage of 200 keV, and beam diameter of 14 mm).

Fig. 3. Number of cycles required for saturation, as a function of Q. 1) M = 1; 2) 1.5; 3) 2.

At a constant beam energy, the neutron yield depends only on the tritium concentration in the target. We assume that W = const; then the yield of D–T neutrons at any time can be expressed in units of the initial tritium concentration in the target. We will assume that the tritium and deuterium concentrations at any time are the same throughout the target layer and that their sum is always equal to C_0.

We denote by C^T and C^D the tritium and deuterium concentrations in the target; we will also use a subscript to denote the cycle number. A cycle consists of a bombardment by the deuteron beam (charge of Q) followed by replenishment of the target with tritons (charge Q_1) (Fig. 1).

We assume that $C_0 = 1$, $e^{-\alpha Q} = l$; $e^{-\alpha_1 Q_1} = K$. After the first irradiation of the target with the deuteron beam, the tritium and deuterium concentrations are $C^T_A = C_0 l = l$ and $C^D_A = 1-l$; thereafter we have

$$C^D_{c1} = (1-l)K;\ C^T_{c1} = 1-(1-l)K;\ C^T_B = lC^T_{c1}; \tag{3}$$

$C^D_B = 1 - lC^T_{c1}$; $C^D_{c2} = C^D_B K$; $C^T_{c_2} = 1 - C^D_{c2}$; etc. (see Fig. 1 for the notation).

As a result, we find the tritium concentration after n cycles to be

$$C^T_{cn} = 1-(1-l)K\sum_{m=1}^{n}(Kl)^{m-1}, \tag{4}$$

which we can convert to the form

$$C^T_{cn} = 1-(1-l)K\frac{1-S^n}{1-S}, \text{ where } S = Kl. \tag{5}$$

Since S < 1, we have, as $n \to \infty$,

$$C^T_{cn} = 1-(1-l)K\frac{1}{1-S} = \frac{1-K}{1-S}. \tag{6}$$

Accordingly, during the periodic replenishment of the target with tritium, a saturation sets in, after which the yield of D–T neutrons at the beginning of each cycle is the same, given by

$$K_T = \frac{1-K}{1-S}K_{0,T}. \tag{7}$$

To determine the number of cycles at which saturation sets in, we write

$$R = C^T_{cn} - C^T_{cs} \tag{8}$$

where R gives the difference between C^T_{cn} and the tritium concentration in the target at saturation (C^T_{cs}). For practical purposes, it is sufficient to choose R = 0.01. Substituting Eqs. (5) and (6) into Eq. (8), we find

$$N = \lg\left(\frac{R(1-S)}{K-S}\right)\Big/\lg S. \quad (9)$$

Figure 2 shows the tritium concentration as a function of the number of cycles of target bombardment by the beam of deuterons and tritons under various conditions.

We see that a constant tritium concentration is reached in the target under all replenishment conditions, so a constant neutron yield is reached at the beginning of each cycle. The yield of D–T neutrons increases with increasing ratio $M = Q_1/Q$ and with increasing Q for a given M. Analysis of Eq. (7) shows that C^T_{cs} depends much more strongly on M than on Q.

The number of cycles required for saturation was calculated as a function of the charge delivered by the deuteron beam to the target on the basis of Eq. (9). As Fig. 3 shows, N depends strongly on Q; as M increases, the dependence of N on Q weakens.

The time required to reach saturation increases linearly with the beam energy, due to the retardation of the isotopic substitution of hydrogen as the thickness to the working layer of the target increases.

The charge Q_1 should be of the same order as Q for use of this method of periodic replenishment of the target with tritium.

In conclusion the author thanks L. N. Katsaurov and A. N. Kuznetsov for discussion of these results, and V. M. Kokhrin for assistance in the calculations.

LITERATURE CITED

1. L. N. Katsaurov and A. N. Kuznetsov, At. Énerg., 21, 390 (1966).
2. L. N. Katsaurov and A. N. Kuznetsov, Preprint, P. N. Lebedev Physics Institute, Academy of Sciences of the USSR, No. 12 (1966).
3. J. Hollister, Nucleonics, 22, 6 (1964).
4. I. Ya. Barit et al., Abstracts of Reports, II All-Union Conference on Activation Analysis, Tashkent, (1968).
5. Hara Eiichi, Japan J. Appl. Phys., No. 7, 70 (1968).

RELATIVE PROBABILITY OF Am^{242} BETA DECAY

V. Ya. Gabeskiriya

UDC 539.165

Neutron irradiation of Am^{241} is extensively used for the production of isotopes of transuranic elements. The nuclear reactions occurring during Am^{241} irradiation are shown in Fig. 1.

One of the basic constants determining isotopic yield during Am^{241} irradiation is the relative probability of Am^{242} β decay. Several papers have been published which deal with the measurement of this quantity [1-7]. The most precise value for the relative β-decay probability, 0.836 ± 0.003, was obtained from measurements of the Pu^{242} and Cm^{242} content in an irradiated Am^{241} target [7]. In this case, the accuracy was limited by the error in absolute measurements of the Pu^{242} and Cm^{242} content.

In this work, the quantiy k – the relative probability of Am^{242} decay – was determined in the following manner. If one irradiates Am^{241} by an integral neutron flux such that there is negligible burnup of the isotopes Pu^{242} and Cm^{242} along with its decay product Pu^{238}, which are produced during irradiation ($\sim 5 \cdot 10^{19}$ neuts/cm^2), and allows the Cm^{242} to decay, the Pu^{238}/Pu^{242} atomic ratio will be equal to the ratio of the probabilities for β decay and electron capture in Am^{242}, as can be seen from Fig. 1. Furthermore, the holding time for the irradiated sample must satisfy the condition $\lambda_2 t \gg 1$, where λ_2 is the decay constant of Cm^{242}. The measurement of the quantity k thus reduces to a determination of the Pu^{238}/Pu^{242} ratio, which can be measured on a mass spectrometer with great accuracy (to 1%).

However, the samples studied were irradiated by a comparatively high integral neutron flux; the appropriate corrections were therefore made for burnup of the isotopes Pu^{238}, Pu^{242}, and Cm^{242}. This led to additional error in the measurement of k because the values of the total effective neutron absorption cross sections appearing in the calculations for the isotopes Cm^{242}, Pu^{242}, and Pu^{238}, and the integral neutron flux were known to have significant error.

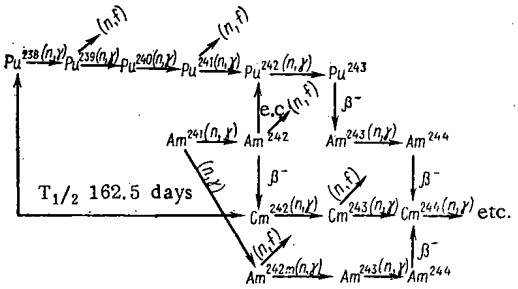

Fig. 1. Nuclear reactions occurring in a reactor during Am^{241} irradiation.

TABLE 1

Am^{242} β-decay probability	Reference	Am^{242} β-decay probability	Reference
0,85	[1]	0,78	[5]
0,82	[2]	0,840±0,004	[6]
0,81	[3]	0,836±0,003	[7]
0,80	[4]	0,827±0,003	this work

The error in the measurement of the quantity k was calculated from

$$\Delta k = \sqrt{\sum_{i=1}^{n} (\Delta k_i)^2},$$

where Δk_i is the variation in the calculated value of k for a variation in the i-th parameter contributing to the magnitude of the error. All sources of error enumerated above were taken into account in the calculations. The calculations were made on a 3M high-speed computer using analytical results from nine irradiated Am^{241} targets.

Table 1 gives the weighted mean values of the relative Am^{242} β-decay probability obtained in the present work and by others.

As is clear from the data presented, our results are in satisfactory agreement with previously published values. However, there is a small disagreement with the results of

Translated from Atomnaya Énergiya, Vol. 32, No. 2, p. 177, February, 1972. Original article submitted April 9, 1971.

[6, 7]. For a conclusive refinement of the Am^{242} β-decay probability, it would be advisable to make a measurement of this quantity by the proposed method. To do this, it is necessary to irradiate Am^{241} by a small integral neutron flux.

In conclusion, I want to thank G. A. Silant'ev for performing the mass-spectrometric analyses.

LITERATURE CITED

1. G. O'Kelly, Nucl. Sci. Abstr., 7, No. 2413 (1953).
2. S. A. Baranov and K. N. Shlyagin, USSR Academy of Sciences Session on Peaceful Uses of Atomic Energy [in Russian], Izd-vo AN SSSR, Moscow (1955), p. 251.
3. R. Hoff, Phys. Rev., 100, 1403 (1955).
4. T. Passell, Nucl. Sci. Abstr., 9, No. 24B (1955).
5. R. Hoff, Nucl. Sci. Abstr., 9, No. 24B (1955).
6. R. Barnes et al., J. Inorg. Nucl. Chem., 9, 105 (1959).
7. R. Hoff et al., J. Nucl. Energy, 8, 224 (1959).

SLOW NEUTRON CAPTURE CROSS SECTION OF Pa^{231}

B. M. Aleksandrov, M. A. Bak,
A. S. Krivokhatskii, and É. A. Shlyamin

UDC 539.172.4.162.2

The purpose of this work was the determination of the value of the thermal neutron capture cross section for Pa^{231} and of the values of the resonance capture integral. The literature gives a value $\sigma_c = 200 \pm 10$ b [1], obtaining for a neutron energy of 0.025 eV and $\sigma_c = 300 \pm 45$ b [2] for a reactor neutron spectrum. During irradiation of Pa^{231} in a reactor, buildup of U^{232} occurs in accordance with the scheme

$$Pa^{231}(n, \gamma)\, Pa^{232} \xrightarrow{\beta} U^{232}.$$

Both the original Pa^{231} and the U^{232} undergo α decay with the ratio of their half lives being

$$\frac{T_{Pa^{231}}}{T_{U^{232}}} = 439.$$

So large a ratio for these quantities makes it possible to observe a marked increase in α activity of an irradiated target for comparatively short irradiations (of the order of a few hours) in a flux of $\sim 10^{14}$ neuts /cm^2-sec.

Irradiation of cadmium-covered and bare targets in identical neutron fluxes affords an opportunity to obtain the value of the resonance integral I as well as the value of the thermal capture cross section σ_c. These quantities are connected by the following relation

$$R - 1 = K \frac{\sigma_c}{I},$$

where K is a coefficient characterizing the ratio of the thermal and resonance portions of the flux, and R is the cadmium ratio.

Between the increase in α activity of irradiated and stored Pa^{231}, the value of the integral neutron flux, and the thermal neutron capture cross section there exists a simple relationship:

$$\sigma_c = \frac{1}{\Phi t} \cdot \frac{T_{U^{232}}}{T_{Pa^{231}}} \left[\left(\frac{S_{U^{232}}}{S_{Pa^{231}}} \right)_{\text{without Cd}} - \left(\frac{S_{U^{232}}}{S_{Pa^{231}}} \right)_{\text{with Cd}} \right],$$

where Φ is the neutron flux density, t is the irradiation time, and $S_{U^{232}}$ and $S_{Pa^{231}}$ are the areas under the U^{232} and Pa^{231} α peaks.

Protactinium targets were irradiated in a vertical channel of the VVR-M reactor. They were prepared by electrolytic deposition of microgram amounts of Pa^{231} (~ 10 μg) on a titanium backing 0.2 mm thick. The neutron flux at the sample location was measured by means of Np^{237} targets [3].

After irradiation and storage for $\sim 10 T_{Pa^{232}}$, the Pa^{231} and Np^{237} targets were measured on an α spectrometer with a surface barrier gold–silicon detector. Since the measurements of α-peak areas are relative and can be accomplished with an error of $\sim 1\%$, the main contribution to measurement error is the error in measurement of neutron flux density. In the present work, the flux was measured with an error of 4%.

The thermal neutron capture cross section for Pa^{231} was found to be 260 ± 13 b.

The experimentally determined values of the cadmium ratios ($R_{Np} = 7.46$ and $R_{Pa} = 9.12$) were used to determine the resonance neutron capture integral for Pa^{231}. If one takes the value of the resonance

Translated from Atomnaya Énergiya, Vol. 32, No. 2, p. 178, February, 1972. Original article submitted June 7, 1971.

neutron capture integral for Np to be I_{Np} = 945 b, the resonance capture integral for protactinium turns out to be 1180 ± 120 b.

LITERATURE CITED

1. F. Simpson et al., Nucl. Sci. and Engng, 12, 243 (1962).
2. R. Elson et al., Phys. Rev., 90, 102 (1953).
3. M. A. Bak et al., Proceedings of the Second Coordinating Conference on High-Dose Dosimetry [in Russian], FAN, Tashkent (1966), p. 121.

Cf^{249} FISSION CROSS SECTION FOR FAST AND THERMAL NEUTRONS

B. I. Fursov, Kh. D. Androsenko,
V. I. Ivanov, V. G. Nesterov,
G. N. Smirenkin, L. V. Chistyakov,
and V. M. Shubko

UDC 539.173.84

To measure the fission cross section (σ_f) of Cf^{249}, we used a californium sample obtained from β decay of Bk^{249} which was thoroughly purified of the heavier californium isotopes that create an undesirable spontaneous fission background. The main source of this background is the most shortlived isotope Cf^{252}. As the result of measures taken, the Cf^{252} content in the sample was reduced to $2 \cdot 10^{-6}\%$. The Cf^{249} target weighing $\sim 3\ \mu g$ and 4 mm in diameter was obtained by electrodeposition on a thin platinum backing.

Thermal neutron measurements were made in the thermal column of the BR-5 reactor. An electrostatic generator was the fast neutron source. The fission fragment detectors used were an ionization chamber in the first case and glass cylinders in the second.

Relative measurements were used in both cases, eliminating the need to consider the value of the neutron flux, for which a Pu^{239} target (isotopic purity, 99.8%), having a fission cross section that was known rather well and of the same dimensions as the target under study, was mounted in the detection equipment close to the target being investigated.

The ratio of the numbers of fissioning nuclei in the targets was determined from the α activity by means of a semiconductor detector. The following values were used for the half lives: Pu^{239}, $(2.438 \pm 0.005) \cdot 10^4$ years [1] and Cf^{249}, 352 ± 6 years [2].

In the accelerator measurements, the distance from the accelerator target to the fissioning layer was 50 mm, and the distance from the layer to the glass detector was 40 mm. Measurements in this geometry permitted a study of the angular distributions of the fission fragments.

The anisotropic portion of the angular distributions of the fragments is satisfactorily described by a quadratic dependence on $\cos\theta$. A description of the experimental data by least squares in terms of this assumption allows one to determine the angular anisotropy $\sigma_f(0°)/\sigma_f(90°)$. The spontaneous fission background was about 10%.

TABLE 1. Results and Pu^{239} Fission Cross Section Values Used

E_n, MeV	ΔE_n, MeV	$\frac{\sigma_f(Cf^{249})}{\sigma_f(Pu^{239})}$	$\Delta\left(\frac{\sigma_f(Cf^{249})}{\sigma_f(Pu^{239})}\right)$	$\sigma_f(Pu^{239})$, b	$\sigma_f(Cf^{249})$, b	$\Delta\sigma_f(Cf^{249})$, b	$\frac{\sigma_f(0°)}{\sigma_f(90°)}$	$\Delta\left(\frac{\sigma_f(0°)}{\sigma_f(90°)}\right)$
Thermal	—	2,049	±0,054	790	1619	±43	—	—
0,500	±0,090	0,997	±0,030	1,59	1,58	±0,05	0,102	±0,050
0,750	±0,080	0,876	±0,027	1,64	1,44	±0,05	0,030	±0,080
0,850	±0,075	0,810	±0,025	1,68	1,36	±0,06	0,133	±0,060
1,450	±0,070	0,866	±0,030	1,93	1,67	±0,06	0,137	±0,060
4,000	±0,100	1,072	±0,042	1,82	1,95	±0,08	0,134	±0,080
4,500	±0,100	1,120	±0,039	1,78	1,99	±0,07	0,209	±0,060
5,020	±0,100	1,135	±0,034	1,76	2,00	±0,06	0,158	±0,050

Translated from Atomnaya Énergiya, Vol. 32, No. 2, pp. 178-179, February, 1972. Original article submitted June 14, 1971.

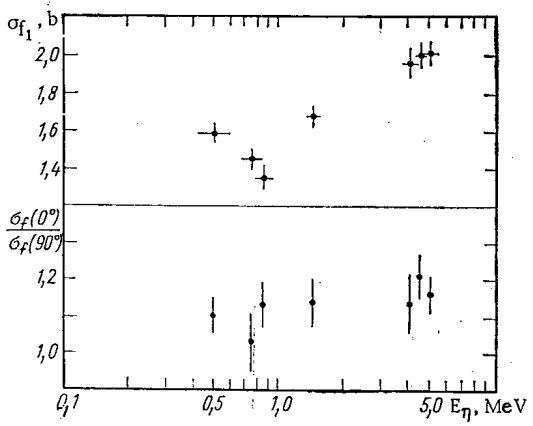

Fig. 1. Fission cross section and angular anisotropy of Cf^{249} fission fragments.

The thermal neutron fission cross section for Cf^{249} was found to be 1619 ± 43 b. The reference Pu^{239} fission cross section for a Maxwellian neutron spectrum at a temperature of 20°C (790 b) was taken from [3] and the fast neutron reference cross section was taken from [4].

The results (see Fig. 1) and the Pu^{239} fission cross section values used are given in Table 1. The uncertainty of $\sigma_f(Pu^{239})$ is not included in the error for $\sigma_f(Cf^{249})$.

The thermal neutron fission cross section for Cf^{249} agrees with the value given in [5]. The fast neutron fission cross section is lower than the value obtained in [6].

LITERATURE CITED

1. G. Hanna et al., Atomic Energy Rev., 7, 3 (1969).
2. D. Metta et al., J. Inorganic and Nucl. Chem., 31, 1245 (1969).
3. Neutron Cross Sections, Vol. III, BNL-325, Supplement No. 2 (1965).
4. T. Byer and V. Konshin, Third Conf. on Neutron Cross Sections and Technology (March 15-17, 1971), University of Tennessee, Knoxville, USA.
5. R. Benjamin, K. MacMurdo, and J. Spencer, ibid.
6. P. Vorotnikov et al., Nucl. Phys., A150, 56 (1970).

AN UNIDENTIFIED ALPHA ACTIVITY OF THORITE

K. A. Petrzhak, M. I. Yakunin,
and G. M. Ter-Akop'yan

UDC 539.164

Cherry et al [1] report that thorite separated from Conway granite shows an excess unidentified alpha activity in the 4.4 MeV region. This work preceded [2] on an unknown alpha activity in the 4.2-4.6 MeV range observed in the study of certain geological specimens. As a result of subsequent papers on the unknown radiator and the search for natural transuranium isotopes a very definite opinion on the nature of this alpha radiator was expressed in [3]. It is stated in [3] that alpha particles with energies in the 4.4-4.6 MeV range appear to belong to some transuranium radiator which approximates osmium in chemical properties and is a progenitor of natural Pu^{239}.

A study of the published materials on this puzzling radiator indicates that its effect appears most clearly in the alpha spectrogram of thorite [1]. Thanks to the kindness of J. Adams in sending G. N. Flerov a specimen of Conway granite containing dispersed thorite we were able to work with these materials.

In view of the difficulty of obtaining thorite we investigated the heavy fraction of the granite separated by sedimentation of the pulverized material in bromoform. The study was made by ionization alpha spectrometry. The spectrometric sources were made by cathode sputtering. One of the sources contained 6 ± 3 mg of the heavy fraction and had an area of 1400 cm^2; the second contained about 0.2 g of granite and had an area of 4200 cm^2. Sheet steel was used as backing for the sources. The ionization chamber contained a grid and had cylindrical electrodes. The spectrum was recorded with a 100-channel pulse height analyzer. Since 100 channels are not enough to make a detailed recording of the spectrum over the whole energy range of interest, the low-energy and high energy parts of the spectrum were taken separately and then joined.

The solid curve in Fig. 1 shows the alpha spectrum of the heavy fraction obtained during 12 hours of measurements. All the peaks are easily identified by the energy scale constructed by calibration with a

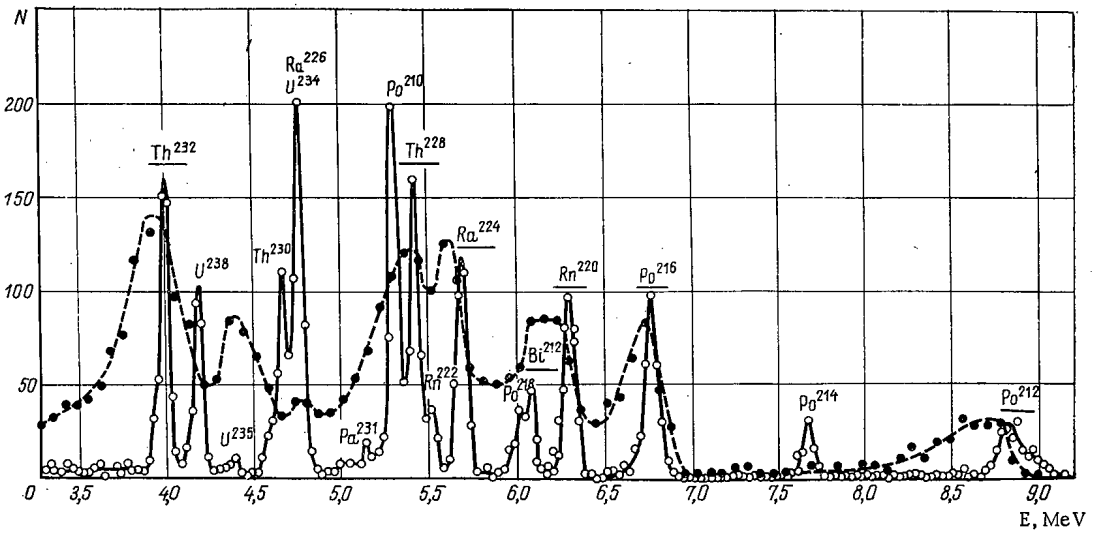

Fig. 1. Alpha spectrum of the heavy fraction of Conway granite.

Translated from Atomnaya Énergiya, Vol. 32, No. 2, pp. 179-181, February, 1972. Original article submitted June 14, 1971.

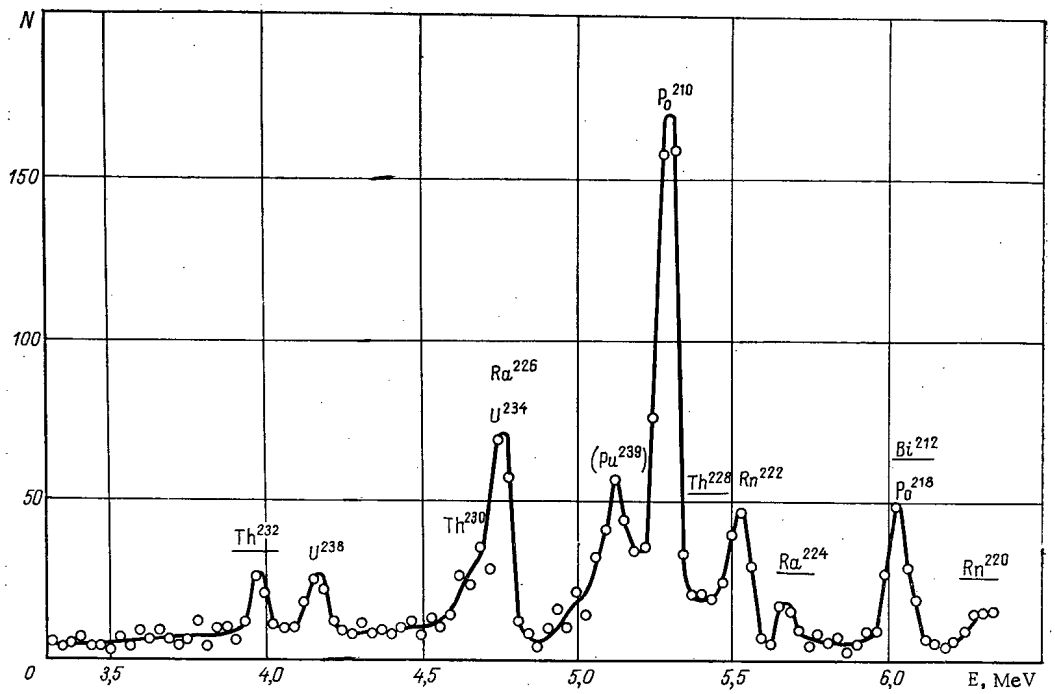

Fig. 2. Alpha spectrum of Conway granite.

reference source containing natural uranium, Pu^{239}, Am^{241}, and Cm^{244}. In addition to the peaks of the thorium series underlined in the figure there are the peaks of the uranium series corresponding to an activity about 0.6 that of thorium. The U^{235} and Pa^{231} peaks of the actinium series can also be observed. The magnitude of the U^{235} peak in the particularly interesting region around 4.4 MeV corresponds to the natural ratio of U^{235} to U^{238}. For convenience in comparing our study of the alpha activity of the specimen with the results in [1] we show dotted in Fig. 1 the alpha spectrum of thorite constructed by transferring the points from the analogous figure of [1]. The dotted curve shows that the activity of the preparation studied in [1] is due mainly to the thorium series with an insignificant addition from the uranium series and apparently a new unknown radiator with alpha particle energies close to 4.4 MeV. Thus the results of our investigation of the alpha activity of thorite completely contradict those of [1].

The discrepancy in the ratios of the thorium and uranium activities might be due to a difference between the thorite specimen studied in [1] and the heavy fraction we used. Therefore we performed supplementary studies of the alpha activity of granite which might contain thorite closer in composition to that studied in [1] or some other carrier of the interesting radiator. In making a spectrometric source of granite the cathode sputtering process had to be intensified since the low specific activity of granite requires a source containing a large amount of material. In order to avoid heating the layer in the deposition process the backing holder was cooled by running water. This precaution was observed because the oxides of the radiator being sought are assumed to be volatile [3].

The alpha activity of Conway granite is shown in Fig. 2. Like the alpha spectrum of the heavy fraction it does not contain any extra peak except the one close to 5.15 MeV which appears to belong to Pu^{239}. In our opinion this peak has a pure laboratory origin since a peak is sometimes observed in alpha spectra backgrounds.

Thus our experiments with the grahite specimen furnished by J. Adams do not confirm the results of [1], i.e., they do not show an excess unidentified alpha activity near 4.4 MeV.

LITERATURE CITED

1. R. Cherry, K. Richardson, and J. Adams, Nature, 202, No. 4933, 639 (1964).
2. V. V. Cherdyntsev and V. F. Mikhailov, Geokhimiya, No. 1, 3 (1963).
3. V. V. Cherdyntsev et al., Geokhimiya, No. 4, 395 (1968).

INFORMATION

STARTUP OF THE THIRD POWER UNIT OF THE NOVAYA VORONEZH NUCLEAR POWER STATION

An operating load of fuel was supplied to the water-cooled water-moderated power reactor of the third power-generating unit of the Novaya Voronezh nuclear power station on December 27, 1971. After the startup of this new power unit, whose output level is rated at 440 MW(e), the total installed power output of the power station now exceeds one million kW. The new reactor is the first functioning unit of the VVÉR-440 series, to be installed at the Novaya Voronezh nuclear power plant (in the fourth power-generating unit), at the Kola and Armenian nuclear power stations, and also at nuclear power stations being built in Bulgaria, in the German Democratic Republic, and in Finland.

Translated from Atomnaya Énergiya, Vol. 32, No. 2, p. 181, February, 1972.

CHRONICLES

XXI SESSION OF THE COMECON PERMANENT COMMISSION (PKIAÉ SÉV)

A. Panasenkov

The session of the COMECON Permanent Commission on the peaceful uses of atomic energy (PKIAE SEV) was held in the Socialist Republic of Rumania in late November 1971.

The Commission reviewed a number of problems concerning the resolutions of the XXV session of COMECON and of the sessions of the Executive Committee of the Council, and discussed various concrete scientific and technical problems in the area of speeding up the development and effective implementation in the national economy of advances in nuclear power on a full industrial production scale. The basis taken for this work is the Comprehensive Program of further collaboration and development of the socialist economic integration of the COMECON member-nations.

The sequence and time periods for developing measures envisaged in the Comprehensive Program, including forecasts of nuclear power development, were confirmed at the sessions of the Permanent Commission. The forecasts in this area will take into account the overall prognosis of the development of power generating capacities in the COMECON member-nations for the period ahead to 1990, with the basic tendencies operative to the year 2000 sketched out. The work plan of the Permanent Commission for the coming two years calls for completion of the development of the forecast in 1973, on the basis of data, broken down by countries, on the expected contribution of nuclear power to the fuel and power balance of the respective countries.

With the object of developing scientific and engineering prerequisites for expediting the speedy development of nuclear power, the Permanent Commission adopted the Programs of Scientific-Technical Collaboration on several topics in the area of design of VVÉR-1000 and BN type large-output reactor facilities, and on research and development work on technological processes for recovery of spent fuel elements.

In line with the decision of the COMECON Executive Committee, a sequential order to be followed in working out proposals on optional forms and organization of collaboration between the various countries, in cooperative and specialized production of reactor equipment and subassemblies for the VVÉR-440 and VVÉR-1000 reactor installations, was agreed upon and formally approved. This comprehensive program is being developed by COMECON subsidiary bodies with the participation of representatives of industry familiar with machinery design and manufacture, electric power, and nuclear power.

The Permanent Commission confirmed the Statements issued on setting up Coordination Scientific-Technical Councils (KNTS), and approved the Program of Collaboration on the three problems and topics covered in the coordination plan of scientific and engineering research for the 1972-1975 period:

- dealing with water management for water-cooled water-moderated reactors, radiation monitoring of coolants and equipment for alleviating radiation hazard in coolants;
- dealing with investigations of fast power reactors;
- dealing with reprocessing of spent fuel from thermal reactors.

A Draft Program of collaboration between COMECON member-nations on physical research on reactors, using a VVÉR type critical assembly, was discussed and improved. The interested countries agreed upon a Draft Agreement on setting up a provisional international scientific research collective for carrying out joint work based on that facility.

Translated from Atomnaya Énergiya, Vol. 32, No. 2, p. 182, February, 1972.

Materials of a KNTS report on radiation engineering and radiation technology were discussed at the session of the Permanent Commission, and measures on collaboration between COMECON member-nations in the field of industrial materialization and implementation on a full production scale of radiation-induced grafting of polymers were confirmed and approved.

Taking into account the problems involving in achieving and maintaining protection of the environment from radioactive pollution with the increasing incorporation of nuclear power into the national economy on a full production scale, the Permanent Commission approved the Program of Collaboration of COMECON member-nations in the field of radiation safety, and adopted a resolution to convene a Coordination Scientific-Technical Council on Radiation Safety (KNTS-RB). The East German delegation took upon itself the responsibility for organizing collaboration in this area.

The Program of Collaboration of COMECON member-nations in the field of development of radiation protection equipment and techniques was also approved, and this program envisages the development of standard technological equipment and operational-technological accessories to be used in dry glove boxes and radiation caves where radioactive materials are handled.

It was also reported, at the session, that COMECON member-nations are interested in organizing multifaceted collaborative activities for making use of the International Nuclear Information System (INIS), and an appropriate program was approved for this area of work for the 1972-1975 period.

COLLABORATION LOGBOOK

A conference of experts from Hungary, East Germany, Poland, Rumania, the USSR, and Czechoslovakia was held in Warsaw in September, 1971, to discuss the results of an interlaboratory experiment on analysis of unitized radiopharmaceutical preparations of sodium o-iodohippurate labeled with I^{131}. Extensive preparations went into the conference: a program was developed for the compilation of techniques employed in COMECON member-nations in the analysis of radiopharmaceutical preparations; specimens of the preparation in question were prepared and circulated for analysis; analysis was carried out simultaneously in the laboratories of the nations participating in the experiment; results were processed and reports worked up for presentation at the conference.

The conference heard and discussed a review report prepared by Polish specialists and containing the experimental data processed by mathematical statistics techniques. This made it possible to arrive at a quantitative estimate of the methods employed in the analysis and to agree on those methods to be preferred in practical work.

The experts reached agreement on a program of further research in this field covering the 1972-1973 period.

* * *

A conference of experts and specialists from Hungary, East Germany, Poland, Rumania, the USSR, and Czechoslovakia on collaboration in the utilization of the International Nuclear Information System (INIS) was held in Moscow in September-October, 1971. Colleagues of the International Center for Scientific and Technical Information, and of the Secretariat Division of COMECON, took part in the work of the conference.

The conference heard information presented by representatives of the various countries on their experience in organizing work geared to expedite the use of the INIS system, and information presented by the delegate of the International Center for Scientific and Technical Information on the problems and activities of the Center in the coordination of national, industry-wide, and topical data acquisition and retrieval systems in COMECON member-nations. Information presented by Soviet specialists was also heard, in a report entitled "Assessment of results of the first year of utilization of INIS."

In the course of the discussions, the specialists covered the following ground: the need to achieve compatibility between the various data sharing and retrieval systems in effect in the COMECON member-nations; exchange of experience on integration, selection, and feed-in of materials to the INIS system; the need to organize regular exchange of materials on data-processing machinery data-carrying vehicles (magnetic tape and punched tape), unitization of equipment for readout and reproduction of microfilm and microcard files; feasibility of compatible training measures in separate areas for the preparation of feed-in and utilization of INIS materials, etc.

The conference developed a Draft Program of collaboration between COMECON member-nations on utilization of INIS services for the 1972-1975 period.

* * *

A seminar and conference of specialists of the COMECON member-nations on collaboration in the field of radiation safety was held in Sofiya in October, 1971. The status and developmental outlook of work

Translated from Atomnaya Énergiya, Vol. 32, No. 2, pp. 182-183, February, 1972.

in the field came under discussion at the seminar. A total of thirteen papers covering a variety of topics pertaining to radiation safety was presented. The specialists centered attention on major regulatory documents, and specifically nation-wide radiation safety rules and regulations. It was stressed that the international regulatory documents prepared or endorsed by the International Atomic Energy Agency (IAEA) and by the International Commission on Radiobiological Protection (ICRP) must serve as points of departure in developing regulatory documents on a national basis.

Some of the reports and the floor discussion stimulated by them took note of the advantages of nuclear electric power generating stations over power stations burning fossil fuels, from the vantage point of minimizing environmental pollutants. On the basis of experience acquired in the operation of the Novaya Voronezh nuclear power station, and other available data, the specialists came to the unanimous opinion that nuclear power stations based on VVÉR type reactors do not at the present time constitute sources of additional radiation exposure to the nearby populations. Topics relating to the structure of monitoring devices and systems, training of cadres of specialists in radiation safety, etc., were discussed.

The conference discussed, and agreed upon, a program of further collaboration between the various countries represented in the field of radiation safety over the period up to 1975. In the discussion of concrete forms of collaboration, the conference reached the conclusion that the most effective way to carry out the program would be to convene a coordination scientific-technical council of COMECON member-nations on radiation safety topics.

* * *

The first session of the Coordination Scientific-Technical Council on Radioactive Wastes and Deactivation met in Moscow on October 25-29, 1971, under the terms of the work plant of the COMECON Permanent Commission on the peaceful uses of atomic energy (PKIAÉ SÉV).

The specialists discussed results of scientific and technical research carried out by COMECON member-nations during 1971 within the framework of the program of collaboration on immobilization and deactivation of liquid, solid, and gaseous radioactive wastes and deactivation of contaminated surfaces. The session discussed the expanded agenda of a scientific-technical conference to be convened on this topic. The conference in question is scheduled for October 1972, in Poland. A work plan of the Coordination Scientific-Technical Council covering the 1972-1973 period was also approved in this session.

* * *

A conference of specialists from Hungary, Poland, Rumania, the USSR, and Czechoslovakia on the development of unified regulatory documents for the COMECON member-nations covering radiation sterilization of materials and wares for use in medicine was held in Warsaw, in November 1971.

Procedures for testing bandaging materials, synthetic polymeric materials and wares sterilized by radiation methods, general medical-technical requirements applicable to polymeric materials to be used in the fabrication of objects to come into contact with the blood stream or as blood substituents, were agreed upon at the conference, as well as general medical-technical specifications for packaging polymeric and combined bandaging materials. Suggestions on further procedures to be followed in the development of unified regulatory documents for the COMECON member-nations, and a proposed agenda for a symposium of COMECON member-nation specialists on radiation sterilization of medical wares, were also discussed and agreed upon. This symposium is scheduled for October 1972, in the USSR.

AN INTRODUCTION TO NONLINEAR OPTICS

By **George C. Baldwin**

Department of Nuclear Engineering and Science
Rensselaer Polytechnic Institute
Troy, New York

Beginning with a concise review of the electromagnetic theory of light and its interactions, this textbook concentrates on those recently discovered or relatively unknown optical phenomena which will play important roles in future laser applications. Dispersion, scattering, and birefringence are systematically investigated, along with coherence, optical susceptibility, and amplification of light waves. The book also describes the most spectacular optical phenomena, including conversion of one light into another, mixing of two colors to produce a third, and direct generation of electricity from light. Directed to the nonspecialist having a general knowledge of modern physics, differential equations, and vector notation, this book is also suitable as a graduate text in nonlinear optics.

CONTENTS: Introduction: The scope of optics • Historical background • Linearity in optics • Non-linearity in other fields • Non-linearity in optics • Scope of this book • **Background of Non-Linear Optics:** Electromagnetic theory of light • Electromagnetic theory of linear, isotropic media modes • Geometrical optics • Quantum theory of radiation process • **Properties of Optical Media:** Introduction • Dispersion • Rayleigh scattering • The Debye-Sears effect • Birefringence • Zeeman and Stark effects • Electrostriction and piezoelectricity • Electrically induced birefringence • Optical activity • Magneto-optical effects • Fluorescence and the Raman effect • Intensity-dependent optical phenomena • **Non-Linear Phenomena in Passive Media:** Introduction • Electromagnetic waves in a non-linear dielectric • The role of coherence in harmonic generation • The non-linear susceptibility tensor • Traveling-wave second harmonic generation • Index matching in birefringent materials • Boundary conditions • A numerical example • Index matching as momentum conservation • Harmonics higher than the second • Optical rectification • Optical mixing and parametric amplification • Self-focusing of optical beams • **Non-Linear Optical Phenomena in Active Media:** Similarities and contrasts • Raman processes • Brillouin processes Interactions of light with free electrons • Optical non-linearity in gases • **Appendix • Bibliography.**

155 pages PP 1969 $9.50
LCC No. 69-16517
SNB 306-30388-4

PLENUM PUBLISHING CORPORATION
Plenum Press • Consultants Bureau • IFI/Plenum Data Corporation
227 WEST 17th STREET, NEW YORK, N. Y. 10011

In United Kingdom: Plenum Publishing Co. Ltd., Donington House, 30 Norfolk Street, London, W.C. 2.

VISCOUS DRAG REDUCTION

Proceedings of the Symposium on Viscous Drag Reduction held 1968 in Dallas

Edited by **C. Sinclair Wells**
LTV Research Center, Dallas, Texas

Presents results of recent concentrated research on diverse problems in fluid dynamics relating to viscous drag reduction. From the basic mechanics of turbulent shear flows to vehicle performance gains with drag reduction, this work devotes particular attention to the reduction of turbulent skin friction in liquid flows by the use of polymer additives and to the analysis of new experimental data in many areas. Other topics discussed include boundary layer transition, prediction and control, drag reduction with polymer additives, applications of polymer drag reduction, and wall turbulence. Uniquely application-oriented, this volume will be valuable to fluid mechanics and acoustical physicists, materials scientists, and aerodynamic, aeronautical, aerospace, chemical, and mechanical engineers.

CONTENTS: Boundary Layer Transition, Prediction and Control, Mamoru Inouye • Invited lecture: On the many faces of transition, **M. V. Morkovin** • Boundary layer tripping with emphasis on hypersonic flows, **E. L. Morrisette, D. R. Stone and A. H. Whitehead, Jr.** • Ballistic range boundary-layer transition measurements on cones at hypersonic speeds, **N. W. Sheetz, Jr.** • Amplified laminar boundary layer oscillations and transition at the front attachment line of a 45° swept flat-nosed wing with and without boundary layer suction, **W. P. Pfenninger and J. W. Bacon** • **Drag Reduction with Polymer Additives, Ralph D. Cooper** • Invited lecture: The onset of dilute polymer solution phenomena, **P. S. Virk and E. W. Merrill** • Studies of viscous drag reduction with polymers including turbulence measurements and roughness effects, **J. G. Spangler** • Turbulent skin friction of dilute polymer solutions in rough pipes, **H. Brandt, A. T. McDonald and F. W. Boyle** • Drag-reduction measurements for three polymers at 4°C, **W. D. White** • Contrasts in the solution drag reduction characteristics of polymeric solutions and micellar systems, **J. G. Savins** • Exploratory drag reduction studies in non-polar soap systems, **I. Radin, J. L. Zakin, and G. K. Patterson** • Velocity profiles during drag reduction, **G. K. Patterson and G. L. Florez** • Drag reduction on a rotating disk using a polymer additive, **C. G. Gilbert and J. F. Ripkin** • Effect of wall shear stress on the drag reduction of viscoelastic fluids, **N. F. Whitsitt, L. J. Harrington and H. R. Crawford** • The use of pitot—static tubes and hot-film anemometers in dilute polymer solutions, **C. A. Friehe and W. H. Schwarz** • **Applications of polymer drag reduction, W. A. Meyer** • Invited lecture: Some observations on the flow characteristics of certain dilute macromolecular solutions, **A. White** • The effect of drag reduction and other improvements on the design and performance of submerged vehicles, **T. G. Lang** • Drag reduction in external flows of additive solutions, **Jin Wu** • The flow of a dilute polymer solution in a turbulent boundary layer on a flat plate, **D. A. White** • An analysis of uniform injection of a drag-reducing fluid into a turbulent boundary layer, **C. S. Wells** • **Wall Turbulence, D. A. Jewell** • Invited lecture: Viscous drag reduction examined in the light of a new model of wall turbulence, **T. J. Black** • The theory of skin friction reduction by a compliant coating in a turbulent boundary layer, **E. F. Blick** • A model for large eddy contributions in incompressible turbulent boundary layers, **J. L. Gaddis and J. P. Lamb** • An experimental study of the effects of dilute solutions of polymer additives on boundary layer characteristics, **J. M. Killen and J. Almo** • Normal-stress effects in drag-reducing fluids, **R. I. Tanner** • Relationship between flow pattern, constitutive equation and molecular structure, **F. W. Boggs.**

500 pages PP 1969 $22.50

PLENUM PUBLISHING CORPORATION
Plenum Press • Consultants Bureau • IFI/Plenum Data Corporation
227 WEST 17th STREET, NEW YORK, N. Y. 10011

In United Kingdom: Plenum Publishing Co. Ltd., Donington House, 30 Norfolk Street, London, W.C. 2.